NTNU

Norwegian University of
Science and Technology

Colloidal Crystals as Templates for Light Harvesting Structures in Solar Cells

Einar Haugan

Nanotechnology
Submission date: June 2011
Supervisor: Ingve Simonsen, IFY

Norwegian University of Science and Technology
Department of Physics

Colloidal crystals as templates for light harvesting structures in solar cells

Master thesis, TFY4905, spring 2011

Einar Haugan

Student number 684387

6th June 2011

Preface

This thesis was written in my fifth year at the Norwegian University of Science and Technology, and is submitted in partial fulfilment for the degree Master of Science in Nanotechnology.

I would like to thank the Institute for Energy Technology (IFE) at Kjeller for giving me the opportunity to do my master project with them on such an interesting topic. I am most grateful to my supervisors Erik Marstein at IFE and Ingve Simonsen at NTNU for their invaluable feedback and guidance throughout the work. I would like to thank Jo Gjessing, PhD candidate at the University of Oslo, for fruitful discussions and for sharing his experimental expertise regarding light trapping in photovoltaics. My gratitude also to Prof. Paul Bergstrom of Michigan Technological University for motivating the work on pre-patterning of wafers for electrochemical etching. I thank Jostein Thorstensen, PhD candidate at the University of Oslo, for the cooperation on laser processing using colloidal crystal microlenses. I am grateful to Prof. Bryce S. Richards at Heriot Watt University, Edinburgh, UK, for sharing his knowledge regarding upconversion and for interesting discussions regarding how the fields of upconversion and 3D photonic crystals can be united.

Finally a word of thanks to my classmates and office companions Susanne Helland and Carl H. Fosli for sharing this year with me at IFE and for all our discussions, both on and off topic.

Kjeller, June 6th 2011

Einar Haugan

Abstract

Monolayer colloidal crystals are formed using silica- and polystyrene beads and used as templates in nanosphere lithography for creating various hexagonal periodic structures intended for light harvesting in crystalline silicon solar cells. Specifically, arrays of silver islands for plasmonic scattering, dimples for use as seeds in electrochemical etching, and silicon cylinders diffraction gratings are fabricated and investigated. Where suitable, optical measurements are done to complement the structural characterisation.

Contents

Chapter 1

Introduction

1.1 Solar cells

Solar energy is a vast energy source. The Earth's surface receives on average $1.2 \cdot 10^{17}$ W of solar power, or 342 W/m^2, which means that in less than one hour our planet receives enough energy to meet the entire energy demand of the human population for a full year [1].

There exist many ways of harvesting energy from the sun. The powerful weather cycle on Earth is driven by solar energy, and we tap into this system using for instance hydroelectric power, windmills and biofuels. In a sense, therefore, these energy sources could justifiably also be referred to as "solar energy". However this term is most often reserved for more direct ways of collecting energy from the sun. Solar thermal energy conversion, for instance, is one such method, by which sunlight is used to heat up a fluid which in turn can be used directly for heating, or it may drive a turbine and generate electricity. A solar cell, on the other hand, can be defined as *a device which directly converts the energy in light into electrical energy through the photovoltaic effect*. The energy of the light is absorbed, generating free carriers (electrons and holes) which are fed into an external circuit, giving a potential difference.

The photovoltaic effect, in which light is used to generate electrical power, was first discovered by Alexandre-Edmund Becquerel in 1839 when he successfully generated electricity from a light-driven chemical process [2]. A few decades later the photovoltaic effect was observed in solid state materials, albeit at efficiencies no higher than 0.1%. Progress after the Second World War was significant, but photovoltaic devices were mostly reserved for applications in space. Terrestrial applications were considered infeasible due to prohibitively high costs. The oil crisis in the 1970's spurred the first major growth period of the global photovoltaic industry, facilitated by the recent microtechnical revolution and the introduction of silicon in the microelectrical industry. In recent years the industry has been booming, as a direct consequence of rising prices of fossile fuels and an increasing political focus on renewable energy.

While major strides have been made in recent years, much work remains to be done before photovoltaics become price competitive against fossile fuels globally. Solar cell research groups and manufacturers are currently exploring many different paths towards achieving this goal. While some are investigating thin film solar cells using exotic materials such as cadmium telluride (CdTe) and others are pursuing organic photovoltaics, the bulk of the market is still in silicon wafer based units. This is a mature industry which is starting to become price competitive with respect to other energy sources in many countries. Silicon solar cell modules on the market today typically have efficiencies around 15–18%, while the highest efficiency obtained in a lab environment without the use of light concentrating optics is 25% [3]. The theoretical efficiency limit, caused by the intrinsic properties of silicon, is 29% at AM 1.5 irradiation [1] [2].

The great challenge facing the silicon solar cell industry today is getting as close as possible to this efficiency level while keeping costs down. Wafers are produced in a very wasteful process where around half the silicon is lost in the sawing process. Contrary to what one might believe, material- and wafering costs only constitute approximately 15% of the price of a solar cell module, as seen in Figure 1.1 [4]. However, production of solar cell grade silicon is a highly energy intensive process, and the silicon used in solar cells is one of the key reasons why the energy payback time is about twice as long as for thin film equivalents [5]. This is a major reason why the industry is continuously moving towards thinner and thinner wafers. Thinner wafers are also beneficial because the collection efficiency of photogenerated free charges increases due to a shorter path way to the contacts.

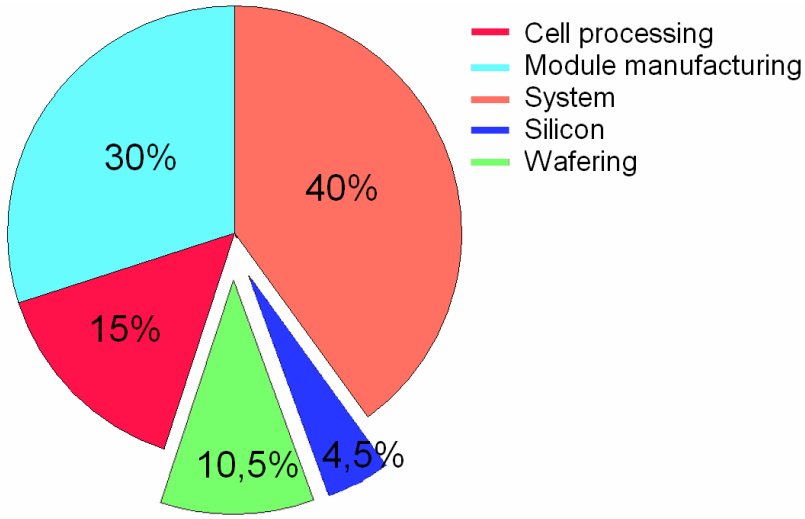

Figure 1.1: *Price composition of a standard silicon wafer based solar cell today. Data from Photon International [4].*

Since the absorption coefficient of long-wavelength light in silicon is low, making a

[1] AM 1.5 (air mass 1.5) is a standard reference irradiance spectrum, corresponding to a solar zenith angle of 48.19°

solar cell thinner has a negative effect on efficiency because some low-energy photons can pass through the entire structure without being absorbed. The lower the coefficient of absorption, the longer the absorption length (penetration depth) L of photons inside the material. In fact, the absorption coefficient in crystalline silicon drops off by more than three orders of magnitude as the wavelength increases from 500 to 1000 nm, as shown in Figure 1.2a.

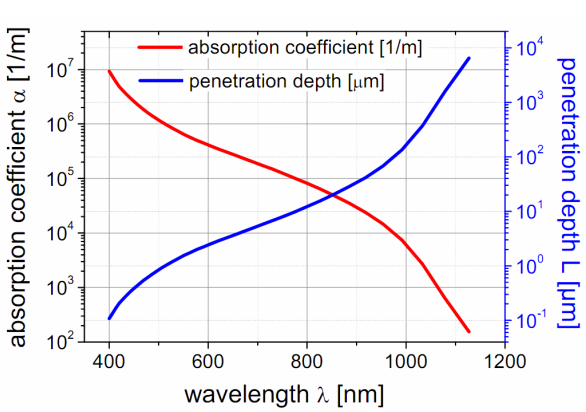

(a) *Absorption coefficient and penetration depth for crystalline silicon. Figure from Peters [6]*

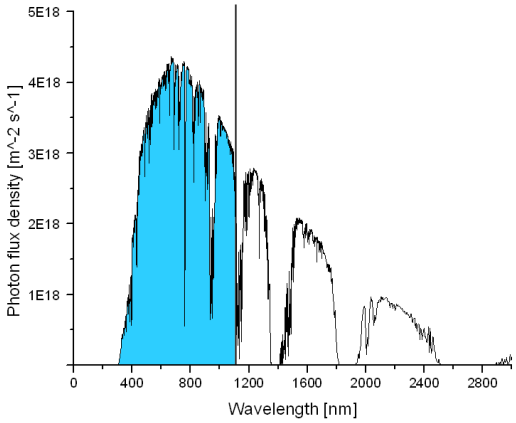

(b) *Photonic flux density reaching the surface of the Earth (AM 1.5 spectrum). The blue part represents light with energy in excess of the band gap of silicon, which can therefore be absorbed. Data from ASTM [7]*

Figure 1.2

Therefore as wafers become thinner more and more of the incoming photons will pass through the solar cell without generating free carriers, and the efficiency of the cell suffers as a result. And because module- and system costs scale roughly with module area one cannot afford to lose efficiency in this way. The concept of quantum efficiency is useful for understanding how this is so. Quantum efficiency is defined as the ratio of generated free charge carriers to the number of incident photons on the solar cell. The efficiency η scales with the quantum efficiency as follows: [2]

$$\eta \propto \int_0^\infty QE\left(E\right) \cdot b_s\left(E\right) dE \tag{1.1}$$

where $QE\left(E\right)$ is the quantum efficiency, E is the energy of the radiation and $b_s\left(E\right)$ is the incident spectrum of solar irradiation. The key point here is that the quantum efficiency of crystalline silicon remains very high (in excess of 80%) even for low energy photons close to the band gap. This means that one can simplify and say that *every incident photon is worth just as much* for the solar cell efficiency regardless of its energy as long as the energy is in excess of the band gap energy (wavelength less than 1118 nm). This is a common approximation in the ideal solar cell [2]. And as can be seen from Figure

1.2b, these low energy photons constitute a significant portion of the total irradiance. Therefore making sure that even the low energy photons get absorbed in the solar cell is of great importance. For this reason light trapping (harvesting) of low-energy photons is becoming an issue of increasing significance. If the path length of photons inside the wafer can be increased, then the silicon layer can be made proportionally thinner without sacrificing efficiency.

1.2 Light harvesting

The term light harvesting is often used to describe techniques used in solar cells which to enhance the absorption of light. The most common light harvesting method in industry today is to use a textured front surface which scatters light into the solar cell due to refraction at the surface. This typically yields an average path length enhancement factor no greater than 10 [2]. Theoretical calculations by Yablonovich [8] dictate that randomly texturing the front- and back sides of a wafer can increase the optical path length and hence the absorption efficiency up to $4n^2$ times compared to a perfectly flat front- and back side, where n is the refractive index of the material. For crystalline silicon this equates to a maximum theoretical path length enhancement of approximately 50 times. Thus, while light trapping is indeed used in solar cells today with some benefit, there is clearly a need for more efficient light harvesting schemes to be developed. This becomes ever more important as solar cells are made thinner and thinner, which causes more and more light to pass through the cell without being absorbed.

Besides making better and better scattering front- and back surfaces to increase the optical path length, it is also possible to take another approach to light harvesting. Looking at Figure 1.2b it is also obvious that much of the incident spectrum has too little energy to be absorbed in the solar cell. If several of these low-energy photons could somehow be combined into a photon of higher energy, this emitted photon could then be absorbed by the cell. In this way one could harvest a greater part of the solar spectrum, and in turn enhance efficiency. This type of method is known as *upconversion*.

1.3 Scope of the project

The purpose of this project is to synthesise various light harvesting structures for solar cell applications using colloidal crystals as templates. Colloidal crystals are close packed arrays of monodisperse beads, fabricated by self-assembly from a colloidal suspension. Figure 1.3 shows two representative electron microscopy images.

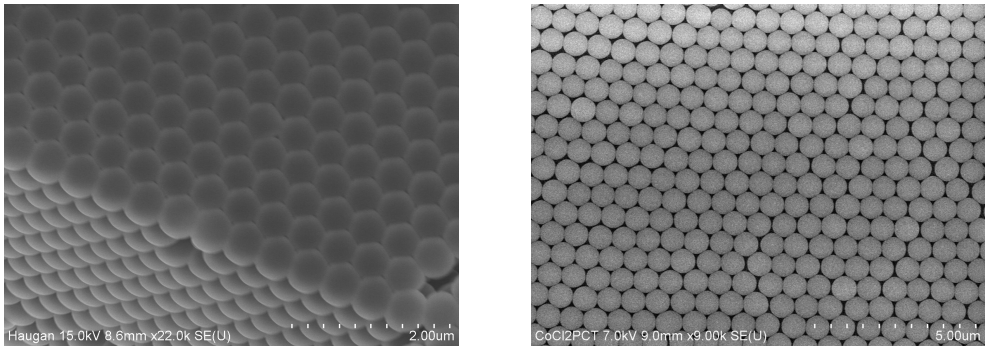

(a) *Multilayer crystal* **(b)** *Single layer crystal*

Figure 1.3: *Scanning electron microscopy (SEM) images of mono- and multilayer colloidal crystals synthesised in this work*

More specifically, the aim is to fabricate high-quality colloidal crystal monolayers on silicon substrates and use them as templates for the synthesis of the following structures:

1. 2D arrays of metal nanoparticles by nanosphere lithography. The plasmonic effects in such arrays will be studied. These structures are intended for use as front- or back scatterers in solar cells

2. Indentations or dimples in a wafer, intended as seeds for further processing by electrochemical- or chemical etching to produce various diffraction gratings for use as back reflectors in solar cells

3. 2D silicon cylinder diffraction gratings by nanosphere lithography processing. These structures are meant as back reflectors are solar cells

Chapter 2 goes through the fundamental physical theory which is needed to understand the synthesised structures. Chapter 3 is a literature review of techniques for the synthesis of colloidal crystals, including emphasis on the mechanics of the self-assembly process. Chapter 4 is a literature study of how to use colloidal crystals as templates for various advanced geometries which may be used for light harvesting.

Chapters 5 and 6 deal with the methods used, as well as the details of the experiments performed herein. Literature references and theoretical simulations performed in our

group will be used to determine the target design parameters of the synthesised structures, in order to tailor the optical properties of the structures for use in crystalline silicon solar cells. The results are finally presented and discussed in Chapter 7.

In addition to the above, significant effort was devoted to designing an initial proof-of-concept demonstration of an upconversion system taking advantage of photonic band gaps exhibited by photonic crystals. The demonstration consisted in using luminescent nanocrystals embedded in a 3D colloidal crystal, with the aim of investigating how the luminescence was quenched by the photonic band gap. Unfortunately, due to time constraints and practical difficulties, this work could not be completed within the time frame available. It is hoped that this work may be continued at a later date, and for this reason the background research and theoretical considerations are included as an appendix to this thesis.

Chapter 2

Theory

This chapter is split into three main bodies. First, a general introduction to the interaction of light with photonic crystals will be presented. Then, the relevant theory on 2D diffraction gratings and plasmonics is given.

2.1 Fundamentals of photonic crystals

Since photonic crystals are used extensively in this thesis for light-trapping purposes, this section provides a summary of the fundamental theory of such structures.

2.1.1 Light propagation and the master equation

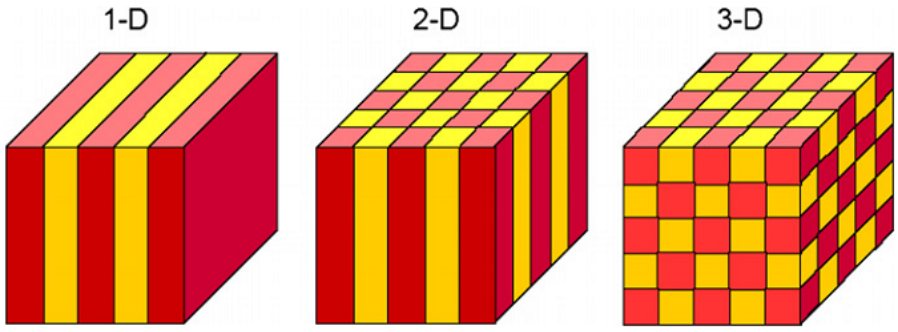

Figure 2.1: *Photonic crystals in one, two and three dimensions. Figure from Lipson and Lu [9].*

A photonic crystal consists of repeating regions of materials with alternatingly high- and low dielectric constants. The structure can be one-, two- or three dimensional, as illustrated in Figure 2.1. In the following discussion we will consider lossless, isotropic

and linear media. For simplicity the frequency dependence of the dielectric constant is ignored in the following discussion. These approximations are commonly used for photonic crystals [10]. Just as electrons of certain energies are not allowed to propagate in a semiconductor, some photons cannot exist within a photonic crystal. In order to understand why, it is necessary to consider the Maxwell equations which govern the propagation of light.

The electrical ($\mathbf{E}$) and magnetic ($\mathbf{H}$) components of an electromagnetic wave can be expressed as *harmonic modes* of frequency ω which separate the time- and space dependent components, such that

$$\mathbf{H} = \mathbf{H}(\mathbf{r})\, e^{-iwt}, \tag{2.1}$$

$$\mathbf{E} = \mathbf{E}(\mathbf{r})\, e^{-iwt}, \tag{2.2}$$

Inserting Equation 2.2 into the curl equations of Maxwell's relations, we arrive at

$$\nabla \times \mathbf{E}(\mathbf{r}) + \left(\frac{i\omega}{c}\right) \mathbf{H}(\mathbf{r}) = 0, \tag{2.3}$$

$$\nabla \times \mathbf{H}(\mathbf{r}) - \left(\frac{i\omega}{c}\right) \boldsymbol{\varepsilon}(\mathbf{r})\, \mathbf{E}(\mathbf{r}) = 0, \tag{2.4}$$

Combining these two equations we arrive at the so called *master equation* [10]:

$$\nabla \times \left(\frac{1}{\varepsilon(\mathbf{r})} \nabla \times \mathbf{H}(\mathbf{r})\right) = \left(\frac{\omega}{c}\right)^2 \mathbf{H}(\mathbf{r}) \tag{2.5}$$

where ω is the frequency of the mode and c is the speed of light in vacuum. $\boldsymbol{\varepsilon}(\mathbf{r})$ describes how the dielectric constant varies throughout the structure as determined by geometry. The master equation allows the allowed harmonic modes $\mathbf{H}(\mathbf{r})$ to be determined. Finally, using Equation 2.4 the E-field component of a mode can be obtained.

The master equation can also be expressed as an eigenvalue problem

$$\hat{\Theta}\mathbf{H}(\mathbf{r}) = \left(\frac{\omega}{c}\right)^2 \mathbf{H}(\mathbf{r}) \tag{2.6}$$

with a linear operator $\hat{\Theta}$ defined as

$$\hat{\Theta}\mathbf{H}(\mathbf{r}) = \nabla \times \left(\frac{1}{\varepsilon(\mathbf{r})} \nabla \times \mathbf{H}(\mathbf{r})\right) \tag{2.7}$$

This equation only has a solution if $\mathbf{H}(\mathbf{r})$ really is an allowed mode in this structure, in which case it has wavelength $\lambda = \frac{2\pi c}{\omega}$. So each mode corresponds to one unique frequency, but multiple modes may share the same frequency, in which case they are said to be *degenerate*. In fact, if two modes share the same frequency then the linear combination of the modes is also a solution, which follows from the fact that Equation 2.5 is linear. It may be shown that the operator $\hat{\Theta}$ is Hermitian so that all eigenvalues $\left(\frac{\omega}{c}\right)^2$ are nonnegative and ω is real [10].

Thus, starting from only the Maxwell equations and knowledge about the geometry and dielectric properties of a material, it is possible to determine which electromagnetic waves are allowed to exist within the structure.

2.1.2 Band structure and band gaps

A key issue in our discussion of photonic crystals is to determine the frequency dependence of allowed modes in a structure with discrete two- or three dimensional translational symmetry of period $\mathbf{R}$. The following discussion will focus on three dimensional structures, although the general theory applies to two dimensions as well.

Due to the periodicity, the entire real lattice can be expressed in terms of a *unit cell* with primitive lattice vectors $(\mathbf{a}_1, \mathbf{a}_2, \mathbf{a}_3)$, which is the smallest repeating unit. The corresponding reciprocal lattice vector $(\mathbf{b}_1, \mathbf{b}_2, \mathbf{b}_3)$ is defined such that $\mathbf{a}_i \cdot \mathbf{b}_j = 2\pi\delta_{ij}$ [11]. The unit cell in reciprocal space is known as the Brillouin zone. Now introduce a translational operator $\hat{T}_d$ which shifts the argument of a function by $\mathbf{R} = l\mathbf{a_1} + m\mathbf{a_2} + n\mathbf{a_3}$ where $\mathbf{a}_i$ are primitive lattice vectors in real space. Due to the periodicity of the photonic crystal structure, the allowed modes in such a system must be plane waves of the form

$$\mathbf{H}_\mathbf{k}(\mathbf{r}) = e^{i\mathbf{k}\cdot\mathbf{r}} \cdot \mathbf{u}_{n\mathbf{k}}(\mathbf{r}) \tag{2.8}$$

where $\mathbf{k} = k_1\mathbf{b_1} + k_2\mathbf{b_2} + k_3\mathbf{b_3}$ is the so called Bloch wave vector and $u_{n\mathbf{k}}(\mathbf{r})$ is a *Bloch function* which has the same periodicity as the lattice which modulates the possible solutions. In free space the Bloch function is unity and the modes are infinite plane waves. Conveniently, solutions to Equation 2.8 are the same for multiples $\mathbf{k}' = n\mathbf{k}$, which means that the entire solution of how light propagates in a crystal can be solved just by considering the behaviour in the first Brillouin zone.

The next step is to determine which frequencies are allowed to exist in a structure. As it turns out, the allowed modes in a photonic crystals exist in so called bands $\omega_n(\mathbf{k})$ where the band number n increases with increasing frequency [10]. Since it is sufficient to consider the band structure in the Brillouin zone, the band structure of a material can conveniently be displayed graphically. An example of such a band diagram is shown in Figure 2.2. Using this type of representation it is easy to see for which frequencies there exist allowed modes in the structure. Band diagrams are usually calculated using

the plane wave expansion method in which the eigenvalue formulation of the Maxwell equations is solved [12]. For frequency ranges where no allowed states exist, a *photonic band gap* is found. Light which falls within the band gap are not allowed to propagate inside the crystal.

A band gap can be either partial (incomplete) or complete. A partial band gap only exists for light travelling in certain directions. In Figure 2.2 the red and green bars represent partial band gaps. Band gaps may also exist for any propagation direction, and such a band gap is known as a *complete* or *full* photonic band gap [10]. The yellow bar in Figure 2.2 is a full photonic band gap. This type of band gap may only be achieved if the structure has long range dielectric periodicity in three dimensions and a high dielectric contrast (> 7.8) [13]. In general, the larger the dielectric contrast the wider the band gaps [14]. Dielectric contrast is defined as

$$\text{Dielectric contrast} = \frac{\varepsilon_1}{\varepsilon_2} = \frac{n_1^2}{n_2^2} \tag{2.9}$$

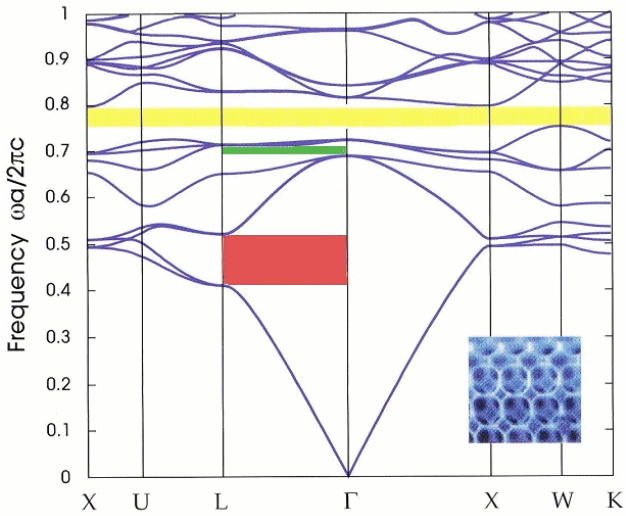

Figure 2.2: *Band structure of fully infiltrated silicon opal (silicon filling fraction 0.24). Photonic band gaps are coloured. Figure from Joannopolulos [10]. The x-axis shows critical points in an fcc lattice corresponding to various angles of incidence with respect to the crystal.*

In addition, the precise geometry and filling fraction of the structure are naturally also of paramount importance. Crucially, changing the physical dimensions of a photonic crystal by making the constituent building blocks smaller or larger causes the spectral response to be scaled by the same factor. In other words, if the spectral response $R^{r_1}(\lambda)$ of a system with characteristic dimension r_1 is known, then the spectral response of a system with characteristic dimension $r_2 = s \cdot r_1$ is simply $R^{r_2}(\lambda) = R^{r_1}(\lambda \cdot s)$. Thus, if the solution for one system is known the solution for any scaled structure can be found with ease. This makes it fairly straightforward to tailor the dimensions of the system such that the band gap(s) occur at the desired wavelength range for a given application.

In summary, photonic crystal structures may exhibit band gaps, such that light of certain frequencies cannot exist within the structure. The wavelength ranges at which the band gaps occur can be tuned by simply changing the dimensions of the structure, i.e. using smaller or larger periods.

2.2 Diffraction gratings

As said before, the most common type of light harvesting geometry implemented in solar cells today is a randomly textured front and/or back side, created by chemical etching. Even the best such random structures used at present yield photon path length enhancement factors no greater than 10 [2], while the theoretical limit for perfectly randomised light in crystalline silicon is around 50 [8]. Therefore, there is room for considerable improvement by designing better, more perfectly random scatterers. A surface which scatters light isotropically is known as a Lambertian scatterer.

Furthermore, calculations show that periodic gratings are capable of yielding path length enhancements exceeding the Lambertian limit [15]. For that reason periodic structures for light scattering in solar cells have become an issue of increasing importance. We shall here discuss their application as back reflectors in solar cells.

Some groups have explored the use of periodic metallic gratings for this purpose. While these structures might give an additional benefit due to plasmonic effects, as will be discussed later, problems related to absorption at the metal/semiconductor interface remain an issue of some concern. The possibility of using a periodic pattern of dielectric materials, i.e. a photonic crystal, rather than metallic structures is intriguing because the loss mechanisms related to material incompatibilities would be far less severe.

In this section the optical behaviour of diffraction gratings of various types will be explored.

2.2.1 Band gap effects

Due to their very intriguing optical behaviour, several attempts at integrating photonic crystals into photovoltaic applications have been made. The most explored option is the 1D photonic crystal. A Bragg stack, also known as a Bragg mirror, is the simplest configuration, consisting of alternating thin film layers of high and low refractive index. The Rugate filter is a variation of the Bragg stack consisting of layers of sinusoidally varying refractive indices. This type of 1D photonic crystal displays a reflectivity peak occurring at tuneable wavelength. However, a disadvantage is that reflectance is only efficient for near-normal incidence; no band gaps can exist for off-axis propagation [10]. Moreover, reflectance from a 1D photonic crystal is purely specular, meaning the scattering angle equals the angle of incidence. Therefore the path length enhancement

factor may not exceed 2, far shy of the theoretical limitation of 50 for Lambertian scattering in crystalline silicon.

In other words the only possible advantage of using a 1D photonic crystal instead of a metallic mirror is a higher reflectivity at normal incidence. This severely limits their usefulness for application in solar cells, except in solar cell modules using advanced tracking systems which always align the solar cell to be perpendicular to the incoming light.

A 2D photonic crystal is periodic in two directions and homogeneous in the third. Unlike the 1D photonic crystal, this type of structure is able to reflect some incoming light regardless of incidence angle in the plane of dielectric periodicity [10]. The mirror symmetry in the plane means that allowed modes can be divided into two different polarisations, known as transverse electric (TE) and transverse magnetic (TM) modes. These modes have their own separate band structures, which may be completely different. TE band gaps are favoured in a lattice where the regions of high dielectric constant are physically separated with no interconnections. TM band gaps, on the other hand, require that these regions be interconnected. A full photonic band gap for both TE and TM light is therefore only possible for highly sophisticated geometries with intertwining regions, while the type of gratings explored in this thesis are of simpler kinds.

Though complete bandgaps are very unlikely in 2D gratings, incomplete bandgaps may exist. For example, simulations by Li et al. [16] for hexagonal arrays of high-dielectric cylinders ($n = 3.6$) in air is shown in Figure 2.3 to display a wide incomplete band gap for certain angles of incidence.

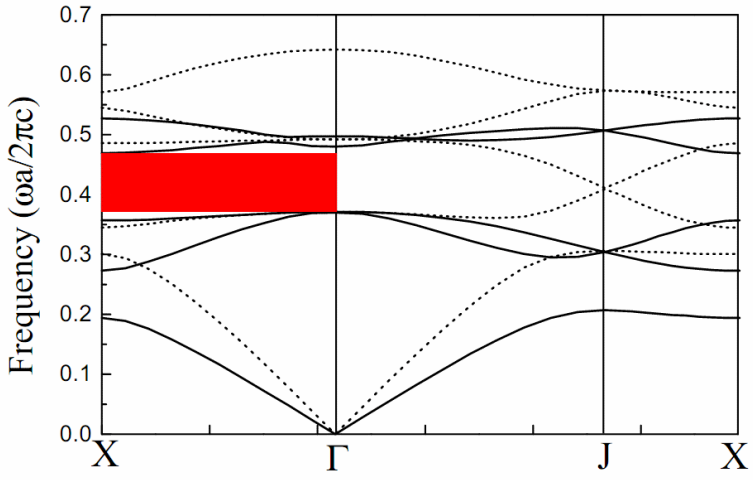

Figure 2.3: *Simulated band gap for hexagonal array of dielectric cylinders* ($n = 3.6$) *in air. Cylinders cover 40% of substrate area. Figure from Li et al. [16]*

It needs to be emphasised that 2D photonic crystals can only exhibit band gaps for light travelling in the plane of dielectric periodicity. No band gaps may exist for light

propagating in the direction along which the structure is homogeneous.

2.2.2 Diffraction effects

In the preceding subsection it was established that 2D periodic arrays, such as for instance grids of dielectric cylinders, can display incomplete bandgaps and that the reflectivity of such structures can therefore be rather high for certain angles of incidence. However this is only the case if light is incident in the plane of dielectric periodicity. Most experimental wafer patterning techniques lend themselves far more easily to the fabrication of structures which are periodic in the plane of the wafer. For this type of structure, no band gaps will occur. Yet the arrays may exhibit highly interesting diffraction effects for light incident on the wafer. These effects will now be described.

In Section 1.2 it was mentioned that using randomised interfaces at the front and/or rear of a solar cell may give a photon path length enhancement up to $4n^2$, where n is the refractive index of the material. This limit is derived assuming complete randomisation of light inside the medium, meaning that the probability of occupation of all photonic states in the material are the same. Unlike random surfaces, however, 2D periodic structures are able to scatter preferentially into just some modes or photonic states. It can be shown that various frequency dependent *diffracted orders* may exist, giving rise to intensity maxima in the reflectivity spectrum at various angles [6,10,17]. The zeroth order corresponds to specular reflectance where the angle of outgoing light equals the incidence angle, while higher orders occur at angles closer and closer to the surface of the structure. This is illustrated in Figure 2.4.

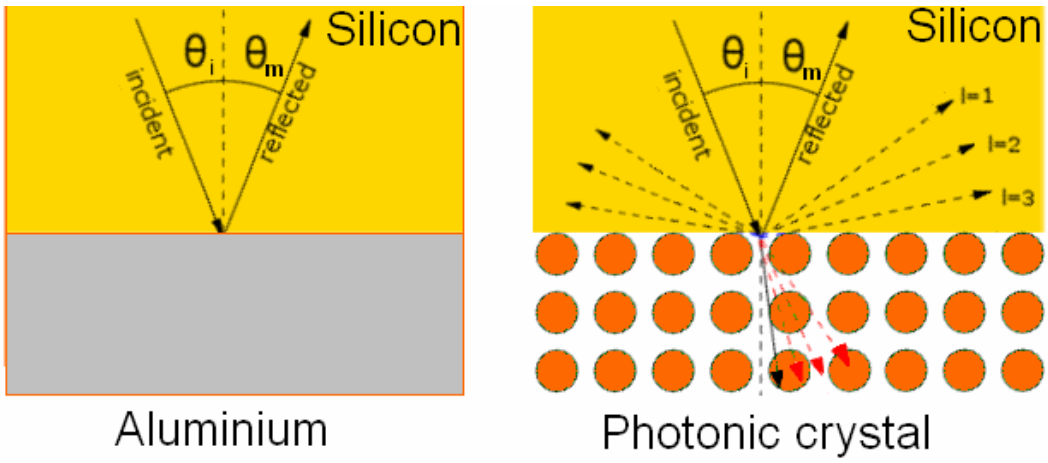

Figure 2.4: *Left: reflectance from a specular surface, such as aluminium. Right: illustration of the effect of higher diffracted orders l existent in a photonic crystal*

The angles at which these diffracted orders occur can be calculated quite readily. For the purpose of the following discussion consider a diffraction grating which is periodic in the (x, y) plane and homogeneous in the z-direction. The angle between the incident

light beam and the plane normal is the polar angle θ, and the azimuthal angle ϕ defines angles in the (x, y) plane. The diffracted beam will be associated with two diffraction orders m_x and m_y which together define the outgoing beam angles $\theta_{m_x m_y}$ and $\phi_{m_x m_y}$.

In the case of a two-dimensional grating at normal incidence, the diffraction equation is given as

$$\sin\left(\theta_{m_x m_y}\right)\cos\left(\phi_{m_x m_y}\right) = \frac{m_x \lambda}{n\Lambda_x} \tag{2.10}$$

$$\sin\left(\theta_{m_x m_y}\right)\sin\left(\phi_{m_x m_y}\right) = \frac{m_y \lambda}{n\Lambda_y} \tag{2.11}$$

where Λ_x and Λ_y represent the periods in the x- and y directions [18]. To simplify, consider instead the 1D case. Here the grating equation simplifies to

$$\sin\left(\theta_m\right) = \sin\left(\theta_i\right) + \frac{m\lambda}{n\Lambda} \tag{2.12}$$

where θ_i is the incident angle. In the case of normal incidence ($\theta_i = 0$), the angle of the diffracted beam is given by $\theta_m = \sin^{-1}\left(m\lambda/n\Lambda\right)$. In the small period limit, where $\Lambda < \lambda/n$, the equation has a real solution only for the zeroth order, $m = 0$. However for large periods, $\Lambda > \lambda/n$, higher diffraction orders are also allowed. The greater the period, the smaller the angular spread between diffraction orders, so a very large period is not beneficial because the lowest diffraction orders will scatter almost specularly and obtain very little path length enhancement. Therefore for practical designs the period should be chosen such that $\lambda/n < \Lambda < \lambda$ [19].

We have now established the angles at which the diffracted orders occur. However, calculating the relative power scattered into each of these orders is far more challenging. Usually this can only be done by computationally heavy modelling. This is because the power of light scattered into the different diffractive orders depends strongly on the precise geometry and materials of a particular photonic crystal and hence needs to be optimised for each such design independently. Needless to say one generally wishes to maximise the likelihood of scattering into higher diffracted orders, as this provides greater path length enhancements, as seen in Figure 2.4. Simulations are therefore a valuable tool when determining the design parameters.

Higher order diffracted light may even fall within the angle of total internal reflection, which ensures total absorption in the absence of loss mechanisms. Using periodically patterned gratings in solar cells thus makes it possible to exceed the $4n^2$ absorption efficiency limit over certain angle- and wavelength ranges [15, 20, 21]. In fact simulations by Zhou and Biswas [22] indicate that path length enhancements several times as high as the Lambertian limit may be attainable using "forests" of dielectric pillars in combination with a 1D Bragg stack, as illustrated in Figure 2.5a. They performed simulations for a cubic array of amorphous silicon cylinders embedded in indium tin

oxide (ITO), which is a common conductive oxide. The function of the Bragg stack is to act as a mirror for the light which is able to penetrate through the 2D cylinder array without getting diffracted. While their overall results are excellent, this synthesis route would be prohibitively expensive for large-scale manufacturing due to the high cost associated with building Bragg stacks. An alternative is to use a standard metallic mirror instead, as suggested by Gjessing et al. [19] and shown in Figure 2.5b. Silver has excellent reflective properties, but using aluminium is even more desirable for large-scale implementation due to the high cost and, eventually, scarcity of silver.

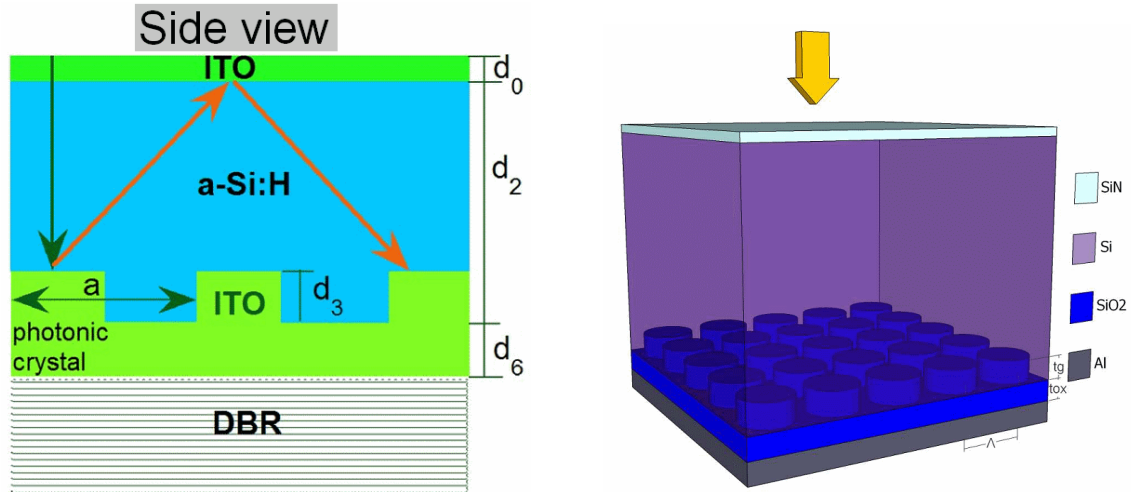

(a) *Photonic crystal back reflector design by Zhou and Biswas [22]*

(b) *Design by Gjessing, using an aluminium mirror on the back side [19]*

Figure 2.5: *Different 2D photonic crystal designs from literature*

From Equations 2.10–2.11 it is clear that the dimensions of the 2D photonic crystal need to be optimised depending on the wavelength range which one wishes to scatter most efficiently. As was mentioned in the introduction and shown in Figure 1.2a, the absorption of light in silicon is highly dependent on wavelength. Therefore only long-wavelength light will reach the back side of the solar cell, because the short-wavelength light will already have been absorbed in the first pass. This means that typically, one wishes to tailor the back reflector to give maximum reflectivity for light of wavelengths around 1000 nm. In fact, for 20 µm thick wafers, Gjessing calculated that diffraction gratings with a period of 0.95 µm gave the highest short-circuit current J_{sc} for most of the investigated structures, including arrays of hemispherical dimples, cones and inverted pyramids [21]. For this reason, 2D arrays with periods around 1000 nm were investigated in this work.

In summary, the allure of 2D photonic crystal diffraction gratings for use as back reflectors in solar cells is twofold. First, the reflected light may be preferentially scattered into higher diffraction orders, which can give substantial path length enhancement even exceeding the theoretical $4n^2$–limit proposed by Yablonovich for Lambertian (random)

scatterers. Second, optical losses associated with periodic dielectric structures are not as significant as for geometries involving metallic interfaces.

2.3 Plasmonic effects

Many research groups are currently investigating the use of plasmonics for light harvesting in solar cells. In this section, a brief review of the theory of plasmonics, as well as the various ways in which these effects might be useful in a solar cell, will be described. Emphasis will be on plasmonic effects associated with metallic nanoparticles rather than planar metallic surfaces.

2.3.1 Fundamental plasmon theory

In the Drude-Sommerfeld free electron gas model, conduction electrons in a metal are considered free to move around in a periodic potential of ionised atoms. When metals are illuminated by electromagnetic radiation the electromagnetic field causes a disturbance of the free electrons, oscillating around the fixed positive lattice ions. Such a collective oscillation of mobile electrons is known as a plasmon. This is shown schematically in Figure 2.6.

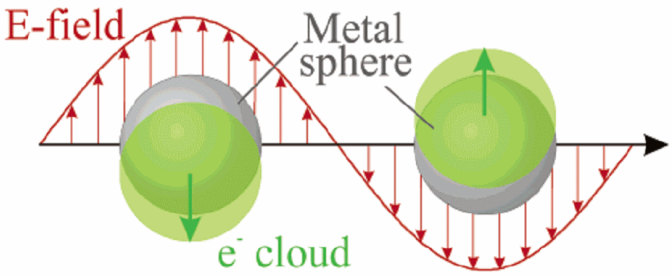

Figure 2.6: *Plasmon oscillation for a sphere, showing how the electron cloud is oscillating around the lattice ions. Figure from [23]*

Plasmons associated with bulk material (bulk plasmons), homogeneous surfaces (surface plasmon polaritons) and small features (localised surface plasmons) each have their unique properties. Here, emphasis will be on the latter, as this is the relevant kind for the structures studied later in this work. Localised surface plasmons (LSPs) are confined to the metal particles, and will now be described in more detail.

Light incident on a sub-wavelength diameter metal particle located on a surface can be described as an oscillating electric field $\vec{E}(t)$, which will induce a dipole moment on the particle given by [24]

$$\vec{p}(t) = \epsilon_p(\omega)\,\epsilon_m(\omega)\,\alpha\vec{E}(t) \tag{2.13}$$

where $\varepsilon_p(\omega)$ and $\varepsilon_m(\omega)$ are the dielectric constants of particles and embedding medium respectively, and α is the polarisability of the particle.

Light which is incident on such a metal particle may be scattered or absorbed. These are competing processes, which both can be described in terms of cross sections. The larger the cross section, the greater the probability of such an event. The cross sections C_{abs} for absorption and C_{scat} for scattering can be expressed as [25]:

$$C_{abs} = \frac{2\pi}{\lambda}\mathrm{Im}(\alpha) \tag{2.14}$$

$$C_{scat} = \frac{1}{6\pi}\left(\frac{2\pi}{\lambda}\right)^4 \alpha^2 \tag{2.15}$$

From these equations, it is seen that the cross sections of absorption- and scattering depend strongly on the polarisability of the metal particle, which, for a spherical particle, is given as

$$\alpha = 3V\left[\frac{\varepsilon_p(\omega)/\varepsilon_m(\omega) - 1}{\varepsilon_p(\omega)/\varepsilon_m(\omega) + 2}\right] \tag{2.16}$$

where V is the particle volume

The polarisability increases sharply towards resonance when the denominator of Equation 2.16 goes to zero; that is, when $\varepsilon_p(\omega) = -2\varepsilon_m(\omega)$. In this situation the cross sections, and hence probabilities, of both absorption and scattering are also at their maximum. The frequency ω at which this situation occurs is known as the *plasmon resonance frequency*.

Scattering versus absorption

It has now been shown that when the frequency of the incoming light equals the the plasmon resonance frequency of the metals particles, both absorption and scattering are at their maximum. The sum of the power removed from the incident beam due to absorption- and scattering processes is known as extinction [26]. Absorption is clearly a parasitic effect which is highly detrimental in solar cell applications, as the absorbed photons would be "lost" and contribute to heating the cell.

Whichever process has the higher cross section at a given frequency will dominate. From Equations 2.14 and 2.15 the scattering cross section increases with the polarisability in a cubic fashion, while absorption is merely linear. Hence absorption processes become less important relative to scattering for larger particles.

Factors affecting the resonance frequency

The plasmon resonance frequency of metallic particles depends not only on the size and dielectric environment of the particles, but also their shape. For near-spherical particles, Mie theory can be used to find the extinction coefficient $E(\lambda)$, which equals the sum of plasmonic scattering and absorption, theoretically by solving Maxwell's equations. The result is given by [27, 28]

$$E(\lambda) = \frac{24\pi N_A a^3 \varepsilon_m^{3/2}}{\lambda \ln(10)} \cdot \left[\frac{\varepsilon_i(\lambda)}{(\varepsilon_r(\lambda) + \chi \varepsilon_m(\lambda))^2 + \varepsilon_i(\lambda)^2} \right] \tag{2.17}$$

where a and N_A are the radius and areal density of nanoparticles respectively, $\varepsilon_m(\lambda)$ is the dielectric constant of the medium surrounding the nanoparticles while $\varepsilon_r(\lambda)$ and $\varepsilon_i(\lambda)$ are the real and imaginary parts of the metal dielectric function. χ is a number which accounts for the geometry of the particles, varying from 2 for perfect spheres to 17 for spheroids with an aspect ratio of 5:1. The higher the value of $E(\lambda)$, the greater the chance of scattering and absorption, meaning that the plasmon resonance occurs when the denominator goes to zero. Thus the position of the plasmon peak shows a strong dependence on the shape parameter χ of the particles.

Experimental literature results

Above, some theoretical considerations regarding plasmon resonance were presented, along with the factors affecting it. Many experimental results have also been presented in the literature, some of which will be summarised here.

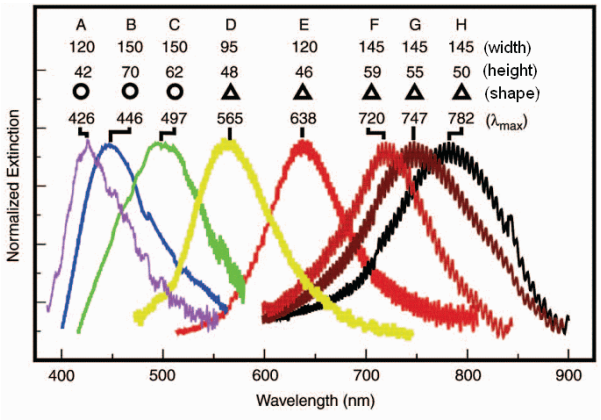

(a) *Normalised local surface plasmon resonance peaks as for different particle geometries. All measurements are in nm. Figure from Haes et al. [27]*

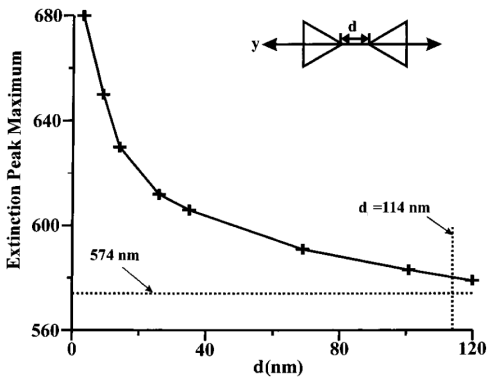

(b) *Resonance wavelength (extinction peak maximum) for triangular silver nanoparticles as a function of distance between adjacent particles. Simulations by Haynes et al. [29]*

Figure 2.7: *Resonance wavelength and its dependence on morphology and spacing between particles*

P. Van Duyne's group at Northwestern University have devoted significant attention to investigating how the geometry and nano-environment of the metal particles affect the plasmon resonance frequency [28, 29]. Some of their results are shown in Figure 2.7a. Larger and more pointy particles are generally found experimentally to give a red shift and broadening of the extinction peak. The distance between particles is also of great importance, as can be seen in Figure 2.7b for the case of triangles.

The authors also attempted coating the particles with a dielectric medium of different thicknesses. For triangular silver nanoparticles fabricated by nanosphere lithography, it was found that the resonance peak red-shifts by 4 nm for each nm SiO_x overlayer deposited by vapour deposition. They also found that the dielectric constant of the substrate plays a key role, as the resonance wavelength increases by 87 nm per unit of refractive index, eg. when the substrate refractive index changes from 1.5 to 2.5. These results are shown in Figure 2.8.

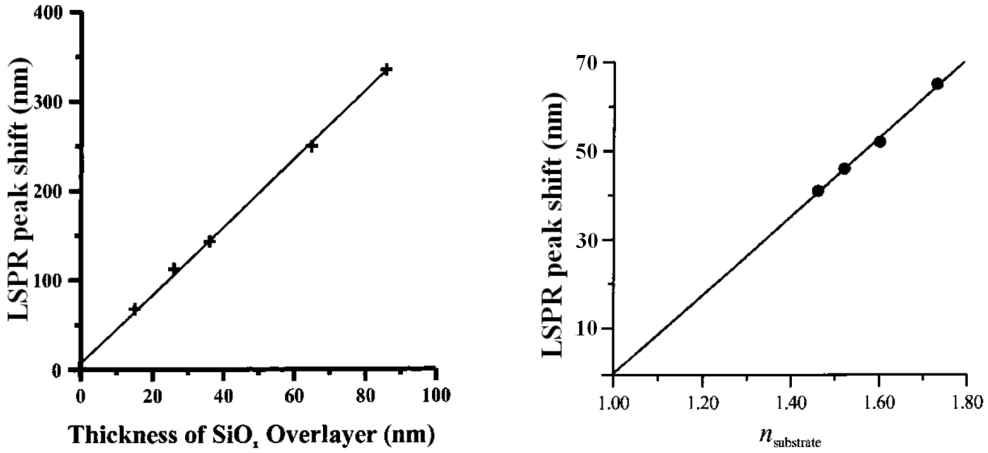

(a) *Resonance wavelength shift as a function of thickness of deposited SiO_x overlayer on top of metal particles*

(b) *Resonance wavelength shift as a function of the substrate refractive index $n_{substrate}$, expressed relative to a substrate of $n_{substrate} = 1$*

Figure 2.8: *Localised surface plasmon resonance (LSPR) wavelength as function of overlayer and substrate properties. Results from Haynes and van Duyne [29]*

	$\triangle a$ [nm]	$\triangle b$ [nm]	$\triangle d_{\mathrm{SiO}_x}$[nm]	$\triangle RI_{\mathrm{subst}}$
$\triangle \lambda_{max}$ [nm]	4	-7	4 *	87 **

Table 2.1: *Summary of how various parameters affect the resonance wavelength λ_{max} of triangular silver particles fabricated by nanosphere lithography. a is island in-plane diameter, b is island height, RI_{subst} is substrate refractive index and d_{SiO_x} is thickness of silicon oxide overlayer.*
** = explored for oxide thicknesses 0–100 nm*
*** = explored for substrate refractive indices in the range 1.5–1.8*

The effect of nanoparticle dimensions and environment on the resonance wavelength are summarised in Table 2.1. It is seen that low, large islands on a substrate of high refractive index and with a thick oxide overlayer gives the maximum red-shifted resonance peak. From the various results listed above, it is possible to derive an empirical equation:

$$\lambda_{max} = 1125 + (a - 240) \cdot 4 - (b - 22) \cdot 7 + 4 \cdot d_{\mathrm{SiO}_x} + 87 \cdot (RI_{subst} - 1.5) \qquad (2.18)$$

While useful, this equation must be used with some caution, taking into account the reservations listed in Table 2.1.

Measuring the resonance frequency

Extinction spectroscopy is used to determine the plasmon resonance frequency. In this method, light of various wavelengths is shone onto the sample, and the extinction as a function of wavelength recorded. The resonance frequency is detected either as a dip in transmission or a peak in reflectance.

In a practical device such as a solar cell, one would naturally seek to minimise absorption and maximise scattering into the substrate. Light is preferentially scattered into the medium of higher refractive index, in this case the wafer. This means that if extinction spectroscopy is performed by measuring the reflectance of a patterned substrate from the front side, a very high reflectance peak is not expected. This makes this kind of extinction spectroscopy difficult to use in practise. It is often preferred to measure transmittance instead and detect the resonance frequency as a dip in transmission. This technique is, however, most suitable for weakly absorbing substrates such as glass or very thin wafers. Since the plasmon resonance frequency is highly dependent on the refractive index of the substrate, direct inferences between the results obtained on glass and the expected resonance frequency on silicon substrates are difficult to make.

2.3.2 Plasmonics for device applications

It has been shown above how, when light is incident on a surface patterned with metallic islands, the light may be scattered or absorbed if its frequency equals the plasmon resonance frequency of the metallic particles. By tuning the geometry of the metallic islands, the plasmon resonance frequency may readily be altered.

There are several ways in which plasmonic effects can be interesting for device applications. Atwater [30] divides these methods into three categories, which are now presented.

Plasmonic scattering

Plasmonic scattering here refers to the effect where the metallic particles on a wafer act as subwavelength scattering elements which scatter the incident light into the wafer at higher angles to the normal, effectively increasing their path length inside the substrate. This method can be compared to other surface texturing techniques such as inverted pyramids described in Section 1.2, which serve the same purpose.

Metal particles embedded within a dielectric scatter uniformly in all directions, whereas if the particles are instead placed at an interface between two dielectric media they will scatter preferentially into the material of higher dielectric constant [31]. The dielectric constant of silicon is greater than that of many commonly used dielectrics for solar cell applications, such as SiN_x, SiO_2 etc. This means that if the metal particles are placed onto a silicon wafer surface and covered by another dielectric, which is a plausible configuration in a solar cell, light will be preferentially scattered into the silicon wafer. The angle of scattering will vary, and portions of the light will also be scattered at angles in excess of the total internal reflection angle, which gives a great increase of the optical path length inside the wafer. Unlike 2D gratings, which were discussed in Section 2.2, plasmonic light scattering would occur in random directions, such that the Lambertian path length enhancement limit applies.

At the plasmon resonance, the scattering cross section (Equation 2.15) can greatly exceed the particle diameter. For instance a 100 nm diameter silver particle in air has a scattering cross section ten times larger than its geometrical cross section. This important result indicates that a wafer covered by roughly 10% silver nanoparticles could scatter all incident light near the surface plasmon resonance frequency [25].

Plasmonic light concentration

Another way in which plasmonics may be interesting for photovoltaics relies on a slightly different concept. Plasmonic scattering at the interface between a metal and a dielectric may strongly enhance the intensity of light within one wavelength of the surface (near-field enhancement) [26, 32, 33]. In essence, this means that the incoming light is

concentrated at the metal-dielectric interface. The concentration of light at the metal-semiconductor interface is 1-2 orders of magnitude more efficient for particles than planar surfaces [27], and the efficiency of this effect is greatest for metal particles with diameters 5-20 nm [30]. Most of this field concentration occurs in the dielectric [25]. As the rate of free carrier generation (photogeneration) scales with the intensity of light in the material, this rate will be very high near the metal particles which are placed near one of the contacts.

An important point to consider here is free carrier diffusion lengths. Because photogeneration occurs near one of the contacts, the pathway of electrons and holes will be very different, as one of these types of carrier will have to diffuse across the entire cell thickness. Therefore this type of plasmonic effect is only interesting if the diffusion length of these carriers exceeds the cell thickness. In some materials, such as organic solar cells, diffusion length of one type of carrier (holes or electrons) is greater than the other, and these materials would therefore be very well suited for this type of cell. It is also necessary that the absorption rate in the semiconductor exceeds the plasmon lifetime (~ 10-50 fs), which is only the case for organic and direct-bandgap inorganic materials. This rules out crystalline silicon.

Light trapping by surface plasmon polaritons

The third plasmon light trapping mechanism for solar cell applications uses surface plasmon polaritons (SPPs). These are bound electromagnetic waves travelling along the interface between a dielectric and metal. Light which is incident on a surface patterned with metallic particles may thus give rise to travelling waves of light moving parallel to the surface. In simplified terms, the effect causes the bending of light to move in the lateral direction inside the cell, which may then be absorbed.

Unfortunately, plasmonic absorption in the metal is often significant, representing a loss mechanism. For a silicon/silver system, such losses will be greater than absorption in the semiconductor. In fact for silicon/silver interfaces, the effective photon path length in the 700-1150 nm spectral range is only in the order of 1 µm.

The main issue with this plasmon mechanism is the probability of formation of an SPP in the first place. Due to an inherent momentum mismatch between incoming light and an SPP, sophisticated light-in-coupling structures must be synthesised on the metal/dielectric interface to increase the probability of SPP formation. At the moment it seems that this light trapping scheme is most promising for ultrathin Si solar cells of thickness < 100 nm, for which all scattered light is predicted to be converted to SPPs. For thicker cells the usefulness of this principle is still under investigation [30].

Summary and evaluation

Three different ways in which plasmonic effects may be interesting for photovoltaics have just been described. Among these, the latter two are associated with serious

practical issues in a silicon/silver system. By far the most realistic and relevant of these methods is, therefore, plasmonic scattering, whereby the metallic particles randomly scatter light into the wafer. Such a structure may act as a random Lambertian scatterer for wavelengths of light close to the plasmon frequency.

Conveniently, this frequency may be tuned by altering the morphology of the particles. Larger particles and a more uneven (non-spherical) particle shape give a red shift and broadening of the extinction peak, which is of great interest for solar cell applications. Moreover, a rather modest ($\sim 10\%$) wafer surface coverage should be sufficient to effectively scatter nearly all incident light near the resonance frequency.

Chapter 3

Synthesis of colloidal crystal templates

In Chapter 2 various light harvesting concepts for use in solar cells were discussed. As we shall see, a recurring theme for all these is that that colloidal crystals may be used as templates or masks in in their synthesis. Self assembled colloidal crystals can be made quickly and at low cost, which is a great advantage to alternative top-down synthesis routes such as photolithography.

Monodisperse colloidal spheres can be routinely manufactured with diameters from a few nanometres to several microns. The Stöber process [34] provides a method for manufacturing silica (SiO_2) spheres, while polymer spheres are most commonly made through some variation of a heterogeneous radical polymerisation process [35].

In this chapter, methods for creating colloidal crystals are introduced.

3.1 Overview of methods

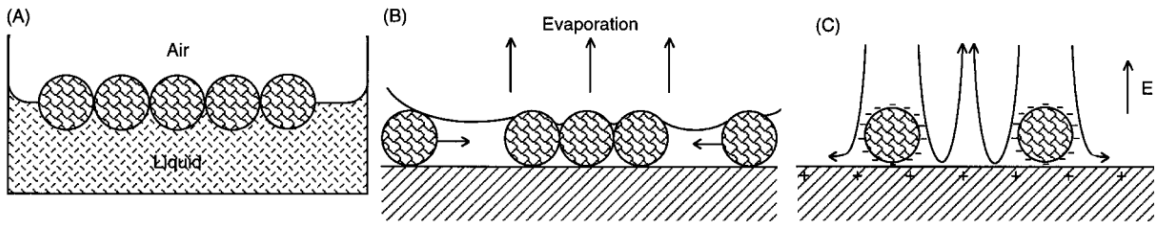

Figure 3.1: *The three categories of self assembly techniques for 2D colloidal crystals. (A): Assembly at air/liquid interface due to long-range attractive forces between particles. (B): Solvent evaporation causes attraction between spheres due to contraction of the meniscus. (C): Electrophoretic deposition, whereby an applied electric field causes sphere assembly. Figure modified from Xia et al. [36]. See text for further details*

Many different ways of creating colloidal crystals from dispersions have been developed over the years, including (but not limited to) sedimentation, spin coating, parallel plate confinement, Langmuir-Blodgett layer-by-layer synthesis, electrophoresis, hydrodynamic shear, evaporation induced self assembly (EISA) and substrate withdrawal [35]. These can be grouped into three categories based on the fundamental synthesis mechanism at play, as illustrated in Figure 3.1. In Type A synthesis, strong attractive interactions between spheres, such as dipole-dipole interactions, initiate the spontaneous formation of a close packed array of spheres at the interface. This array might then be transferred to a solid substrate. Various such Langmuir-Blodgett type of synthesis methods have been suggested.

Evaporation induced self assembly (Type B in Figure 3.1), relies on capillary forces between spheres in solution caused by a contraction of the meniscus as the solvent evaporates. Ko and Shin [37] recently suggested a mechanism for how this process occurs. They propose that as the solvent meniscus shrinks, some colloidal particles will be pinned to the substrate. Pinned particles cause a local increase of the solvent surface area, which leads to an increased rate of solvent evaporation. This causes an inflow of solvent, dragging along more particles which subsequently self assemble in close contact. Thus the few pinned particles act as nucleation centers for crystal growth, resulting in the formation of crystal domains. Crystal formation starts where the meniscus is thinnest [38].

Self assembly based on electrostatic forces (Type C in Figure 3.1) is a category which includes all the methods which rely on electrostatic attraction between spheres for self assembly. Here, the spheres are typically capped with a surfactant and the pH of solution is selected such that the surfactants are ionised. Then, applying an external electric field across a colloidal suspension confined between parallel plates may induce the self assembly of spheres in a two dimensional array on one of the electrodes.

In this work, evaporation induced self assembly (Type B) is explored further. This route is very intriguing in its simplicity relative to the alternatives, and numerous sources in literature have given very good results. The details of this synthesis category are described below, along with examples from literature.

3.2 Evaporation induced self assembly

Multiple methods relying on the principle of EISA for self assembly of polystyrene colloidal spheres into monolayers have been developed. Among these techniques vertical deposition (dip coating) [39, 40], spin-coating [41–43] and horizontal evaporation [17, 38, 44–47] have been extensively explored.

For each of these approaches there is a number of considerations which have to be made. First, the composition of the sphere solution must be optimised. This includes

selecting the sphere concentration, dispersion medium, and possible surfactants to aid the process.

The wetting properties of the solvent on the substrate need to be controlled and optimised. This is important to enhance the capillary attraction between spheres during evaporation, which depends greatly on contact angle. Most often the substrate is made hydrophilic by a chemical or physical treatment to alter the surface chemistry.

Third, the atmosphere in the deposition chamber must be selected. Both temperature and humidity play an important role. Several authors [37, 38] agree that film growth starts with a few pinned particles acting as nucleation centers for growth due to a local increase of solvent evaporation rate. Each such nucleation center eventually forms a domain. The domain size depends on the evaporation temperature. A high temperature means that the colloidal particles have a high kinetic energy and thus rapid random thermal motion, which enables them to probe a larger portion of the substrate. This allows particles to migrate to the most energetically favourable positions, which are found at the already growing crystal domains, rather than forming new small domains [48]. In multilayer formation a higher temperature appears to give better crystal quality, while for monolayers the opposite is true; film quality improves and domains become larger at lower temperatures [38, 45, 47, 49].

A concern with all EISA-based deposition techniques is the formation of agglomerates of spheres in solution. Ideally, the colloidal spheres should repel each other and avoid clustering. However, depending on the surface treatment of the beads, they will tend to agglomerate to a certain extent, forming large clusters which severely deteriorate the quality of the deposited film. Kumar [50] investigated this problem for non-functionalised 458 nm diameter silica beads as part of her M.Sc-thesis. She discovered that 5-6 hours of sonication at temperatures between 24-27°C was necessary to completely remove all aggregates.

The concerns listed above apply to all techniques relying on EISA. Now, some specific techniques of this kind will be described in more detail.

3.2.1 Horizontal evaporation

The method of horizontal evaporation has been explored by several authors. Most often, this method involves placing a droplet of sphere solution on a substrate and letting the solvent evaporate [38, 45, 47]. If the sphere concentration from the manufacturer is known, as well as the wetting properties of the film, the optimal dilution factor needed for monolayer formation can be calculated with ease. A solid fraction around 1% is used with success by several authors [38, 47]. Higher concentrations will give multilayer formation over some areas while a lower concentration causes voids between monolayer areas. Some examples of monolayers fabricated in this way are shown in Figure 3.2.

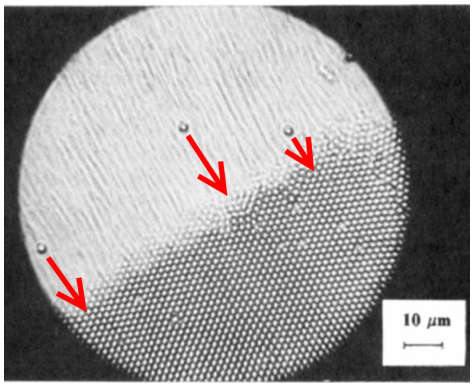

(a) *Formation of monolayer. Influx of spheres from solution towards monolayer is marked with red arrows. Sphere diameter 1700 nm. Figure edited from Denkov et al. [38]*

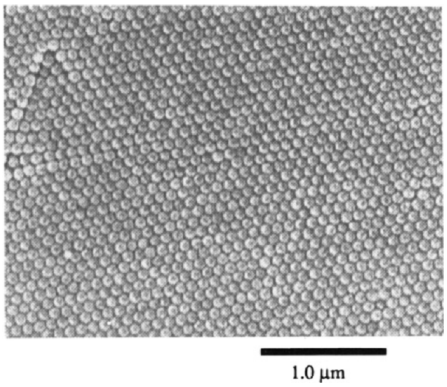

(b) *Example of monolayer obtained. Figure from Micheletto et al. [45]. Sphere diameter 100 nm.*

Figure 3.2: *Formation of monolayers by horizontal evaporation*

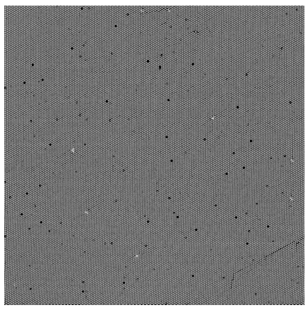

(a) *Example of monolayer film obtained by Kosiorek [46], area 100x100 μm.*

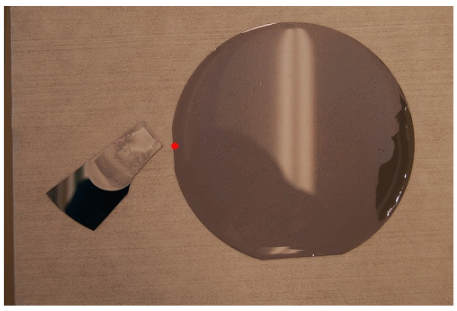

(b) *Adaptation by Granlund [17]. The wafer (right) is covered by a pure water film. The small wafer piece (left) is covered by concentrated colloidal suspension from the manufacturer.*

Figure 3.3: *Monolayer fabrication by horizontal evaporation, onto liquid meniscus*

A slightly different approach was introduced by Kosiorek et al. [46]. Rather than preparing a uniform sphere solution, a wafer was first wet with pure water and a droplet of concentrated sphere solution was then carefully applied on top of this. This caused the formation of a monolayer on the water surface. When the solvent subsequently evaporated, the monolayer was left behind on the substrate. This process yielded

monolayers covering up to 25 cm^2 for polystyrene spheres of diameter 540 and 1710 nm. An image of the resulting monolayer is shown in Figure 3.3a.

Yet another adaptation of this method was pioneered by Granlund [17]. In this method, a wafer was first covered by a water film. A few drops of concentrated colloidal suspension were placed on another separate small wafer piece, as seen in Figure 3.3b. By touching these two substrates together, spheres were observed to diffuse onto the water meniscus on the large wafer until monolayer formation was achieved. As the water was subsequently evaporated in a controlled atmosphere at room temperature, neatly arranged domains of average size around 300 μm^2 were formed. However, this approach was only successful for Ugelstad spheres of diameter 3270 nm, and failed when attempted with polystyrene spheres with diameter 490 nm.

3.2.2 Spin coating

Spin coating has been used to successfully synthesise mono- and multilayer colloidal crystals. By changing the spin time and speed, Jiang et al. [42, 43] were able to tune the film thickness from 1 to well over 100 layers using spheres of diameters from 130 to 1320 nm. Colloidal crystals with thickness variations of less than 4% were routinely manufactured on four-inch diameter wafers in a matter of minutes. The spheres were suspended in a viscous monomer solution prior to spinning, and the monomers were photopolymerised after deposition to yield a rigid final structure. Examples of synthesised films are shown in Figure 3.4. Monolayers could also be achieved by a slight modification of the spin speed regime and wafer priming [43]. These monolayers covered the entire 4-inch wafer and consisted of domains of size ~ 10000 μm^2. These films displayed a non-closepacked hexagonal pattern. Examples are shown in Figure 3.5.

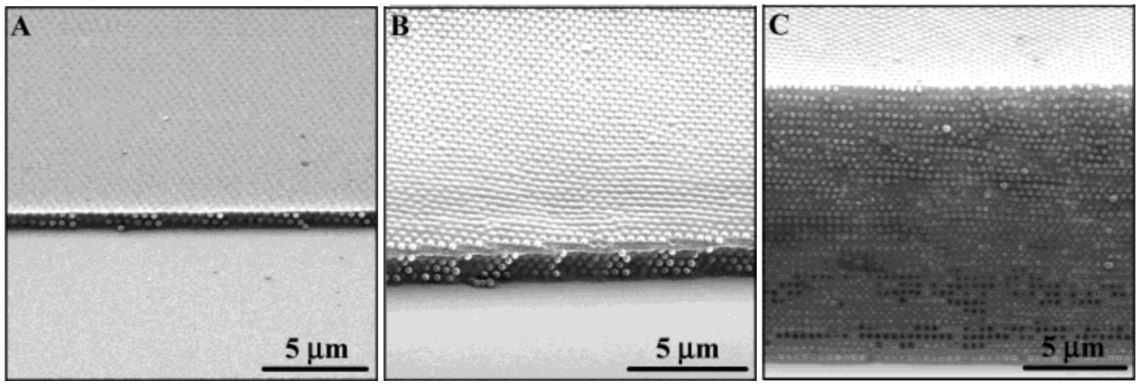

Figure 3.4: *Spin coated multilayer films produced by spin coating, from Jiang et al. [42]. Sphere diameter 325 nm.*

The difficulty in this approach lies in the use of highly toxic and expensive chemicals, as well as the need for photopolymerisation following bead deposition. Other authors have obtained similar results without the use of viscous solvents, including the pioneering

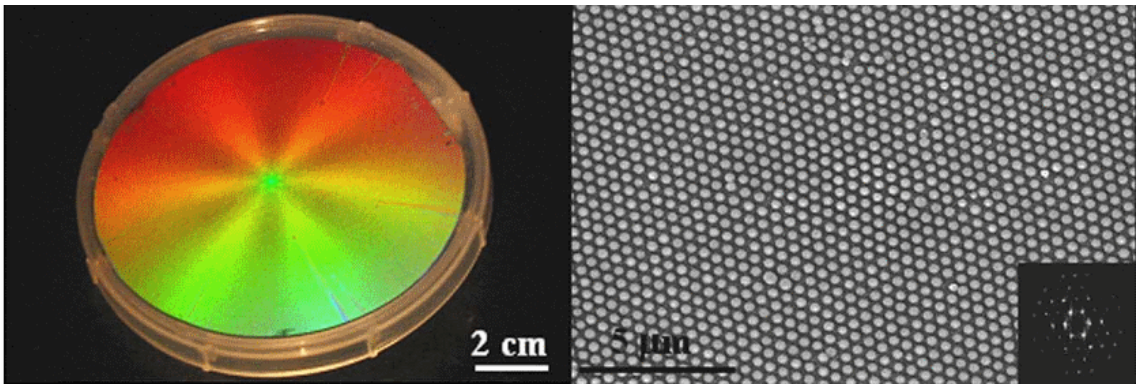

Figure 3.5: *Spin coated non close-packed monolayer film produced by spin coating, from Jiang et al. [43]. Sphere diameter 315 nm.*

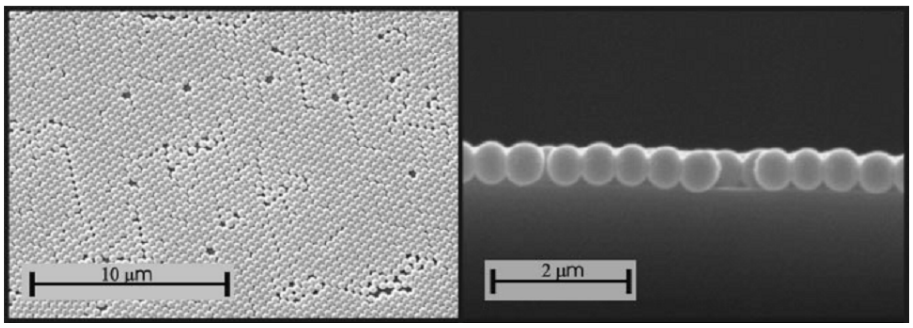

Figure 3.6: *Monolayers obtained by spin coating of silica colloids in a mixture of ethylene glycol, water and ethanol. Results from Mihi et al. [51]. Sphere diameter 440 nm.*

work in the field by Hulteen and Van Duyne [52]. While these authors used dilute aqueous suspensions with added surfactants, Klein et al. [53] used ethanol as the only additive to the aqueous suspension of polystyrene beads. They reported that defects covered less than 10% of the wafer surface, and domains were several 1000 µm^2.

Mihi et al. [51] obtained layers of controllable thickness using polystyrene and silica beads dispersed in a mixture of ethanol, ethylene glycol and water. Ethylene glycol is a viscous solvent of high boiling point which serves to improve crystal quality by slowing down the rate of shear and evaporation. By using volume concentrations of ethylene glycol larger than 30% and particle volume fractions less than 30%, monolayers with crystalline domains in the order of 10000 µm^{2}were obtained. The number of layers was determined by varying the spinning speed. Representative scanning electron microscopy (SEM) images are shown in Figure 3.6.

3.2.3 Vertical deposition

If a substrate is placed nearly vertically into a colloidal suspension, the spheres are observed to spontaneously self-assemble into a mono- or multilayered colloidal crystal

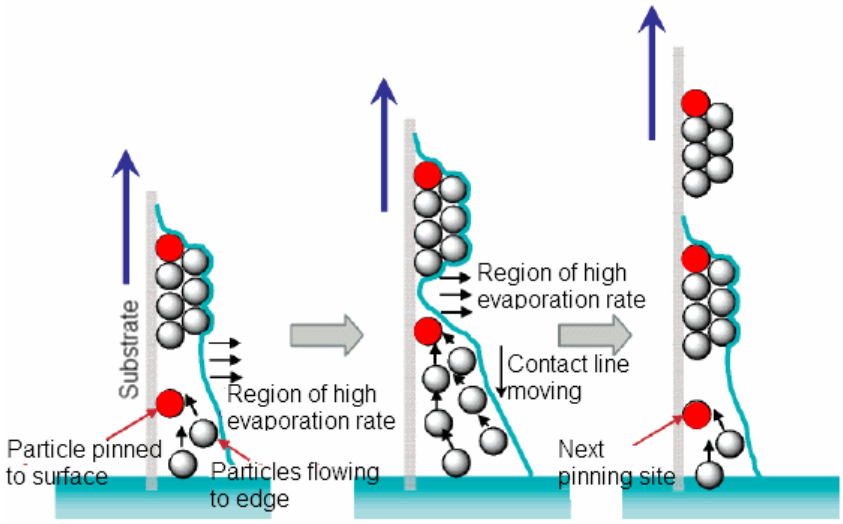

Figure 3.7: *Mechanism of domain formation, proposed by Ko and Shin [37]. Red spheres represent pinned spheres which act as nucleation sites for new domains. Figure modified from [37].*

on the surface in a close packed conformation, provided an adequately low wetting angle with the substrate [54]. This phenomenon was first described by Colvin et. al [55]. The spheres migrate towards the meniscus driven by convective forces where they self assemble due to capillary forces. To minimise free energy the solvent "neck" between particles at the meniscus will contract to reduce its surface area, thus bringing the particles closer together in a close packed array [35, 54]. Ko and Shin [37] recently suggested a mechanism for how this process occurs. They propose that as the solvent meniscus is dragged along the substrate, some colloidal particles will be pinned to the substrate. Pinned particles cause a local increase of the solvent surface area, which leads to an increased rate of solvent evaporation around each pinned particle. This causes an inflow of solvent, dragging along more particles which subsequently self assemble around the pinned particle. Thus the few pinned particles act as nucleation centers for crystal growth. Then as the water meniscus moves further down the substrate the process repeats itself, resulting in the formation of separated domains, as shown in Figure 3.7. Domain formation as defects will be described further in Section 3.3. Layer formation is driven by van der Waals and electrostatic forces between particles. For multilayer crystals, the most energetically favourable conformation is fcc stacking, but the free energy difference between fcc and hexagonal close packing (hcp) is only approximately $10^{-3}k_b$ [56]. However the most typical conformation observed in EISA on vertical substrates is an fcc packing with the (111) planes parallel to the substrate surface [57, 58].

The method of vertical deposition was primarily explored by Nagayama and coworkers [39]. They suspended the substrate vertically into a solution of spheres. As the substrate was withdrawn from solution or the solvent evaporated, mono- or multilaye-

red structures were spontaneously formed. The rate of growth, v_c, was found to be given by the following equation:

$$v_c = \frac{\beta L j_e \varphi}{0.605 d v \, (1 - \varphi)} \tag{3.1}$$

where β is the ratio between the velocity of a particle in solution and the fluid velocity, L is the meniscus height, j_e is the solvent evaporation rate, d is the colloidal particle diameter, φ is the particle volume fraction and v is the relative movement of the substrate out of the solution, either by pulling the substrate out of the beaker or by evaporating the solvent.

An inherent problem with this method, as explored in the preceding project work, is that the number of sphere layers deposited tends to increase towards the bottom of the substrate. As the solvent evaporates the concentration of spheres in the beaker will rise. According to Equation 3.1 the growth rate depends on the volume fraction of solids φ as $v_c \propto \frac{\varphi}{1-\varphi}$, meaning that a larger volume fraction leads to a higher growth rate of the film, which in turn gives a thicker layer. Despite this, several groups have managed to achieve good thickness control by this method, including the fabrication of monolayers over large areas [39, 48, 55].

3.3 Crystal quality

Self assembled monolayers made by evaporation induced selfl assembly can either be amorphous or crystalline, depending on the synthesis parameters. Crystalline films are always poly-crystalline, with domain sizes typically in the 100-10000 µm^2 range. The domains in polycrystalline monolayer films prepared by spin coating tend to be of either square or hexagonal ordering, corresponding to the (100) or (111) planes of an fcc crystal respectively. As was mentioned in Section 3.2, the free energy difference between the different crystalline packing conformations is very low compared to the thermal energy at room temperature. This may cause the packing order of the crystal to change during growth, giving regions of square non-close packed order or other non-desirable conformations [59]. It is therefore very important to achieve good control of the deposition conditions in order to produce crystals of good quality.

When shining white light onto such a monolayer structure, one typically observes four- or six armed colourful reflection patterns on the substrate. Examples are shown in Figure 3.8a. Whether four-arm or six-arm patterns dominate have been shown to be dependent on both spinning speed and the solvent [50]. Some authors, noteably Jiang and McFarland [42], interpret the presence of such patterns as evidence of long-range "globally even" distribution of spheres. Kumar, on the other hand, showed by laser diffraction and SEM investigations that the most likely interpretation is that

the orientation of domains remains relatively unchanged in the radial direction while tangentially it is more random, as sketched in Figure 3.8b. In other words she proposed the coexistence of long-range orientational order (between domains) with short-range positional order (within domains).

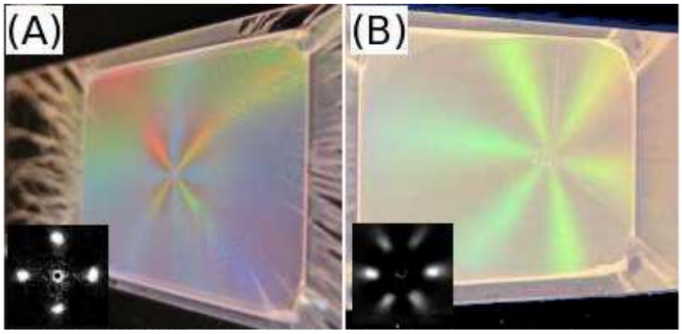

(a) *White light reflection patterns from monolayer colloidal films of 500 nm diameter silica beads. Four-arm (A) and six-arm (B) reflection patterns are seen. Insets show laser diffraction patterns confirming the symmetries. Results from Kumar [50].*

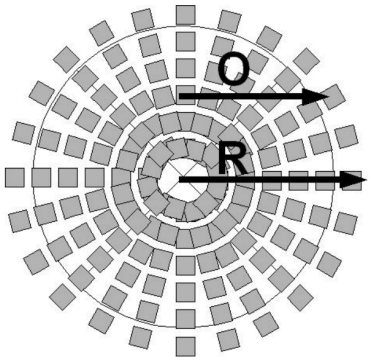

(b) *Proposed orientation of polycrystalline monolayer structures. Orientation remains nearly the same radially (along R) but changes in the tangential direction (along O). Model from Kumar [50]*

Figure 3.8: *Long range order in colloidal crystal monolayers*

Many parameters can affect film quality. Generally a high growth rate can cause high internal stresses which in turn cause more cracking and smaller domains, while a too low growth rate causes weak lateral forces during deposition which gives thin films of poor quality [48]. Even if the growth rate is kept constant film quality can still vary significantly for example with humidity. Recall that film growth in EISA is believed to start with a few pinned particles acting as nucleation centers for growth due to a local increase of solvent evaporation rate. Each such nucleation center eventually forms a domain, as was illustrated in Figure 3.7. The domain size depends on the evaporation temperature. A high temperature means that the colloidal particles have a high kinetic energy and thus rapid random thermal motion, which enables them to probe a larger portion of the substrate. Thus particles can migrate to the most energetically favourable positions, which are found at the already growing crystal domains, rather than forming new small domains [48]. For this reason high deposition temperatures are generally favourable. However in some adaptations of EISA, such as spin coating, a high temperature may cause a too rapid solvent evaporation rate, which in turn forces the beads to in energetically non-optimal positions. Thus for spin coating, depositing at a high temperature using a solvent with a high boiling point is advantageous. In this way the kinetic energy of the particles would be high enough to probe large areas, while the evaporation rate would be low enough to provide the colloids enough time to diffuse to the nucleation sites.

Chapter 4

Nanosphere lithography

In Chapter 2 it was shown that diffraction gratings and plasmonics hold great promise for light harvesting applications in solar cells, while in the preceding chapter it was shown how colloidal crystals can be made from suspensions. Now, these two concepts will be unified, and it will be shown how such colloidal crystals may be used as templates for the production of the desired light harvesting structures.

Nanosphere lithography (NSL) is a broad term used to describe fabrication techniques where two dimensional arrays of colloidal spheres are used as templates for further processing. These processing techniques can be roughly split in two categories. The first category is where a material is deposited on top of the entire crystal before the spheres are removed, leaving behind material only in the gaps between spheres. The second category uses the spheres as an etch mask for selective etching of the substrate, either by chemical or physical etching. In this work, the definition of nanosphere lithography is extended to include the use of colloidal crystal monolayers as microlenses for the patterning of a substrate by laser ablation.

After processing the spheres are typically removed by sonication in a solvent [60].

As was seen in the previous chapter, most 2D template synthesis methods cause the colloidal spheres to arrange themselves in a hexagonal close packing. For some NSL procedures this mask can be used directly, but often it is necessary to alter the size of the spheres before using as a template. The voids between spheres can be made larger by plasma etching (O_2 etching) or smaller by annealing, as shown in Figure 4.1.

In this chapter the use of NSL for the fabrication of plasmonic nanostructures and 2D gratings will be discussed.

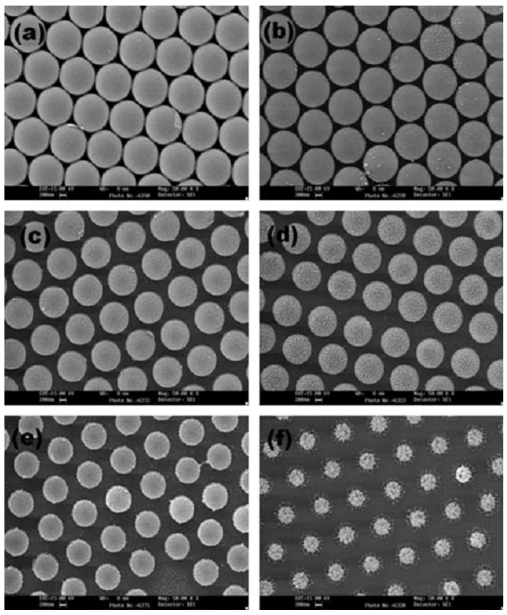

(a) *O_2 etching of polystyrene colloidal crystal template to reduce the sphere diameter. Figure from Valsesia et al. [61]*

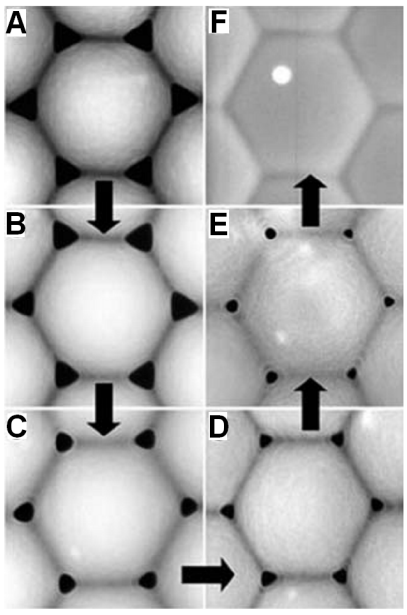

(b) *Annealing of colloidal crystal template. Figure from Li et al. [62]*

Figure 4.1: *Post processing of close packed monolayer colloidal crystals*

4.1 Metal islands for plasmonics

In Section 2.3 it was established that very interesting plasmonic light scattering effects may arise if a dielectric substrate is covered by nanosized metal particles. Nanosphere lithography has been extensively explored for the fabrication of such nanoparticles. After the 2D colloidal crystal template has been manufactured, a metal is deposited on top by methods such as thermal evaporation, pulsed laser depositon or electron beam deposition. By tailoring the process parameters it is possible to achieve uniform coverage over the entire substrate such that material is also deposited in the holes between spheres. The template may then be removed either by chemical dissolution or in an ultrasonic bath (or both), leaving an hexagonal pattern of metallic nanoparticles on the substrate.

As was established in the theory section, the size and shape of the nanoparticles is very important for the surface plasmon resonance frequency, and hence also dictate the interaction with light. Nanosphere lithography provides ample opportunity to tune these parameters. The period of the array scales with the diameter of spheres used in the template, while island height is determined primarily by the amount of metal deposited. The as-deposited metal islands will be roughly triangular in shape, but this may be altered by a thermal or chemical treatment. Heat treatment (annealing) will cause the particles to become more rounded, in order to optimise the contact area

between silicon and silver, as determined by the surface wetting properties.

In Section 2.3.2 it was mentioned that theoretically, 100% of the incoming photons near the plasmon resonance frequency may be scattered if silver particles deposited on the front side of a silicon wafer cover roughly 10% of the wafer [25]. In NSL using close-packed spheres, the as-deposited area fraction covered by the triangular silver islands will theoretically be 9.3%. Post-processing steps such as annealing can be used to alter the morphology of the particles.

A concern with plasmonic scattering from metal islands is that the colloidal crystal monolayer template consists of small crystalline domains with defects. Since the plasmonic scattering is so dependent on the exact shape and size of the silver islands this might be an issue, degrading the performance. However, Malinsky et al [60] found experimentally that macroextinction spectra using probe areas of 4 mm^2 gave the same results as microextinction spectra with probe areas of 12 μm^2, which is well within a grain. This indicates that metal island defect sites formed due to mask imperfections should not affect the plasmon resonance spectrum to any appreciable degree.

4.2 Diffraction gratings

As explained in Section 2.2, two dimensional photonic crystals / diffraction gratings may exhibit highly interesting optical properties which would make them suitable as back reflectors in solar cells. Such structures may bee fabricated on crystalline silicon wafers using both dry- and wet etching, and these methods will be described in this section.

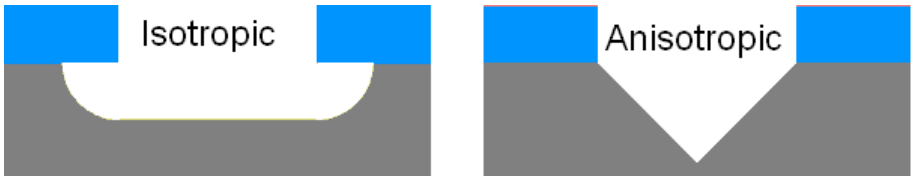

Figure 4.2: *Isotropic vs anisotropic etching profiles. Blue is etch mask, grey is the substrate*

Before discussing the various etch types in more detail it may be useful to briefly mention the difference between isotropic- and anisotropic etches, as shown in Figure 4.2. For fully isotropic etching, the etch rate is the same in all directions. Therefore the horizontal etch rate undercutting the mask edge is as large as the etch rate in the downwards direction. A fully isotropic etch will eventually produce a “dimple” on a substrate, the depth of which will be as large as the undercut. For example, in order to achieve near-ideal hemispheres the mask opening should be small, although too small an opening might cause the etch rate to slow down with time due to a constrained exchange of liquid.

Anisotropic etching, on the other hand, occurs more rapidly along some directions than others. Anisotropy may be caused by the etching technique or by the substrate itself, depending on the etch. For instance, certain wet chemical etches display a higher etch rate along some crystallographic directions than others. A typical example is the etching of silicon by alkali hydroxides to produce inverted pyramids.

In order to obtain good control of the etch, an etch mask needs to be used to dictate which areas of the substrate are etched. The etch mask and etchant need to be selected to match each other, as a very selective etch which leaves the mask nearly un-damaged is required.

4.2.1 Dry etching

Dry etching refers to the removal of surface atoms from a crystal by bombarding the sample with high-energy ions. These violent impacts cause some surface atoms to be dislodged and removed. One type of dry etching is reactive ion etching (RIE), which will be described in more detail in Section 5.1.5. Pillars of silicon may be formed using a monolayer of polystyrene beads as an etching mask for deep-RIE of silicon using a commercial process known as the Bosch time-multiplexed RIE process. Alternating cycles SF_6 and C_4H_8 gas are used. Silicon is etched by SF_6 and the side walls of the holes are passivated by a polymer formed from C_4H_8 gas. In this way aspect ratios of up to 40:1 can be achieved [63]. SEM images of such pillars are shown in Figure 4.3.

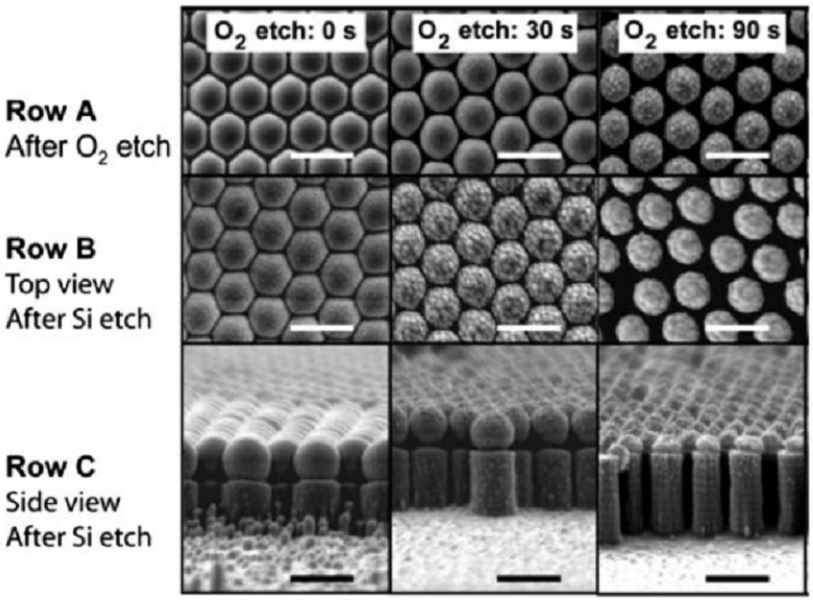

Figure 4.3: *SEM images of silicon pillars obtained using the Bosch deep-RIE process, as used by Cheung et al. [63]*

4.2.2 Wet etching

While dry etching is certainly a very useful method, the emphasis of this work was on wet chemical etching, primarily due to limited access to dry etching facilities. Wet chemical etching is a term used to describe etching processes where the etchant is in liquid form.

Chemical etching

Several silicon-selective wet chemical etches are available, both anisotropic- and isotropic ones. Potassium hydroxide (KOH) solutions etch crystalline silicon anisotropically, preferentially etching {110} surfaces. This gives rise to very characteristic slanted grooves with sidewall angles of 54.7° with respect to the surface of a (100) wafer. The anisotropy can be attributed to small energy differences of the surface states of the different crystal planes. Hydroxide ions from water initially reacts with the exposed silicon to form orthosilic acid, $Si(OH)_4$, which is removed from the surface as neutral molecules. This species then dissociates in solution via an acid-base reaction due to the high pH, eventually forming molecular hydrogen gas which bubbles off the substrate [64]. It should be noted that these bubbles may adhere to the substrate, causing variations in the etch rate. In general a higher temperature- and concentration give more, smaller bubbles and overall higher smoothness of the etch [65].

If KOH etching is performed on a bare wafer, random pyramidal pits are formed which cause scattering of light and enhanced light trapping in a solar cell. This type of surface treatment is used extensively in industry today. It is also possible to do KOH etching through holes in an etch mask. Silicon nitride is frequently used as such a mask material for KOH etching. This is because KOH etches silicon effectively but does not attack silicon nitride; Williams et al. found the etch rate in silicon nitride thin films deposited by plasma enhanced chemical vapour deposition to be negligible [66].

Isotropic etches are also available. The Chemical Polish 5 etch, which is a mixture of nitric acid, hydrofluoric acid and water, is very common. The nitric acid oxidises the silicon, and the silicon oxide is then removed by the fluoride ions. However, no easily accessible materials function well as etch masks for this etch due to inadequate etch selectivity.

Electrochemical etching

Electrochemical etching is a powerful method for the highly controllable etching of a material, including crystalline silicon. The method requires the immersion of the substrate in an etchant electrolyte. The substrate acts as the cathode which is connected to the anode via an external circuit, as shown in Figure 4.4. For the etching process to start, the electrode potential is brought to the level at which surface atoms of the

substrate will be ionised and dissolved. Electrons pass through the wires to complete the circuit. The etch rate is closely related to the current density passing through the substrate. More precisely, it is given as

$$r_{el} = \frac{M}{z \cdot \varrho} \cdot \frac{I}{A} \tag{4.1}$$

where M, z and ϱ are material constants, I is current and A is the etching area [67].

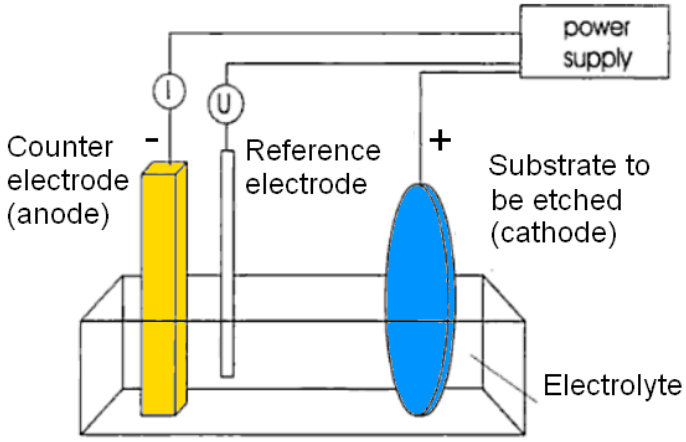

Figure 4.4: *Schematic of electrochemical cell*

For silicon wafers, hydrofluoric acid is typically used as the etchant. For this to be effective, electronic holes have to be generated in the wafer by light absorption. Therefore the substrate is placed in an etching cell which allows the front side of the wafer to be exposed to the HF solution, while the back side is illuminated by a lamp. A platinum control cathode is submerged into the etchant solution and an anode is attached to the back side of the wafer. Photogenerated holes diffuse through the wafer to the side which is exposed to the etchant, thus catalysing the etching reaction [68].

The anodic potential at the surface makes holes diffuse to the interface with the electrolyte, where they cause the oxidation of silicon by reaction with OH^- ions from the solution. The resulting silicon oxide created at the surface is subsequently removed by the hydrofluoric acid.

At high applied potentials, the etch rate will be even across the entire substrate, causing a smooth chemical polish. However, it is also possible to tweak the etch to induce the formation of random networks of pores running into the substrate. This material is known as porous silicon, and the diameter of the pores can be varied from nanometers to micrometers by adjusting parameters such as the wafer doping level or the electric current and bias potential. Porous silicon has mainly been explored for sensor applications, due to its high specific surface area and highly tuneable surface properties.

A crucial aspect of electrochemical etching is that the process preferentially starts at points on the surface where the electric field is concentrated. This is because the etching of silicon is a dissolution process which occurs more rapidly in places where the concentration of holes is high, as explained. One way to achieve such field concentration is to pre-pattern the substrate to create indentations or dips in the surface. Etching then proceeds from these initiation spots ("seeds") to form various kinds of etching profiles which can be tuned by altering the etchant concentration, current density and other parameters [69]. The current density at the pore tip is determined by the light intensity, which allows accurate tuning of the pore characteristics over time [35, 70]. If the parameters are kept constant throughout the duration of the etch, the nanochannels will continue to grow in a diameter self-limiting fashion.

Patterning of the wafer to create such seeds may be achieved in many different ways. Regular photolithography can be used for making holes in a photoresist etch mask, prior to alkaline etching to produce regular arrays of inverted pyramids [70, 71]. The sharp tips of these inverted pyramids are perfectly suited as seeds for the etch. Using seed-catalysed electrochemical etching, a vast variety of patterning geometries have been demonstrated in the literature, a few examples of which are shown in Figure 4.5. The electrochemical etching step itself is quick and easy; the main issue preventing the large-scale use of this technique in price-sensitive applications is the lack of cheap, rapid and scaleable methods for the pre-patterning of the wafer to allow good control of the pore initiation.

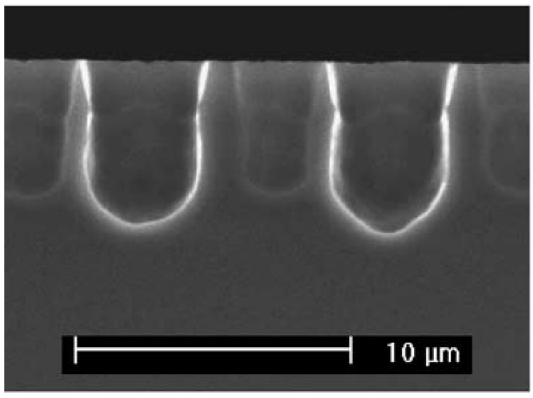

(a) *Image from Föll et al. [72]*

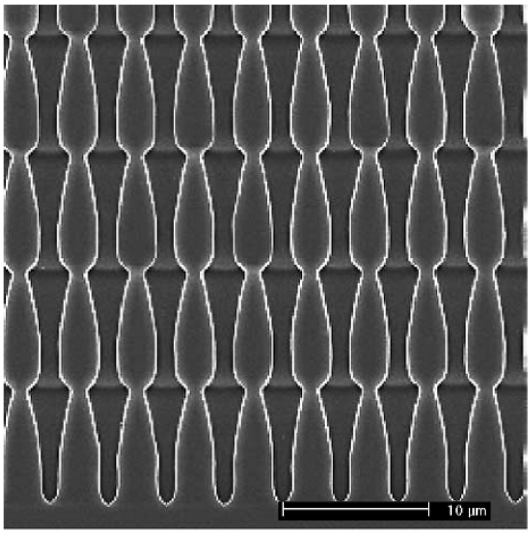

(b) *Tuning of etch pit diameter by current modulation. Image from Müeller et al. [73]*

Figure 4.5: *Cross sections of various geometries fabricated by seed-catalysed electrochemical etching*

Depending on the patterning technique used, defects and imperfections are to be ex-

pected. This can cause anomalies in the neighbouring area of the sample. For instance, if one pit is missing, the electronic holes which would otherwise have concentrated here will instead diffuse to the neighbouring pits, causing a local increased hole concentration. This in turn causes a widening of the etched structures initiated at those locations. Therefore high quality patterning must be achieved to avoid this kind of defect.

Metal catalysed etching

A special kind of chemical etching is the metal-catalysed etching of silicon. Some noble metals such as silver, palladium, platinum or gold can act as a catalyst for the etching of silicon by a mixture of hydrogen peroxide (H_2O_2), hydrogen fluoride (HF) and deionised water. As the chemical etching begins, the silver sinks into the etching holes and continues to catalyse the directional etching just beneath it. The metal particles act as cathodes while silicon acts as anodes. Li et al. [74] studied this process in detail, and proposed the following reaction mechanism:

$$\begin{aligned} \text{Cathode (metal):} \quad & H_2O_2 + 4H^+ + 2e^- \rightarrow 2H_2O + 2h^+ + H_2(g) \\ \text{Anode (silicon):} \quad & Si + 4h^+ + 6HF \rightarrow H_2SiF_6 + 4H^+ \\ \text{Overall:} \quad & Si + H_2O_2 + 6HF \rightarrow 2H_2O + H_2SiF_6 + H_2(g) \end{aligned} \tag{4.2}$$

The noble metal acts as a cathode where the oxidant H_2O_2 is reduced. The holes which are generated in this half-reaction are injected into the silicon in contact with the metal, and the silicon is thus oxidised and dissolved.

An important point about this mechanism is that the holes which are necessary for the etch to progress are provided by the hydrogen peroxide, and as such the etching process should not be very dependent on the doping level. Unlike electrochemical etching, therefore, metal catalysed etching is not very dependent on the doping level of the wafer. The etching is, however, dependent on the crystallographic orientation. The removal of surface silicon atoms obviously requires the breaking of chemical bonds in the crystal. The more strongly a silicon atom is bound, the harder it is to remove. Hence the chemical etching preferentially occurs along non-dense directions. Atoms on a (100) surface have two back-bonds, while atoms on a (110) or (111) surface have three such bonds. Hence, etching preferentially occurs along the <100> directions [75].

Huang et al. [76] explored the use of nanosphere lithography to pattern a wafer with silver islands. Before depositing silver, the diameters of the beads were reduced by reactive ion etching. After exposing these samples to the etching solution, regular arrays of silicon pillars of the same diameter as the protective polystyrene spheres were formed, as the silver coating the surface etched its way into the wafer. Cylinder aspect ratios up to 30:1 (height to diameter) can reportedly be achieved by this method, with nearly vertical side walls. This method is shown in Figure 4.6. The results obtained

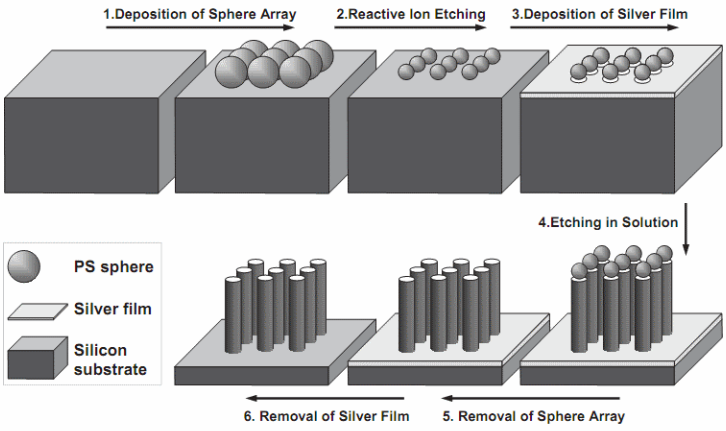

(a) *Schematic of the method*

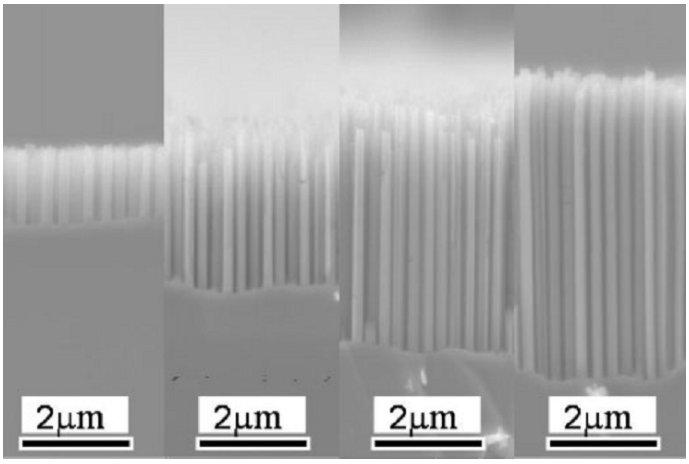

(b) *SEM cross-section image of synthesised structure*

Figure 4.6: *Metal catalysed etch method introduced by Huang et al. [76]*

are fairly similar to those by Cheung et al. [63], who used dry etching to obtain aspect ratios up to 40:1, as shown in Section 4.2.1.

4.2.3 Laser ablation using colloidal microlenses

Some groups have explored the use of a monolayer colloidal crystal as a microlens array for laser processing. When firing a laser beam onto such a structure, the beads concentrate the light beneath their center. If the laser pulses are sufficiently short and energetic, extreme local heating of the substrate beneath the spheres will occur. This may cause local ablation (melting/boiling) of the substrate [77].

Brodoceanu et al. [78] used hexagonal close packed monolayers of silica beads deposited on a (100) silicon wafer as microlenses to create hexagonal arrays of 6 ± 1 nm deep

dimples in the substrate. Their experimental parameters are listed in Table 4.1, and some of their results are shown in Figure 4.7a. It should also be noted that the laser parameters can be tuned such that bumps rather than dents can be formed. This was shown by, among others, Huang et al. [79], also using (100) silicon wafer substrates.

The main difference in experimental parameters between these two groups is the laser pulse length. When ultrashort pulses are used, the power of each pulse is extremely high, such that the energy which is focused beneath each bead cannot dissipate into the surrounding material. Therefore the local heating is significant, causing a small amount of substrate material to be ablated off the surface. When longer pulses are used, a larger amount of material will melt. The bump formation observed by Huang et al. was attributed by the author to the way in which the molten silicon re-solidifies when cooling.

	Brodoceanu et al. [78]	Huang et al. [79]
$\frac{\lambda}{d_s}$	0.89	0.248
Pulse length [fs]	300	23000000
Intensity[mJ/cm^2]	15	30-300
Structure	Dimples (Fig. 4.7a)	Bumps (Fig. 4.7b)

Table 4.1: *Experimental parameters from literature. d_s is the diameter of the spheres in the monolayer template*

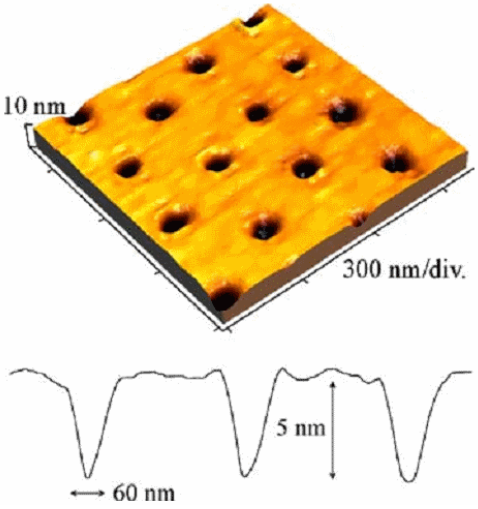

(a) *Results from Brodoceanu et al. [78] Dimple formation using a 265.7 nm Ti:sapphire laser with a 300 fs pulse.*

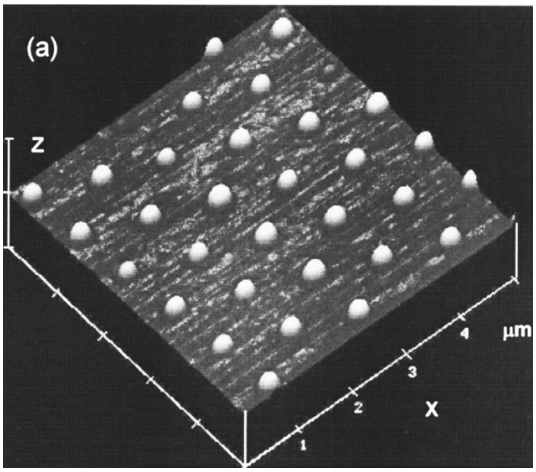

(b) *Results from Huang et al. [79]. Bump formation using a 248 nm KrF excimer laser with a 23000000 fs pulse*

Figure 4.7: *Dimples and bumps achieved by laser ablation on patterned (100) Si wafers using colloidal monolayers as microlenses*

Brodoceanu et al. found that the laser wavelength and bead diameter need to be matched in order for the beads to function as effective microlenses. The field enhancement factor is a measure for how strongly the light is concentrated beneath each bead. In general, the wavelength should be less than the bead diameter for the field enhancement factor to be high enough to achieve significant ablation; that is, $\frac{\lambda}{d_s} < 1$. Brodoceanu calculated that the factor drops off by a factor of 2 when changing the $\frac{\lambda}{d_s}$ ratio from 0.89 to 1.3.

Monolayers of polystyrene and silica beads have both been successfully used as templates for laser ablation. With a laser intensity above approximately 45 mJ/cm^2 polystyrene beads are removed almost completely from the surface, while removing silica beads requires a laser intensity almost twice as high [79].

Chapter 5

Methods

In this chapter, supporting information about some of the more key experimental instrumentation used in this project will be presented. This chapter is not meant to give an exhaustive explanation of the methods; only the aspects considered essential for this work will be discussed. The reader is encouraged to consult the cited references if more details are requested.

First, equipment used to synthesise the structures shown in this thesis will be described, before the characterisation tools are discussed.

5.1 Synthesis equipment

5.1.1 Spin coating

Spin coating is used to fabricate monolayer colloidal crystals. Spin coating is a simple technique which is widely used in the microelectronics industry for deposition of thin films, for instance photoresist for photolithography. The sample is wetted by the solution to be spin coated and placed on a sample stage. A vacuum chuck holds the sample in place, and the rotation speed of the stage is set. A schematic of a spin coater system is shown in Figure 5.1a.

Typically the speed of a spin coater may range from 0 up to 5000–10000 rotations per minute (RPM). The centripetal force causes the solution to spread out and form a thin film of uniform thickness on the substrate. The thickness of Newtonian fluids, when spin coated, is expected to depend on the angular frequency ω as $T \approx \omega^{-b}$, with the exponent b typically around 0.5. This value depends on the viscosity and properties of the fluid. It has been observed that for colloidal suspensions, a very high solids fraction causes the exponent to increase, resulting in a thinner film than could otherwise be expected for a given angular frequency [51]. Figure 5.1b shows an example where experimental data of a sphere solution is fitted to the spin coating power law.

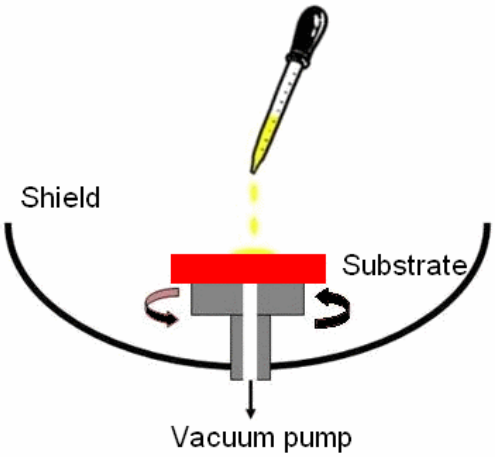

(a) *Schematic of a spin coater system*

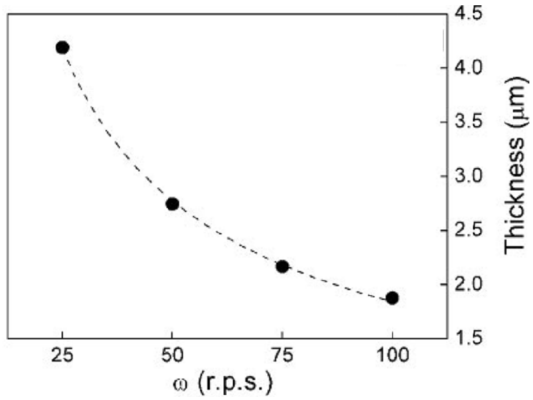

(b) *Thickness of spin coated film for different angular frequencies. Dotted line shows the fit to the spin-coating power law, with exponential* $b = 0.59$. *30:30:40 volume fractions of polystyrene/ethanol/water. Results from Mihi et al. [51]*

Figure 5.1: *Spin coating*

5.1.2 Plasma enhanced chemical vapour deposition

Chemical vapour deposition is a collective term used to describe several thin film deposition processes in which gaseous film precursors react on the substrate to form a film. The surface reaction has a certain activation energy barrier which needs to be overcome. The well known Arrhenius equation is commonly used to relate the activation energy barrier and temperature of a reaction [80]:

$$k = Ae^{-E_a/RT} \tag{5.1}$$

where k is the rate (speed) of reaction, E_a is the activation energy barrier, R is the universal gas constant and T is the temperature. From this equation it is seen that the necessary reaction temperature $T \propto E_a$. Thus, a lower activation energy barrier leads to a lower required activation temperature.

In thermal CVD, the gaseous precursors are neutral molecules, and the activation energy is supplied by simply heating the substrate. In plasma enhanced chemical vapour deposition (PECVD), on the other hand, the precursors are present in the form of reactive ions and free radicals in a plasma. These species are unstable and thus have a far lower activation energy barrier for the surface reaction, and consequently the reaction can take place at lower temperatures than in thermal CVD [81]. This is a distinct advantage for processes involving delicate and temperature sensitive substrates. The activation energy barriers for the two processes are illustrated in Figure 5.2.

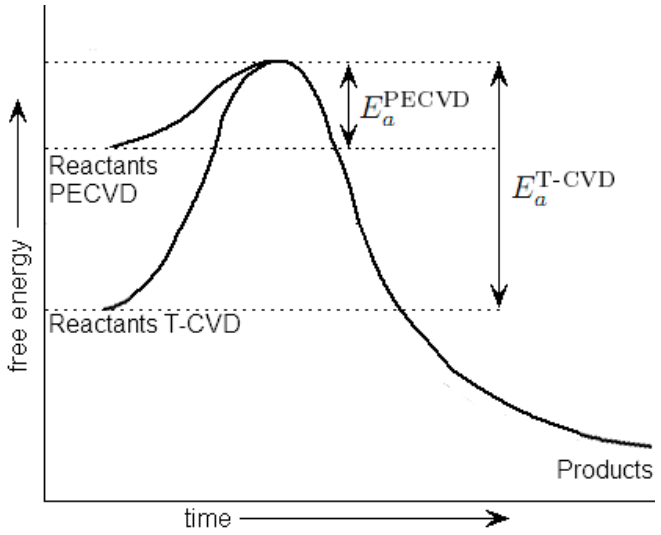

Figure 5.2: *Activation energy barriers for PECVD and T-CVD*

In a PECVD system, precursor gases are fed into an oscillating electric field containing free electrons moving very rapidly back and forth. Usually the alternating current frequency is in the megahertz range. High energy collisions between electrons and precursor molecules can cause the formation of radicals or ions in the plasma. Due to the instability of these species, deposition will occur on any suitable surface, including the walls of the chamber. To gain some control of the depositon, the substrate is usually placed directly onto one of the electrodes, whose temperature can be adjusted [81]. This also means, however, that the surface will be bombarded by high energy species which can cause undesired sputtering and surface damage in addition to film buildup.

In this work, an Oxford Plasmalab 100 PECVD system at the IFE Solar Department was used for the deposition of silicon nitride films.

5.1.3 Thermal evaporation of metal

Thermal evaporation is a commonly used method for depositing thin films of material onto a substrate. In simple terms, the source material to be deposited is melted in a vacuum chamber and caused to diffuse to the substrate, where it settles and condenses to form a film.

The source material is usually either in the form of a pellet or a wire, the latter for continuous feeding into a carrier (or "boat"). An electrical current is passed through the boat, causing local heating and hence evaporation of the source material therein. Typically the boat is fabricated from some intermetallic mixture, often containing wolfram, which offers the right electrical resistivity and corrosion resistance [82].

Due to the vacuum in the deposition chamber, most of the evaporated atoms migrate to the substrate without interacting with other species. This gives a highly directional

deposition. Thermal evaporators are also commonly equipped with a rotating sample stage to avoid any shadowing effects during the deposition. A schematic of a thermal evaporator system is shown in Figure 5.3.

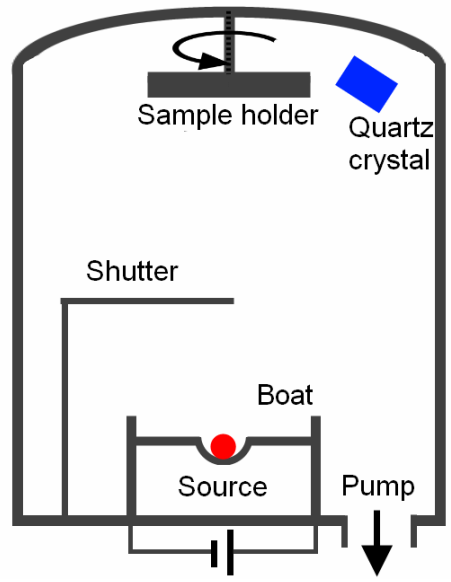

Figure 5.3: *Schematic of thermal evaporator system*

The deposition rate of the film is measured by a quartz crystal, whose vibrational frequency depends on the amount of material deposited onto it, allowing the film thickness to be determined with sub-Ångström precision.

A Kurt J. Lesker NANO 36 thermal evaporator system at the IFE Solar Department was used in this work.

5.1.4 Laser ablation

Laser ablation is a technique for the removal of material by laser irradiation. Typically one uses very short (pico- or femtosceond) laser pulses of very high energy. The short pulses and high energy prevent much heat from dissipating beyond the illuminated patch. If the laser parameters are adjusted properly, the laser beam can cause the irradiated material to melt and evaporate [83].

Here, a J-1030-515-343 FS industrial system from Oxford Lasers with a s-Pulse HP laser from Amplitude Systems located at the IFE Solar Department was used for laser ablation.

5.1.5 Reactive ion etching

Reactive ion etching is a powerful dry-etching method for substrate patterning. Just as in PECVD, a sample is placed on an electrode in a vacuum chamber and a plasma is created by an alternating electromagnetic field, as seen in Figure 5.4. The negatively charged plasma bombards the positively charged sample stage. If the plasma energy is high enough, this can cause sputtering or local ablation of the substrate. This is in contrast to PECVD, where the precursors in the plasma are less energetic and react to build a film on the substrate.

It is worth noticing that many industrial apparatus are capable of both PECVD and RIE operation.

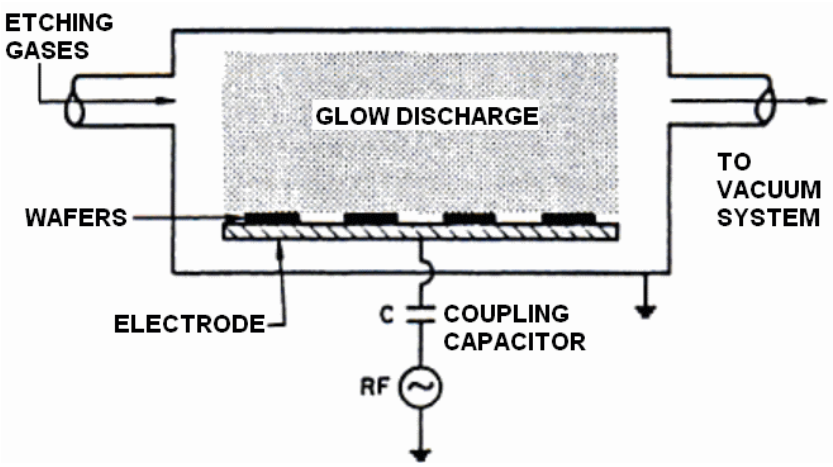

Figure 5.4: *Schematic of reactive ion etching chamber. Figure modified from [84]*

5.2 Characterisation tools

5.2.1 Optical characterisation

An integrating sphere is a very useful tool which allows the reflectance and transmittance of a sample to be determined. The inside of an integrating sphere is covered by a diffuse reflective coating with a reflectance close to unity over the entire relevant wavelength spectrum. The purpose of the sphere is to collect light and feed it to a detector, thus much amplifying the signal which is registered. By illuminating the sample with a light source, the light from the sample may be collected by the sphere and used to calculate the reflectivity or transmittance, depending on the experimental setup.

The light source may either emit at all wavelengths simultaneously (white light) or a monochromator may be used such that the wavelength is changed in steps throughout

the measurement. In either case the detector records the reflected intensity as a function of incident wavelength.

Integrating sphere measurements are most often relative rather than absolute, meaning that in order to recover the reflectivity of the sample the signal must be compared to that of a calibration material of known reflectivity, as shown in Figure 5.5. Sample reflectivity is then calculated by using the following formula: [85]

$$R_s^{measured}(\lambda) = \frac{S_s(\lambda)}{S_c(\lambda)} \cdot R_c(\lambda) \tag{5.2}$$

where $R_c(\lambda)$ and $S_c(\lambda)$ are the reflectivity and measured intensity spectrum of the calibration material respectively while $S_s(\lambda)$ is the measured intensity spectrum of the sample. Also, the recorded signal needs to be multiplied by a correction factor to account for the relative port areas.

The correction factor can be shown to be [85, 86]

$$k \approx \frac{1 - R_w \cdot (1-p) - R_c(\lambda) \cdot p}{1 - R_w \cdot (1-p) - R_s(\lambda) \cdot p} \tag{5.3}$$

where R_w is the reflectivity of the sphere walls and p is the sample port area divided by the sphere area. The corrected reflectance is then determined as

$R_s^{corr}(\lambda) = k \cdot R_s^{measured}(\lambda)$.

The integrating sphere setup used here consisted of an Ocean Optics HL-2000-FHSA light source with wavelengths from 260-2000 nm, connected to spectrometers from the same manufacturer of models QE65000 (200–1100 nm) and NIRQuest (900–1700 nm). The internal sphere diameter was 60 mm, and the relative sample port area $p = 0.01$. The sphere wall reflectivity R_w of a brand new sphere wall coating of this kind is reported by the manufacturer to be closer to 0.99, but such high-reflectivity coatings are known to degrade over time due to ultraviolet radiation. Earlier investigations [86] revealed that the reflectivity could be approximated to 0.98 over the entire wavelength range. This setup was used to measure total reflectivity for an angle of incidence of 8°, which was the only angle of incidence allowed by the experimental setup. The sample is placed on a side port on the sphere and light is introduced through an other opening, and the output signal is detected. By first detecting the reflected signal from a reference sample and then the sample of interest, Equation 5.2 can be used to recover the reflectivity of the sample. This is shown in Figure 5.5.

5.2.2 Atomic force microscopy

Atomic force microscopy (AFM) is a type of scanning probe microscopy. The technique uses a very sharp tip which is rastered across the surface of the sample in very close

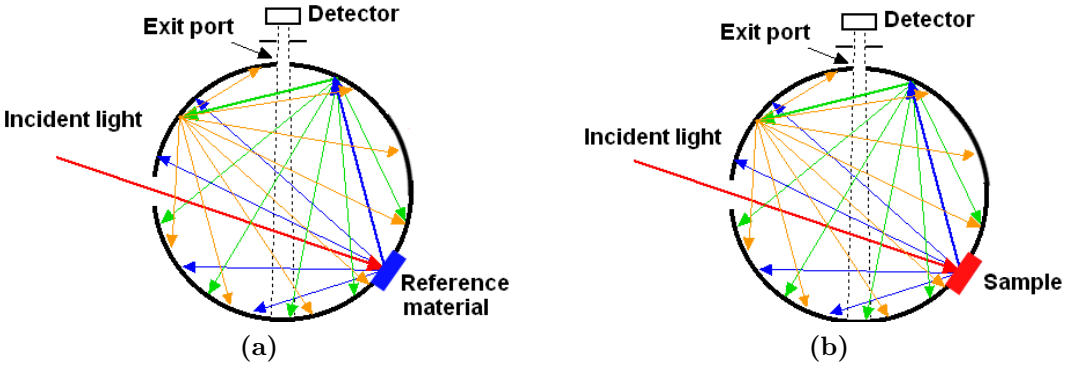

Figure 5.5: *Integrating sphere setup for reflectivity measurements*

proximity. As it does so, the tip is affected by various surface forces which cause it to deflect. By accurate measurement of these deflections, information about surface topography, magnetism etc of the sample can be extracted.

The tip is normally made from silicon or silicon nitride, with a tip radius in the order of 20–200 nm [87]. As it scans across the surface it is either attracted or repelled by the surface. These tiny tip movements are registered by shining a laser beam onto the tip and measuring the deflection of the beam by a photodetector, as shown in Figure 5.6. In this way, near-atomic lateral resolution can be achieved, with Ångstrøm height sensitivity. The major downside of the method is its slowness and small scan areas, typically in the range of 50x50 µm. Also, it may be difficult to know where exactly on the sample one is measuring, unless an optical microscope is used together with the AFM to ease the sample alignment.

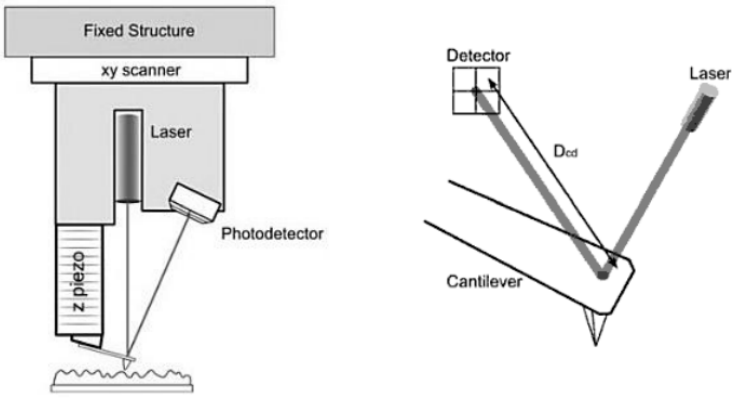

Figure 5.6: *Schematic of an AFM setup. Images from [88]*

The AFM used in this work was a Surface Imaging Systems Picostation located at the IFE Physics Department.

5.2.3 Scanning electron microscopy

Scanning electron microscopy is a powerful and much used type of electron microscopy. In many ways it resembles optical microscopy, except a beam of high-energy electrons is used rather than light. The electron beam is focused by electromagnetic lenses inside the microscope column under vacuum, before interacting with the sample. The scattered electrons and radiation can be collected and used to produce high-resolution images as well as for extracting information about the composition of the sample [87]. A schematic of a SEM column is shown in Figure 5.7.

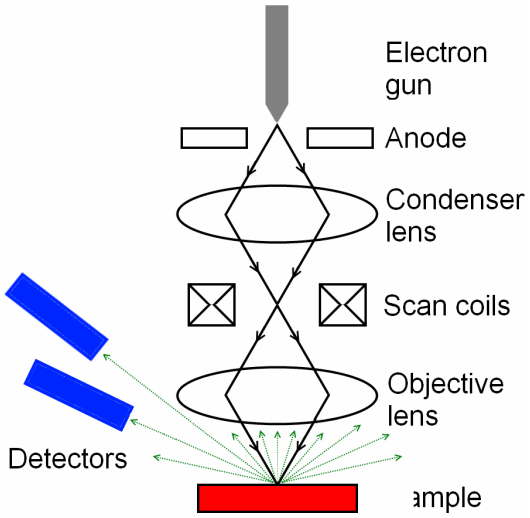

Figure 5.7: *Schematic of a scanning electron microscopy setup. Green dotted arrows represent the scattered signal*

For most samples, most incoming electrons will lose their energy through inelastic scattering events within a few nanometers to a few micrometers beneath the surface, depending on beam energy and the sample properties. In these collisions, much of the energy of the incoming beam is absorbed and causes the emission of secondary, low-energy electrons from the sample, which can be detected and used for imaging.

The incident electron beam will also cause the emission of some high-energy electromagnetic radiation from the sample. This may happen in the event that the energy of the incident beam is high enough to ionise atoms in the sample. When an outer-shell electron subsequently decays to fill the vacant state, a high-energy photon is emitted, of a particular frequency which is characteristic of the material. Hence, by studying the emitted x-ray spectrum from a sample investigated in the SEM, information about the elemental composition of the sample can be extracted. This method is referred to as energy-dispersive X-ray spectroscopy (EDS) [87].

The SEM used here was a Hitachi S-4800 at IFE Materials and Corrosion.

Chapter 6

Experimental

In the previous chapter, the working principles of some of the experimental equipment essential to this work were explained. Now, the precise details of the experiments conducted will be presented. Where appropriate, some additional motivation and background information will also be included.

The process for making monolayer colloidal crystal templates is developed first. These templates are then used to create silver nano-islands for plasmonic scattering, as well as various diffraction gratings. The work on diffraction gratings is divided into two parts. First, four different techniques are explored for the patterning of wafers with shallow indentations, intended for use as initiation points or seeds for a later electrochemical etch. Then, arrays of dielectric cylinders are fabricated by metal catalysed etching.

6.1 Synthesis of colloidal crystal templates

6.1.1 Substrate pre-treatment

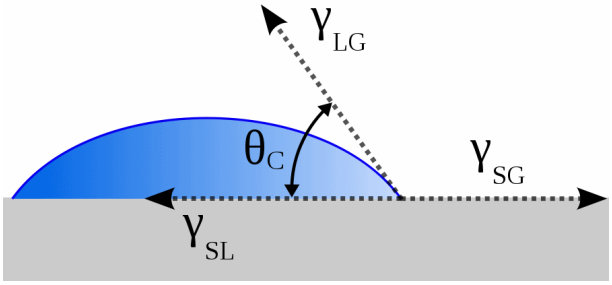

Figure 6.1: *Schematic showing the contact angle θ_c for a liquid on a substrate*

In order to obtain good quality colloidal crystals by evaporation induced self assembly, it is imperative that the substrates be hydrophilic. Cleaned silicon wafer substrates

are, however, highly hydrophobic and therefore require a pre-treatment to decrease the contact angle with water, θ_c, as shown in Figure 6.1. In initial experiments, several different surface treatments were attempted, including piranha etching (1:4 ratio of H_2O_2/H_2SO_4) [51], growing a thermal oxide, or soaking the substrates for 24 hours in sulphuric acid [45]. The best results, however, were obtained using an RCA-1 chemical treatment similar to that proposed by Rakers et al. [47]:

1. Put 515 ml DI-water in a glass beaker and add 85 ml NH_3
2. Heat the solution to 77°C
3. Add 100 ml H_2O_2 and maintain a solution temperature of 70°C. Wait 2 minutes for solution to start bubbling
4. Submerge silicon substrates into solution for 15 minutes
5. Remove substrates and clean in copious amounts of DI water

This procedure creates a nanometer thin silicon oxide film on the surface of the wafer, which much improves wettability by water. During the RCA procedure, hydrophilic radicals absorb on the silicon surface altering the surface chemistry. Literature reports indicate a wetting angle of 2-3° for substrates prepared in this manner shortly after treatment, increasing to 25° after four days exposed in an air-tight container [89]. The substrates are therefore stored in ethanol, which is reported to significantly reduce the ageing effect. [45].

Colloidal spheres, both polystyrene (PS) and silica, were purchased from Bangs Labs Ltd. in 10% aqueous suspensions. These were used for the formation of colloidal crystals, as will now be described.

6.1.2 Monolayer synthesis

Monolayers were made by spin coating a solution of beads, a technique described in Sections 3.2.2 and 5.1.1. Many factors will affect the quality and properties of a monolayer colloidal crystal fabricated by spin coating, as has been touched upon in Section 3.2.2. The most important ones are:

- Composition of spinning solution, including volume fraction of spheres
- Spinning speeds- and durations. The spin coater used allowed for three different spin speeds with individually selectable ramping rates
- Atmosphere control (humidity, temperature, air flow across substrate)

All these parameters were investigated systematically in this work. Where appropriate, an Eppendorf 5804 tabletop ultracentrifuge was used to increase the concentration of the sphere solution before use. Centrifugation was done for 15 minutes at 1400 G for diameter $d_s > 800$ nm, 2200 G for $500 < d_s < 800$ nm or 9300 G for $d_s < 500$ nm, in agreement with suggestions from the sphere supplier [90]. For centrifugation, the following steps were followed:

1. Put sphere solution (solids fraction 10%, from manufacturer) into a test tube designed to be used with the ultracentrifuge
2. Centrifuge at the designated rotational velocity and time (see above)
3. Remove some of the supernatant liquid above the sedimented beads, such that the solid fraction is increased to the desired level

Prior to spin coating, it is necessary to place the prepared solution in an ultrasonic bath to break up any aggregates of spheres which may have formed. The required sonication time depends greatly on the type of beads used. The polystyrene beads used in this work arrived from the manufacturer functionalised with sodium dodecyl sulfate surfactant (SDS), which renders the surfaces hydrophilic to prevent agglomeration. Thus, initial experiments revealed that 5 minutes of ultrasonication was sufficient to break up the clusters. The silica are un-functionalised, and although their natural hydroxide surface is hydrophilic, a certain degree of agglomeration was observed. Initial experiments to investigate the importance of the duration and temperature of the sonication were performed, including sonication for 5-6 hours at 24-27°C as suggested by Kumar [50]. However no correlation between temperature/time and degree of agglomeration could be found. Therefore it was decided to sonicate for 5 minutes for silica beads and PS beads alike.

After centrifugation and sonication, a few drops of solution were placed on a substrate, which was tilted manually to achieve complete wetting, before spin-coating. The exact experimental spin coating parameters are presented later.

6.2 Metal islands for plasmonics

Nanosphere lithography was used to fabricate regular arrays of metallic nano-islands on a substrate. First, a monolayer of beads was made, before metal was deposited on top using the vapour deposition system described in Section 5.1.3. A silver pellet was placed in the heating boat and a uniform film of silver of a selected thickness deposited onto the substrate. Various thicknesses were explored. After metal deposition, the beads were removed by sonication in a bath of ethanol for 2 minutes and the substrates flushed with DI water.

Monolayer templates with bead diameters 490 nm and 1000 nm were fabricated on silicon substrates and used to study the plasmonic effect.

6.3 Diffraction gratings I. Seed formation

In Section 4.2, various experimental techniques for the synthesis of diffraction gratings structures in silicon were discussed. Several of the techniques described there are suitable for the fabrication of nano-indentations in a wafer, which should work very well as initiation points or seeds for chemical- or electrochemical etching to create various diffraction gratings. In this section, four approaches will be attempted.

As mentioned in Section 2.2.2, PhD candidate Jo Gjessing at the Institute for Energy Technology has developed a simulation platform which allows the optical properties of many kinds of diffraction gratings to be determined. This is a useful tool for selecting the target structures for synthesis in the lab. For thin wafers, Gjessing calculated that arrays of hemispherical dimples, cones, inverted pyramids and cylinders with periods around 1 µm give very high reflectivity due to a high degree of scattering into non-zero diffraction orders [21]. For this reason, 2D hexagonal arrays with periods around 1000 nm were investigated for many of the diffraction gratings synthesised in this work. In practise this meant selecting colloidal beads with diameters around 1 µm for nanosphere lithography.

6.3.1 Metal catalysed etching

Silver islands on a silicon substrate may, when exposed to a solution of HF/H_2O_2, catalyse the local etching of silicon beneath the silver particle to form pits or channels. This was explained in Section 4.2.2. Metal catalysed etching was used to create pits in a wafer for use as seeds in an electrochemical etch. The synthesis steps proposed by Huang et al. [76] were followed.

First, a 40 nm thick film of silver was deposited onto the samples by thermal evaporation and the beads were removed by sonication in ethanol for 2 minutes. The samples were then submerged in a 4.6 M HF / 0.44 M H_2O_2 etch bath at room temperature. The etch rate of silicon by this mixture was reported by Huang et al. to be 5.5 nm/sec at these conditions. Initial experiments revealed that the etch depth varied slightly across a sample, but with an etch rate around 5 nm/sec. After the etch, samples were rinsed in DI water and dried.

6.3.2 Laser ablation using colloidal microlenses

Laser ablation was used in two different experiments. First, monolayer colloidal crystals were deposited on a plain (100) silicon wafer and illuminated with picosecond laser pulses, with the aim of using the beads as microlenses for creating dimples in a wafer. Second, monolayer colloidal crystals were fabricated on a wafer which had been coated with a 80 nm thick silicon nitride layer by PECVD. The idea here was to use the laser beam to burn holes in the silicon nitride. The holey nitride mask may then later be

used as a mask for the chemical etching of silicon, such as for instance an alkali etch to create arrays of inverse pyramids in the wafer.

Microlenses on bare silicon wafers

Monolayers of 1 µm polystyrene beads were prepared on two silicon wafer samples before laser ablation. As explained in Section 4.2.3, the two most important parameters to investigate at this point were the laser wavelength and intensity. To explore this, one sample was bombarded with ultraviolet light (343 nm) and the other with visible light (wavelength 515 nm). Each sample was divided into four parts, and the laser intensity varied from quadrant to quadrant. The pulse length was set to 3 ps, and the focus diameter was approximately 30 µm for visible light and 10 µm for ultraviolet light. The laser intensity is assumed to follow a Gaussian distribution within the focus spot. The laser beam was rastered across the sample, firing a single pulse at each position. With the beam moving at 50 mm/s, an entire sample could be manufactured in a matter of minutes.

Initial experiments revealed that a pulse energy of 100 nJ was necessary to achieve ablation when using visible light, while the necessary intensity when using ultraviolet light was an order of magnitude less. Due to the smaller spot size of the ultraviolet light, the required pulse energy is in other words similar for both wavelengths. Limitations in the laser's intensity detector made it impossible to determine the actual laser power used in the UV irradiated samples. Four different pulse energies were explored for each wavelength.

After laser ablation, the polystyrene microbeads were removed by sonication in acetone for 2 minutes. Acetone was chosen rather than ethanol because it dissolves polystyrene, including any molten remains that may be sticking to the surface.

Microlenses on silicon nitride coated wafers

Based on the positive results obtained using visible light on bare silicon wafers, attempts were also made at using this technique for burning holes in a silicon nitride film on a wafer. The experimental approach was otherwise identical.

6.3.3 Selective alkali etching through silver etch masks

As was described in Section 4.2.2, alkali hydroxides such as potassium hydroxide (KOH) etch silicon anisotropically to create inverse pyramids, while the etch rate in silver is negligible [66]. Attempts were made to use a pattern of silver as a mask to restrict the size and positioning of the inverse pyramids formed by the etch. To investigate the feasibility of this technique, random patterns of silver were formed by first creating

a 15 nm thick silver film on a silicon wafer sample by thermal evaporation, and then heat treating the wafer at 200°C for 15 minutes. Due to the high contact angle between silver and silicon this heat treatment causes the silver film to "curl up" and form thicker structures such as droplets or islands with exposed silicon wafer inbetween.

Alkali etching was done using a 47% concentration KOH solution at a temperature of 80°C. At these conditions the etch rate on {110} planes of silicon is approximately 700 nm/min [64, 91].

6.3.4 Selective alkali etching through silicon nitride etch masks

As an alternative to the silver etch mask, silicon nitride films created by nanosphere lithography were also explored as an etch barrier for KOH etching. The aim was to create hexagonal patterns of inverted pyramids in a wafer. To the best of our knowledge, this method has not been demonstrated in the literature before. The details of this novel method are explained below.

Step 1. Silicon nitride deposition by PECVD After creating a monolayer of 800 nm silica beads, a thin layer of silicon nitride was deposited onto this template by plasma enhanced chemical vapour deposition (PECVD). The precursor gases were N_2, NH_3 and SiH_4. As described in Section 5.1.2, the feed rate of the precursors as well as the deposition temperature and radio frequency (RF) power are important parameters that affect the quality and properties of the film. Various RF powers and deposition temperatures were attempted.

Step 2. HF etching to enlarge holes in mask To enlarge the holes in the nitride mask, where the wafer was exposed, some samples received a gentle HF-dip to etch away some nitride. The desired etch durations were determined after performing AFM and SEM scans of deposited etch masks to determine the profile heights.

After enlarging the holes, the beads were removed by sonication in ethanol for 2 minutes and the samples were flushed with DI water. Perceivably this step could also be performed directly after Step 1, but it was observed that the beads could more easily be removed after the nitride capping had been weakened by the rapid HF dip. With this method, no colloidal beads could be detected on the substrates by optical microscopy and SEM after processing.

Step 3. Potassium hydroxide etching The KOH etching for creating inverse pyramidal dimples in the wafer was performed in the same way as in the previous method, using a 47% concentrated KOH solution at a temperature of 80°C. Following the KOH etching step, the nitride mask was stripped off the wafer by a 10 minute dip in a 5% HF solution.

6.4 Diffraction gratings II. Dielectric cylinders

Metal catalysed etching was also used for the fabrication of cylinders of silicon. The process steps were exactly the same as when fabricating pits, as described in Section 6.3.1, except the bead diameter was reduced by reactive ion etching prior to silver deposition. This was performed at Michigan Technological University. The etch was done at a power density of 100 W/m^2, 50 sccm of O_2 and a pressure of 0.135 Torr.

After this, silver was deposited before removing the beads and performing the etch.

The optimal height and diameter of the pillars was determined by simulation. An example of such a calculation to determine the optimum height and diameter is shown in Figure 6.2. From this figure we can see that a radius around 350–400 nm and a pillar height of 200–400 nm causes a high fraction of the incident light power to be diffracted into higher (non-zero) diffraction orders.

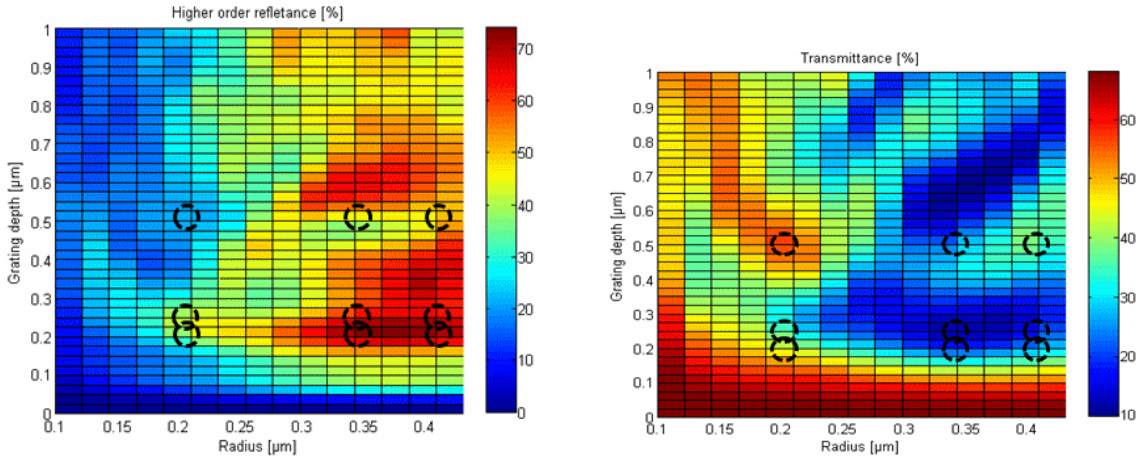

(a) **(b)**

Figure 6.2: *Simulation to determine the power of light scattered into non-zero diffraction orders. Reflection (left) and transmission (right) of a hexagonal array of silicon pillars in air, as a function of pillar height and radius. Light is incident from the front side of the wafer, with the diffraction grating on the back side. Simulations by UiO PhD candidate Jo Gjessing*

Chapter 7

Results and Discussion

In this chapter the results from the experiments will be presented and discussed. First, it will be shown that good quality monolayer colloidal crystals could indeed be formed by spin coating. Then, the monolayers are used as templates to produce metal islands for plasmonics, silicon cylinder diffraction gratings and seeds for electrochemical etching.

For easy referencing, this chapter will follow the same structure as the Experimental chapter.

7.1 Synthesis of colloidal crystal templates

As explained in Section 6.1.2, a number of factors will affect the formation of monolayers by spin coating. These parameters were explored systematically in an attempt to develop a method for the rapid and repeatable production of high-quality crystalline monolayers. The results of these investigations will now be presented.

The experimental parameters of the samples referred to in this section are given in Table 7.1.

7.1.1 Effect of spinning speed regime (rpm)

The first parameter to be investigated was the rotational speed of the spin coater. For these initial experiments, the main concern was the macroscale homogeneity of the samples rather than the monolayer quality per se.

The spin coater used here allowed for three different spin speeds, each with individually selectable ramp up/down rates. It was found that spinning first at a high speed and then more slowly allowed for back-diffusion of solution from the wafer edges, which left clearly visible thick multilayer streaks on the surface. This left the samples looking highly non-uniform on the macroscopic scale. Gradually increasing the spinning speeds

	S21	S22	S29	S16	S47
Sphere concentration [%]	2.5	2.5	2.5	5	30
Water [vol%]	97.5	97.5	–	45	70
PEG [vol%]	–	–	–	50	–
Ethanol [vol%]	–	–	97.5	–	–
Spin stage # 1 [RPM/s]*	300/15	300/15	1000/2 x2**	300/15	300/1
Spin stage # 2 [RPM/s]	1500/120	500/120	350/120 x2	3000/120	7500/180
Spin stage # 3 [RPM/s]	–	–	–	6000/120	–

Table 7.1: *Summary of experimental parameters of samples investigated in this section, to highlight the effect of extreme conditions.*
** RPM/s = rotations per minute and duration (in seconds)*
*** Double deposition*

eliminated this problem and left the samples looking far more homogeneous to the eye and in the optical microscope. The higher the final spin speed the more homogeneous the samples looked on the macro scale. This was a general trend independent of the solids fraction of the spinning solution. When using aqueous suspensions, the final spinning speed should be in excess of 4000 RPM to avoid macroscale inhomogeneities.

However there is a tradeoff involved: higher final spin speeds give poorer wafer coverage, as the centripetal forces are increased, causing the spinning solution to spread out more. This effect becomes very clear when using low concentrations of spheres, as illustrated in Figure 7.1 for the case of a dilute 2.5% solids fraction. For this reason, in order to be able to use high spin speeds, other parameters need to be adjusted to obtain complete wafer coverage.

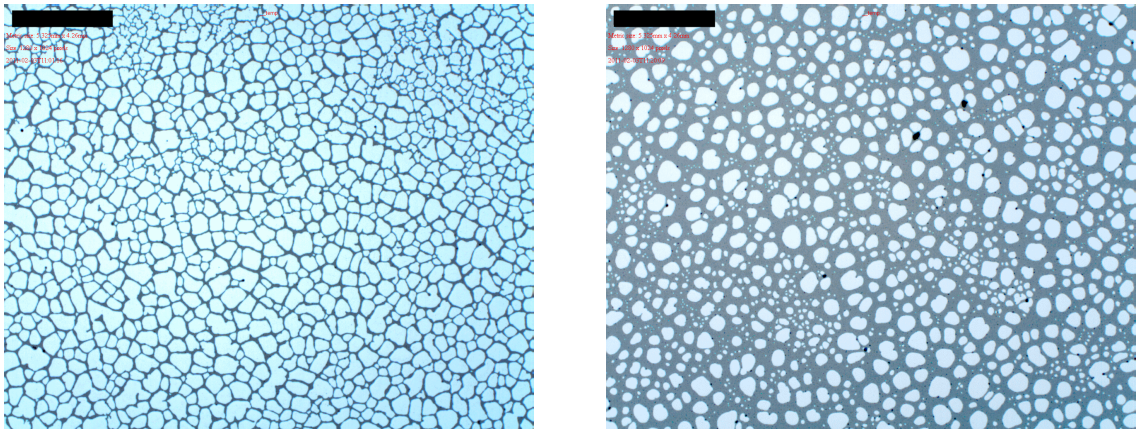

(a) *Sample 21, high spinning speed* **(b)** *Sample 22, low spinning speed*

Figure 7.1: *Effect of final spinning speed. Dark areas are monolayers, light areas represent bare wafer. 2.5% sphere concentration, aqueous suspension. Scale bars 1000 µm*

7.1.2 Effect of multiple spin coatings

Following the initial problems obtaining complete wafer coverage, it was decided to try spin coating on the same substrate multiple times in succession. The idea was that the second spin coating would cause the holes from the first deposition to be filled. However this approach was not successfull; the second deposition formed another holey grid on top of the first layer, as shown in Figure 7.2. This method was therefore abandoned.

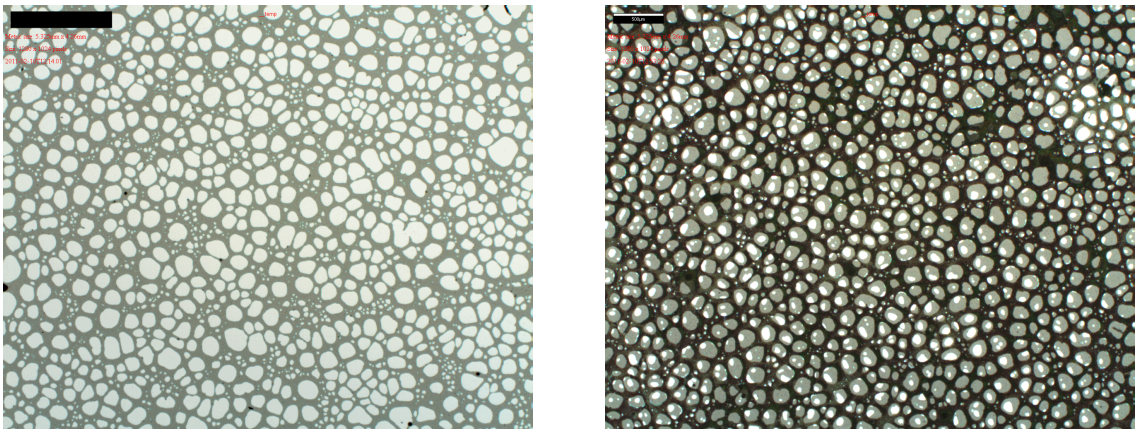

(a) *First layer* **(b)** *After deposition of second layer*

Figure 7.2: *Effect of multiple layer deposition. Sample 29.*

7.1.3 Effect of solvent viscosity

Other groups, noteably McFarland et al. at Corning [42, 43], have had great success using viscous solvents rather than water for spin coating. This was described in Section 3.2.2. Therefore it was also decided to investigate this approach here. Initial tests were carried out with polyethylene glycol (PEG-400) as the solvent. This is a water soluble polymer of average molar mass 400 g/mol, giving viscous solutions when mixed with water. Spin coated samples using this solvent turned out to have highly randomised ordering of spheres as well as incomplete wafer coverage. While the viscosity of a PEG solution is easily tuneable by dilution, this polymer was considered unsuitable for further experiments as it cannot be removed by evaporation.

Therefore other viscous solvents, namely glycerol (boiling point 290°C) and monoethylene glycol (boiling point 197.3°C), were investigated. However both these solvents inhibited the formation of large crystalline domains, and amorphous distribution was dominating. Note that this was the case independent of the solids fraction of the spinning solution, as well as the rotational speed of the spin coater.

It is believed that the viscosities of the solutions investigated here were so high that sphere diffusion and ordering was inhibited due to the high drag on moving particles.

The random thermal motion is slowed down, preventing the beads from settling in the most energetically favourable close-packed conformation. Towards the substrate edges the viscous solutions formed flow line patterns of thicker coverage, which was also deemed to be a sign of too high viscosity. This can be seen in Figure 7.3.

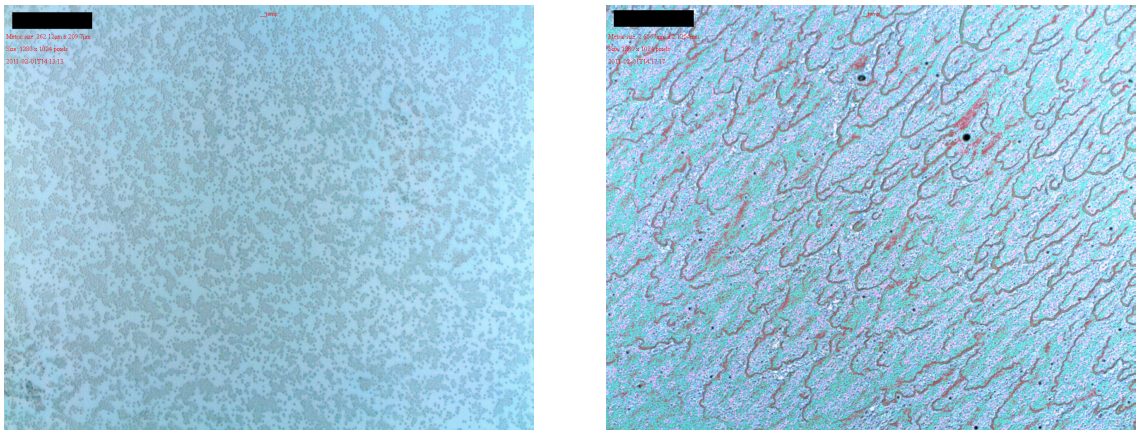

(a) *Randomly distributed spheres at center of substrate. Scale bar 40 µm*

(b) *Flow lines towards substrate edges. Scale bar 400 µm*

Figure 7.3: *Results using a viscous solvent, Sample 16*

Because of the poor quality of the samples fabricated using viscous solvents, this avenue was not explored further.

7.1.4 Effect of solvent boiling point and atmosphere humidity

As mentioned in Section 3.2.2, the humidity of the atmosphere and the solvent boiling point (and hence vapour pressure) are also important parameters. Unfortunately it was not possible to control the humidity during spin coating in any accurate way, because an atmosphere control chamber was not available. Therefore only rudimentary testing could be done, by placing some samples inside a teflon box along with some water droplets, and then spin coating the entire box. This was observed to slow down the rate of evaporation significantly. However, far more testing would be required in order to determine the precise impact of this method. The problem observed here was that the rate of evaporation was simply too low, such that it was necessary to spin coat for several minutes for the spinning liquid to evaporate. By that time, most of the colloidal beads had disappeared from the sample rather than self-organising into monolayers.

Spin coating was also done using ethanol as the solvent instead of water. Ethanol has a lower boiling point than water, and thus evaporates more quickly. While monolayers could indeed be fabricated in this way, the higher evaporation rate yielded some practical difficulties, as the solvent evaporated so quickly that the spinning solution

would start drying even before spin coating could be started. Therefore this was also abandoned in favour of water.

7.1.5 Effect of sphere concentration

As established above, a high spinning speed gave more uniform films on the macro scale. But higher speeds also tend to yield incomplete monolayers with large voids. To counteract this, a simple measure is to increase the solids fraction of the spinning solution, while keeping all other parameters untouched. This requires the use of an ultracentrifuge. After some testing, it was found that complete wafer coverage could be achieved using aqueous suspensions with solids fractions around 30%. This allowed the spin coater rotational speed to be greater than 4000 RPM, which also made the samples homogeneous on the macro scale.

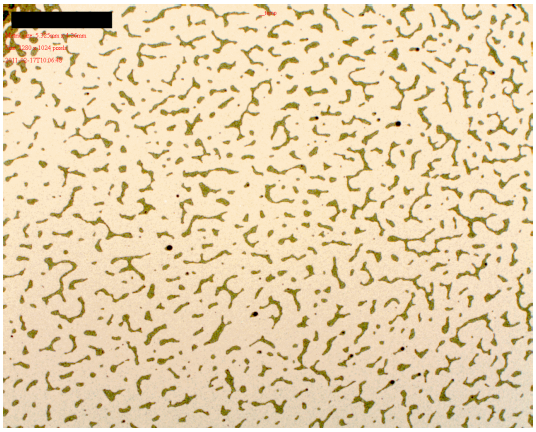

(a) *Overview image, scale bar 1000 µm*

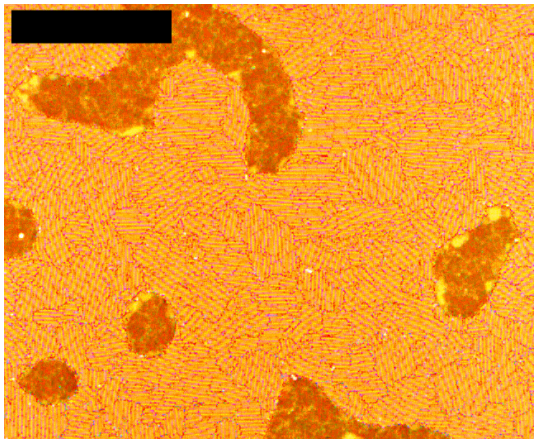

(b) *Optical image showing typical domain sizes. Straight lines within each domain represent a line of spheres. Average domain size approximately 1000 µm^2. Scale bar 100 µm*

Figure 7.4: *Monolayer film obtained by spin coating a solution of 30% spheres, 70% water. Darker areas are double layers. Sample 47, sphere diameter 1 µm*

7.1.6 Summary and evaluation

After careful experimentation with all the above variables, the best results were obtained using a 30:70 mixture by volume of solids and water. For each batch of fabricated samples, approximately 2 ml of stock 10% sphere solution from the manufacturer was centrifuged and supernatant solvent removed, leaving approximately 0.6 ml of solution of the desired concentration. The precise concentration of the suspension was tweaked

on a few test samples by carefully diluting the solution until a near-perfect monolayer coverage was achieved. Each batch was sufficient for preparing approximately 15 samples, sized 15x15 mm.

Creating a perfect monolayer with no voids or double layer islands was nearly impossible; some double layers or voids were unavoidable. It was decided that partial double layers were preferred to monolayers with voids. This was because the subsequent processing steps will generally apply to all exposed wafer areas, meaning that any void areas would be affected. Areas covered by double layers of spheres, however, should be virtually untouched by the following processing steps. After bead removal, the optical properties of the finished sample would then be a superposition of the behaviour of a bare wafer and of the synthesised structure, weighted by area fractions. Thus, the finished samples typically contained one complete monolayer plus approximately 10–15% of a second layer on top.

Typical domain sizes obtained in this method was were around 1000 μm^2, as can be seen in Figure 7.4b. This image also shows double layer regions.

Monolayer samples also exhibited six-armed reflection patterns under white light. An example is shown in Figure 7.5. As was explained in Section 3.3, these patterns indicate that the orientation of domains remains relatively unchanged in the radial direction while tangentially it is more random. A model displaying this was shown in Figure 3.8b.

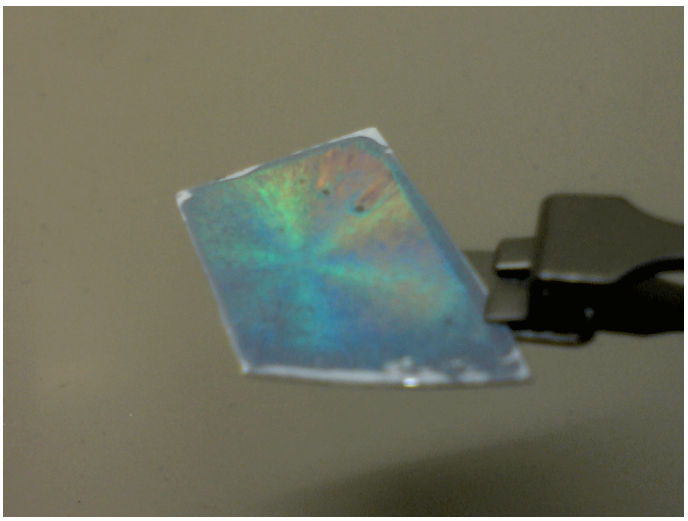

Figure 7.5: *Monolayer sample displaying a six-armed reflection pattern under white light*

Thus we conclude that monolayers of good crystalline quality, displaying long range order in the radial direction, could be successfully fabricated by spin coating aqueous suspensions of beads.

7.2 Metal islands for plasmonics

Metal nano-islands were fabricated by nanosphere lithography on a monolayer colloidal crystal of polystyrene beads, the diameters of which were 490 and 1000 nm. A summary of the samples investigated in this section is given in Table 7.2.

	PL4	PL2	PL10	PL8	PL19	PL17	PL20	PL18
Island height b [nm]	10	30	50	70	20	30	40	60
Bead diameter [nm]	1000	1000	1000	1000	490	490	490	490

Table 7.2: *Synthesis parameters of the plasmon samples referred to in the text*

7.2.1 Structural characterisation

SEM images revealed that silver deposition and sphere liftoff were indeed successful. The silver deposited between the spheres remained on the substrate after sphere liftoff, as expected. However it was observed that for very thin (10 nm) metal films, the island quality was very poor. Rather than forming continuous islands of uniform thickness, small independent crystallites were seen. For thicker silver films, this was no longer an issue and the island morphology became far more uniform, as seen in Figure 7.6.

The height profiles of deposited islands were also investigated by AFM. This revealed that the height of an island did not vary much from its center to the edges, indicating good uniform coverage. This is partially attributed to the fact that in the thermal evaporator used to deposit silver, the sample stage was rotating to avoid shadowing or other directional non-uniformities. An example of an AFM scan with a height profile is shown in Figure 7.7.

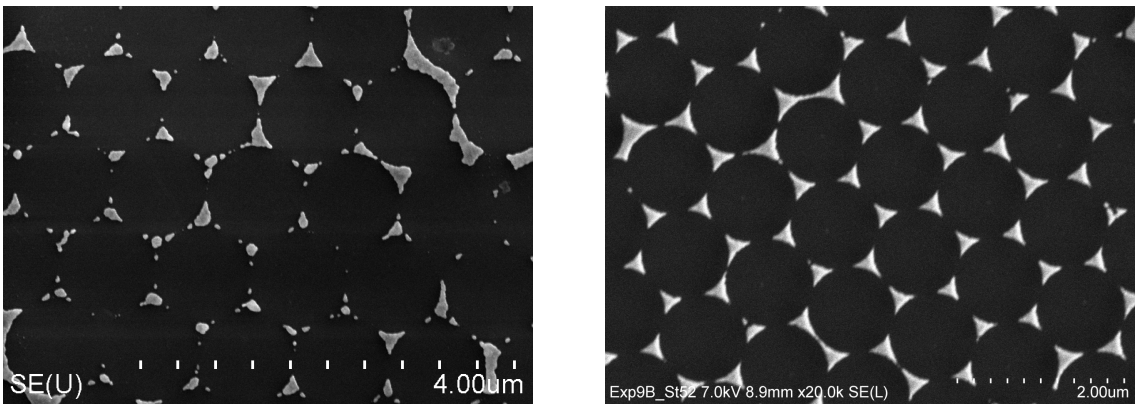

(a) *Sample PL4 (10 nm Ag)* **(b)** *Sample PL8 (70 nm Ag deposited)*

Figure 7.6: *Island quality for different thicknesses of deposited Ag*

In Section 2.3.2 it was mentioned that if the metal particles cover roughly 10% of the substrate, nearly all incident light near the surface plasmon resonance frequency should be scattered effectively [25]. Therefore this is an important target area fraction to aim for. By a simple geometrical calculation for ideal nanosphere lithography deposition, the silver islands should cover 9.3% of the wafer area. SEM images analysed by ImageJ revealed that our samples are indeed close to this value; the area fraction in Figure 7.6b is, for instance, 7.9%.

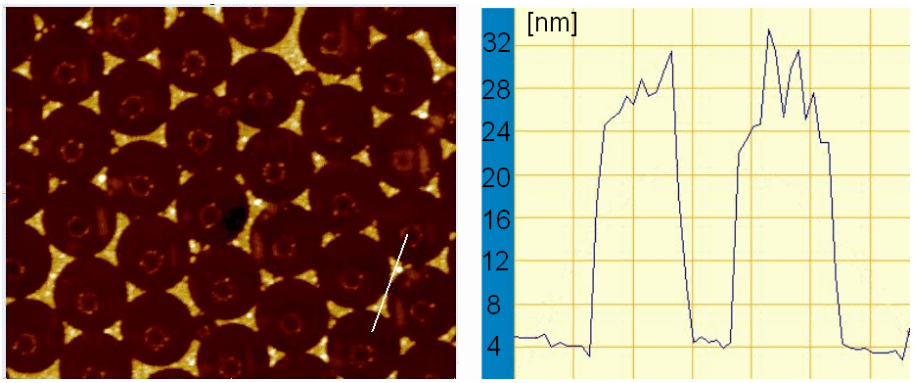

Figure 7.7: *AFM scan of Sample PL2, including height profile of two adjacent islands. Deposited Ag thickness 30 nm, measured island height approx. 30 nm*

Due to local defects in the monolayer colloidal crystal, imperfections in the metal island coverage are unfortunately inevitable. Such defects include co-joined metal islands, particularly at grain boundaries in the colloidal crystal, as seen in Figure 7.8a. By numbers, the near-perfect triangular islands dominate, but by area fractions defects are also significant. The optical contributions of the large complex metal structures remain unknown. Large metal particles with rounded corners are thought to act mostly as mirrors, reflecting light back from the surface rather than contributing to plasmonic absorption, while edgy connected islands might also contribute to plasmonic scattering much like their smaller counterparts. However it should be emphasised that this remains speculative, and no investigations of this could be found in the literature.

The monolayers of beads used as templates contain, by area, around 15% of double layer crystals, as explained in Section 7.1 and seen in Figure 7.4. Some silver which is deposited on top of such double layer regions will also be able to permeate through and deposit on the wafer, as seen in Figure 7.8b. This results in the formation of smaller, near circular silver islands on the surface.

In conclusion, entire samples could be covered with metallic islands whose height corresponded very well with the deposited silver thickness. Although some interconnected silver patterns and other anomalies were found, the near-perfect triangular islands dominate.

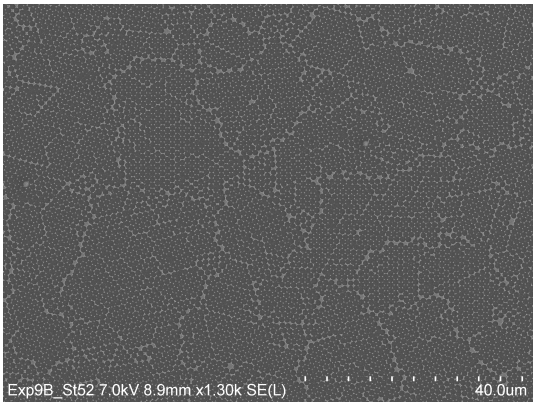

(a) *Overview image showing defects and grain boundaries*

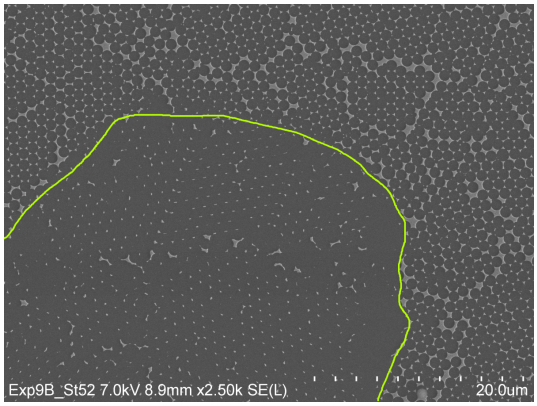

(b) *Circled area shows silver deposited on top of a double layer of beads*

Figure 7.8: *SEM images of Sample PL8, 70 nm Ag deposited on 1000 nm diameter spheres*

7.2.2 Optical properties

The structural characterisation of the metal islands is certainly encouraging for the prospect of using these islands for metal catalysed etching in a subsequent step. This avenue will indeed be explored in the following section. However, it is also interesting and worthwile to investigate the optical properties of the substrates patterned with metallic nanoparticles, as they should exhibit interesting plasmonic scattering.

As was described in Section 2.3.1, a number of factors affect the plasmon resonance frequency. An equation was derived, which is reproduced here for convenience:

$$\lambda_{max} = 1125 + (a - 240) \cdot 4 - (b - 22) \cdot 7 + 4 \cdot d_{\mathrm{SiO}_x} + 87 \cdot (RI_{subst} - 1.5) \qquad (7.1)$$

where a is the in-plane size of the islands as shown in Figure 7.9b, b is the island height, RI is the refractive index of the substrate and d_{SiO_x} is the oxide overlayer thickness (if present).

It was decided to investigate how the height and width of the islands affect the plasmon resonance frequency. The height is determined by the amount of silver deposited onto the mask, while the width is controlled by the size of the colloidal spheres used in the template. The relationship between the lateral size parameter a and the sphere diameter, as found by Jensen et al. [28], is shown in Figure 7.9a.

By knowing the island sizes, as well as the refractive index of the substrate, one can use Equation 7.1 to determine the approximate wavelength at which the plasmon resonance is expected to occur. However, for silicon substrates this equation is only a guideline, since the effect of substrate refractive index on the resonance frequency has not been explored thoroughly in literature. For the samples explored in this section, the expected resonance frequencies are calculated and presented in Table 7.3.

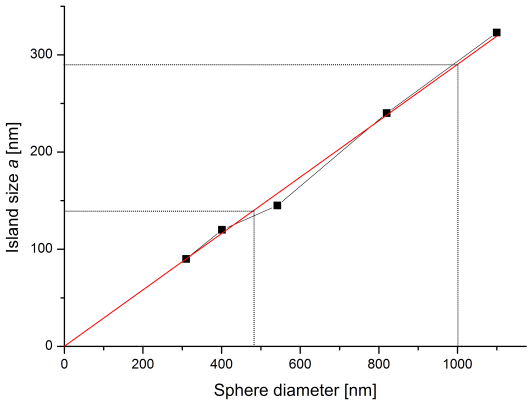

(a) *Lateral size parameter a of silver islands as a function of the diameter of spheres in the template. Original data from Jensen et al. [28]*

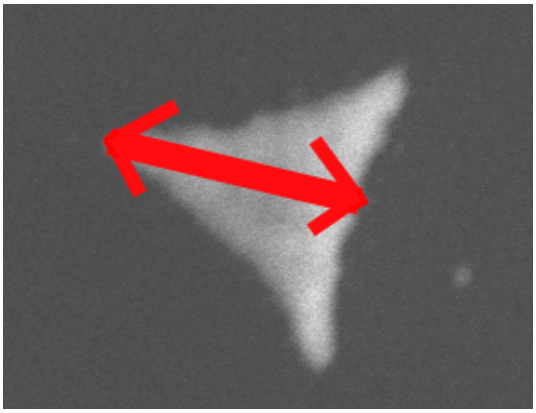

(b) *Definition of the parameter a*

Figure 7.9: *Lateral size parameter a of the islands*

	PL4	PL2	PL10	PL8	PL19	PL17	PL20	PL18
Island width a [nm]	290	290	290	290	140	140	140	140
Expected λ_{res}[nm]	1627	1487	1347	1277	957	887	817	677

Table 7.3: *Island width a, interpolated from Figure 7.9a, and expected plasmon resonance wavelengths for these geometries, found using Equation 2.18*

The reflectivity of the samples fabricated on templates of 490 nm diameter beads is shown in Figure 7.10. As a general observation, the reflectivity is higher than for a bare silicon wafer. This is likely caused by the large, interconnected silver features which which were present on all the samples due to imperfections in the monolayer mask, as was shown in Figure 7.8a. These islands may act as mirrors, giving a higher reflectivity overall.

The plasmon resonance peak of Sample PL17 is expected to occur at 887 nm, and a clear reflectivity peak is seen here at approximately 850 nm. In other words the observed peak agrees well with theory. The slight difference from the expected value may be attributed to slight island size deviations and inaccuracies in the formula, primarily related to the high refractive index of the substrate used. No resonance peaks are observed for the other samples, however. It should be noted that the monolayer used as a template in Sample PL17 was made in a different batch than the others, using a different spinning solution. Some batch-to-batch variability in the monolayer quality is to be expected, and it is possible that the monolayer quality on the other samples was not adequate for a clear peak to be observed. The plasmon resonance peak for Sample PL17 is indeed quite broad, which indicates a wide size distribution of the triangular silver islands even here. It is therefore quite conceivable that if the monolayer quality of the other samples was inferior, the plasmon peak might be quenched altogether.

No reflectivity peaks were observed for samples made using 1 µm template beads (not shown). These samples are expected to have resonance frequencies well into the infrared, as found in Table 7.3. At these wavelengths the total reflectivity of the samples is high, since the back side reflectance also contributes to the overall signal. It is possible, therefore, that the plasmon peak signal is simply too small in relation to the overall signal to be detected.

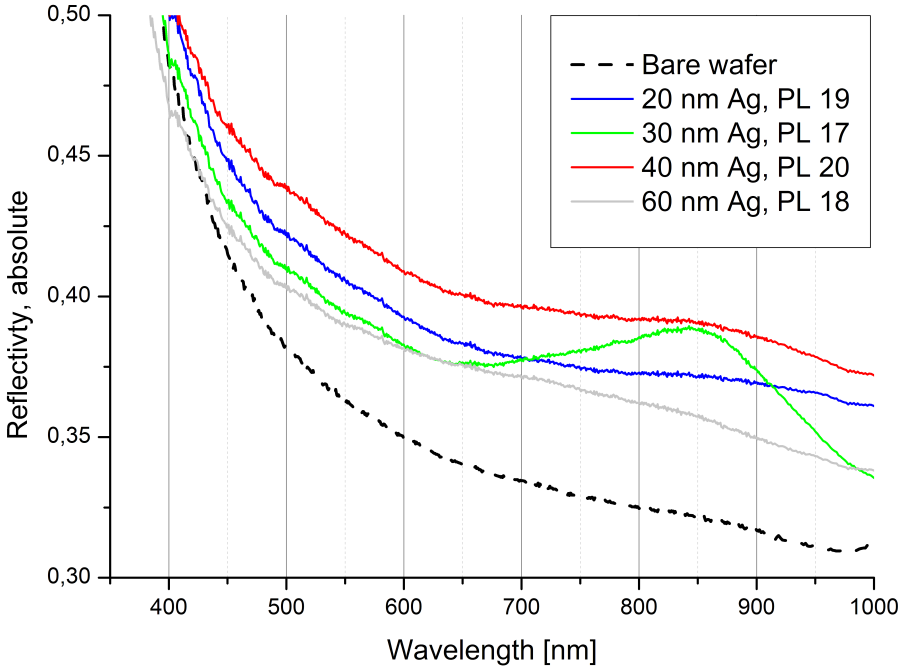

Figure 7.10: *Reflectivity of samples, 490 nm template bead diameter*

We conclude that plasmon resonance is indeed observed at 850 nm for a sample with template bead diameter 490 nm and silver thickness 30 nm. The position of the peak agrees well with theoretical predictions. The resonance peak is broad, indicating a wide size and shape distribution of the silver nano islands. No resonance peaks were observed from the other samples investigated, most likely due to an inferior quality of the monolayer templates.

There has been some debate in the scientific community as to whether the metallic islands should be deposited on the front or back side of the solar cell for maximum benefit, though lately most groups seem to focus on depositing on the back side. In this configuration, the plasmon peak should occur at a wavelength just shy of the band gap of silicon. This low-energy light has low absorption coefficients and is therefore likely to pass through the entire cell without being absorbed, where it can then interact with the metal particles and be scattered back into the silicon. The wavelength at which the plasmon peak for Sample PL17 occurs is indeed within this range of interest for very thin wafer solar cells. By making the islands a little larger, or coating them with silicon

dioxide, it should be possible to shift the resonance frequency towards 1000 nm, which would be even more suitable also for thicker wafer cells.

7.3 Diffraction gratings I. Seed formation

In Section 4.2, various methods for creating diffraction gratings in silicon wafers were introduced. Electrochemical etching was discussed in some detail. It was shown that if a wafer can be pre-patterned by some method to create sharp pits, the electrochemical etching will preferentially initiate at these sites, which thus function as "seeds" for the etch. By properly managing the parameters of the electrochemical etching process, highly tuneable structures can thus be formed, such as cylindrical holes or hemispherical dimples. These geometries are expected to be very good diffraction gratings, suitable for application as back reflectors in solar cells.

Performing the electrochemical etching step is beyond the scope of this work. Rather, it was decided to investigate different techniques for the patterning of silicon wafers to create seeds which may later be used for electrochemical etching or, possibly, other types of chemical etching. Four different patterning techniques were attempted, all relying on monolayers of beads. The results obtained for each of these methods will now be compared.

7.3.1 Metal catalysed etching

One of the techniques investigated was metal catalysed etching. First, the process for the formation of dimples in a wafer will be discussed, before investigating the etch mechanism in some more detail.

Metal catalysed etching for wafer patterning

As explained in Section 4.2.2, silver catalyses the etching of silicon by a mixture of H_2O_2 and HF, forming pits directly beneath the silver islands.

The idea explored here was to create triangular islands of silver on a wafer by nanosphere lithography, as has been shown previously, and then explose these samples to the etching solution. According to theory, the etching of silicon should be focused at the contact points between silver and silicon, causing the silver islands to "dig" into the wafer.

A monolayer of 1000 nm polystyrene beads was covered with 70 nm silver before bead removal, leaving behind triangular silver islands. The sample was then submerged in the etching solution for 60 seconds. Figure 7.11 shows a top-down image of pits etched in a sample. Dark spots are formed where the silver islands used to be, representing depressions in the wafer. The cross-sectional SEM image in Figure 7.11b demonstrates

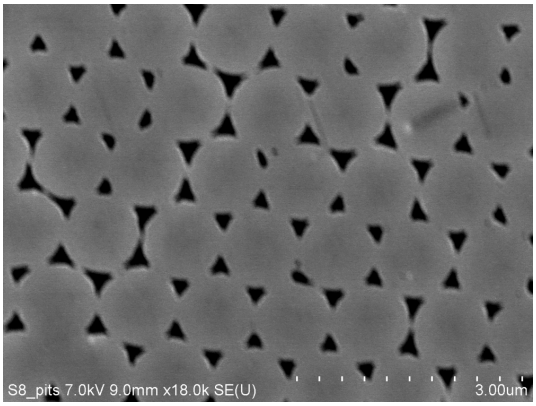

(a) *Pits seen from above. Dark spots are pits*

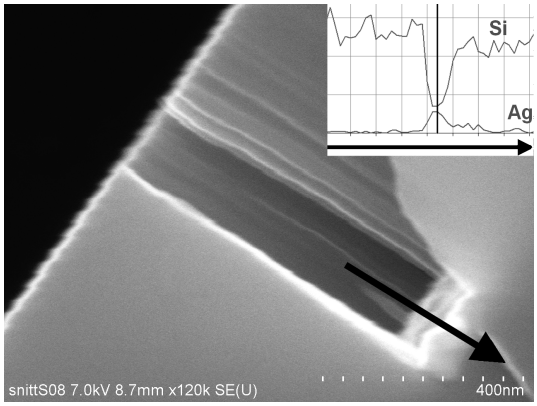

(b) *Pit seen from the side. The inset shows an EDS line scan (elemental analysis) along the orange arrow. At the bottom of the pit the silver concentration is high*

Figure 7.11: *SEM images of silver catalysed etch pits. Etch duration 1 minute*

that the sidewall profile is indeed very straight, with no appreciable widening or tightening of the groove. This is in line with the results by Huang et al., as shown in Figure 4.6. SEM EDS scans of the grooves show a high silver content at the bottom of the pits, indicating that the silver particles have indeed carved into the grooves during the etching process, as predicted.

We thus conclude that metal catalysed etching can indeed be used for the formation of holes in a wafer. For short etch durations, the etch was found to be highly directional, giving straight pore walls.

Further analysis of the etch mechanism

For the purpose of understanding more about the etch process, another identical sample was left in the etching solution overnight for a total etch duration of 19 hours. The final structure is shown in Figure 7.12. These images show that the etched holes have become significantly wider than they were intially. This highlights the fact that the etching rate is indeed not zero in the absence of silver; there is a finite and non-zero etching rate of all exposed silicon, regardless of whether any silver is present. This has caused the pores to widen during the etch, finally leaving only pillars of silicon standing. The final structure is far too inhomogeneous to be of practical use for any perceiveable application, except perhaps as an antireflective coating, as the samples appeared quite dark. However it must be stressed that this particular sample was exposed to an extremely long etch. By reducing the adjusting the etch duration and tuning parameters such as etchant concentration, temperature and additives, much more uniform pores could conceivably be formed.

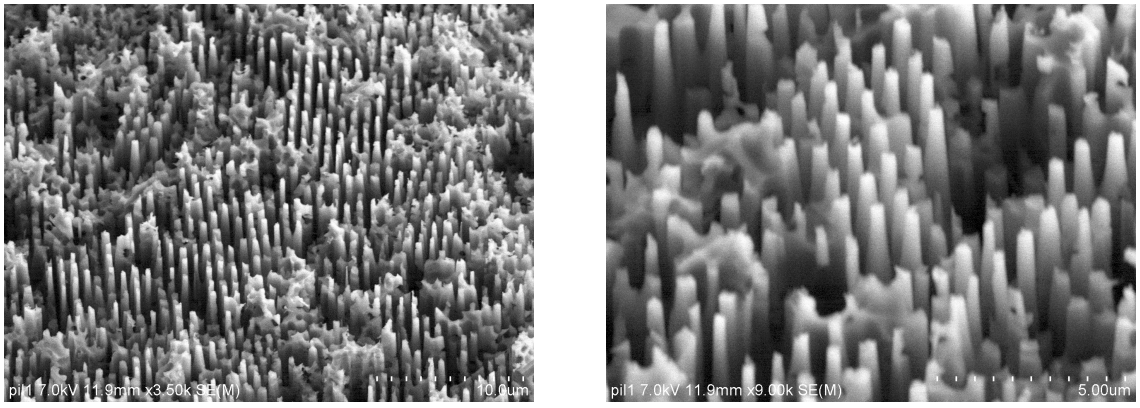

(a) *Overview image* **(b)** *Close-up of pillars*

Figure 7.12: *SEM images of silver catalysed etch pits. Etch duration 19 hours (1140 minutes)*

7.3.2 Laser ablation using colloidal microlenses

Microlenses on bare silicon wafers

Laser ablation using colloidal microlenses was attempted as a method for creating pits in a wafer. Figure 7.13 shows two AFM scans of laser ablated spots. The Gaussian beam intensity profile of the laser beam causes the intensity to drop off radially from the center of the beam, giving smaller and smaller features towards the edges of the spot before eventually the laser intensity drops below the ablation threshold.

Sample	VIS-Q1	VIS-Q2	VIS-Q3	VIS-Q4
Pulse energy [nJ]	90	150	290	380
Avg. energy density [mJ/cm^2]	6	10	18	24

Table 7.4: *Samples for laser ablation. Energy density is the averaged of the entire spot, calculated by assuming a spot diameter of 30 µm. The laser power for the UV samples could not be detected, but was increased in the same manner from UV-Q1 to UV-Q4*

If these structures are to be used as initiation points for an electrochemical etch, it is the depressions in the wafer which are of primary concern. Figures 7.15 and 7.14 show side views of AFM scans on some spots such as those shown in Figure 7.13. Note that while the vertical dimension is the same in all figures (scaled in nanometers), the unit in the horizontal direction is arbitrary due to differing sizes of the scan areas.

Consider first the UV irradiated samples, shown in Figure 7.15. Here, the depth of the pits formed actually remains relatively steady around 50 nm as the pulse energy is increased. The height of the features on top of the surface, however, follow a different trend. These peaks first get higher with increasing energy before finally dropping off

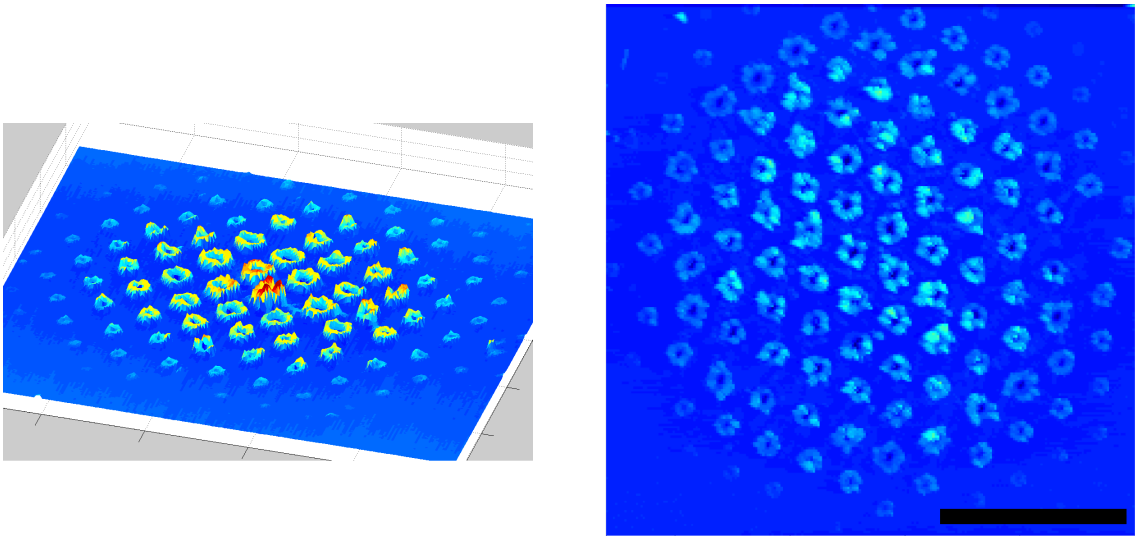

(a) *Tilted view AFM, UV-Q1, arbitrary colour scale*

(b) *Top view, sample UV-Q4. Scale bar 4 μm*

Figure 7.13: *AFM images showing typical irradiated spots*

again for the highest energy. Recall that the samples were cleaned by ultrasonicating in acetone, which dissolves polystyrene, prior to AFM imaging. However it is possible that some polystyrene is still left on the samples, and that this accounts for some of the crests seen. The crests could also consist of re-deposited silicon. The nature of these features was not investigated further as, for the application considered here, it is the pit depth which is important.

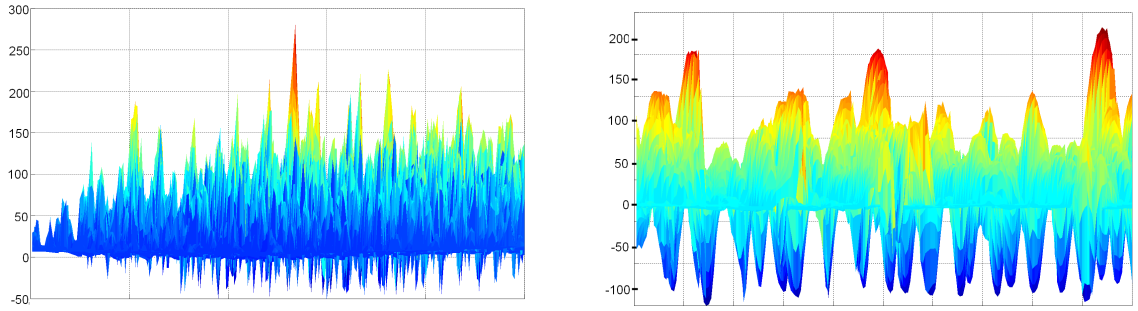

(a) *VIS-Q2*

(b) *VIS-Q4*

Figure 7.14: *AFM scans, side view, visible light irradiated samples. Vertical unit is nanometers*

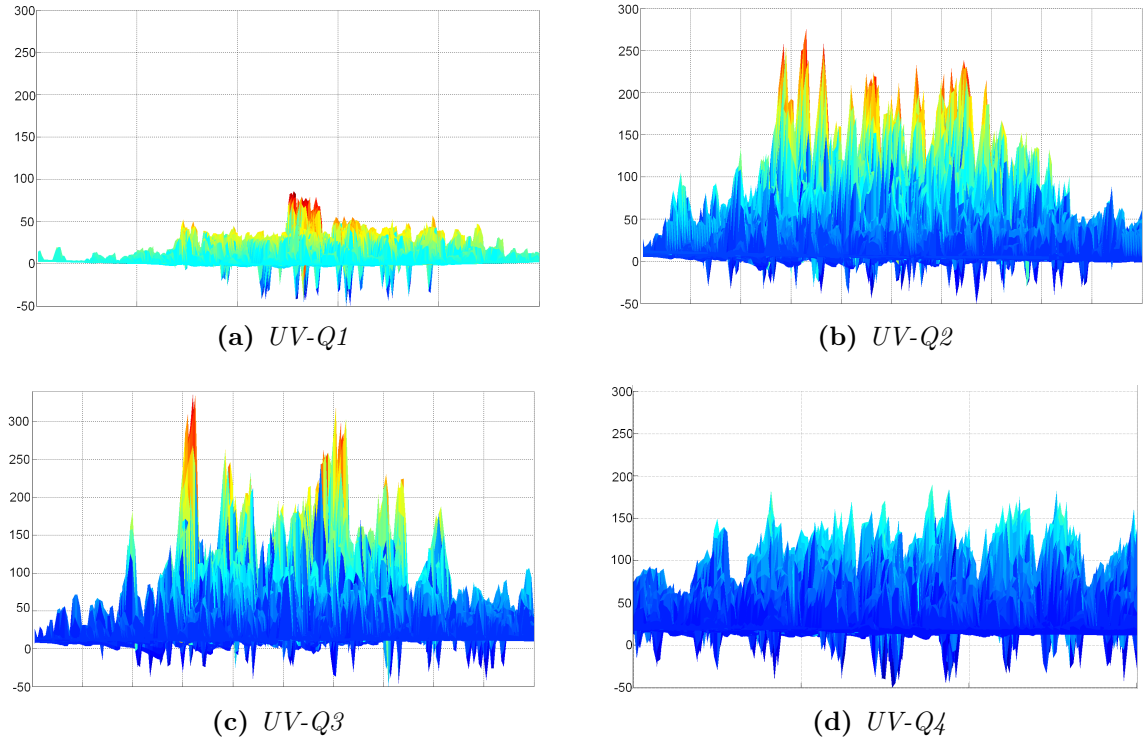

(a) *UV-Q1* **(b)** *UV-Q2*

(c) *UV-Q3* **(d)** *UV-Q4*

Figure 7.15: *AFM scans, side view, UV samples. Vertical unit is nanometers. Observe how the feature depth increases with laser beam energy*

While the pit depth of the UV irradiated samples is actually remarkably deep compared to literature results, the visible light samples are even more impressive in that regard. Figure 7.14 shows that pits with depths exceeding 100 nm could be formed when using the highest laser energy. This is more than 15 times as deep as the results obtained by Brodoceanu et al. [78].

In summary, laser ablation proved to be effective for producing hexagonal arrays of pits in a wafer. Both visible and ultraviolet light was used with success, although the deepest pits were produced using visible light. The pit depth exceeds 100 nm for a beam energy 380 nJ and a wavelength of 515 nm.

Microlenses on silicon nitride coated wafers

Attempts were also made at using colloidal crystal monolayers as microlenses for burning holes in a 80 nm silicon nitride film. Figure 7.16 shows two optical microscopy images of irradiated spots with two different laser pulse energies. At the lowest energy, the nitride is still intact, indicating that the ablated dimples are not deep enough to fully penetrate the entire nitride film. When the energy is increased, however, bare silicon wafer is exposed at the center of each beam. This is where the laser energy was

the greatest, so this is where the dimples are naturally expected to be deepest. A holey nitride grid is seen to be left on the surface in between the dimples.

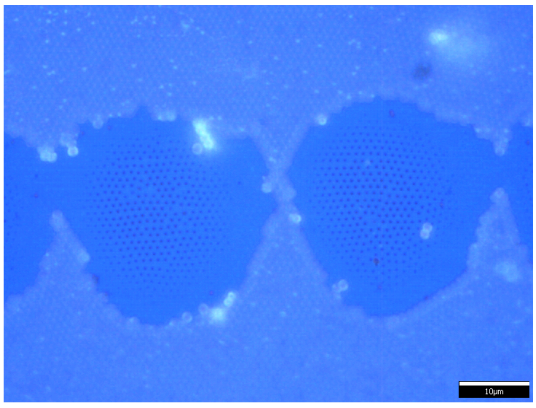

(a) *Pulse energy 380 nJ*

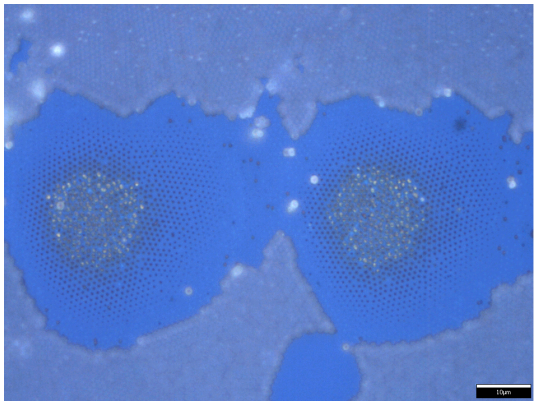

(b) *Pulse energy approximately 900 nJ. Grey areas at the center of each spot represent exposed silicon*

Figure 7.16: *Laser irradiated samples. Blue is silicon nitride, grey is exposed silicon*

To conclude, laser ablation using sphere monolayers as microlenses was successfull in burning holes in a 80 nm silicon nitride film, producing a holey mask of silicon nitride on top of an exposed layer of silicon. It is believed that this type of structure will be suitable as a mask for the etching of silicon through the holes in the grid.

7.3.3 Selective alkali etching through silver etch masks

Alkali etching, specifically KOH etching, is very interesting for the patterning of monocrystalline wafers because of the highly anisotropic nature of the etch. This can be used to create inverse pyramids which have been demonstrated to function very well as initiation seeds for an electrochemical etch [72, 73]. Since silver is not etched by KOH, it was decided to investigate the use of silver islands as etch masks for a KOH etch. The idea was to force the formation of etch pyramids whose size would be limited by the silver islands, as shown schematically in Figure 7.17.

Rather than using silver islands fabricated by nanosphere lithography, initial testing was done using randomised silver patterns on a wafer. These structures were formed simply by thermal evaporation of 15 nm silver onto a plain wafer, and then heat treating the wafer at 200°C for 15 minutes. Due to the high contact angle between silver and silicon this heat treatment causes the silver film to "curl up" and form thicker structures such as droplets or islands. The samples used here consisted of continuous networks

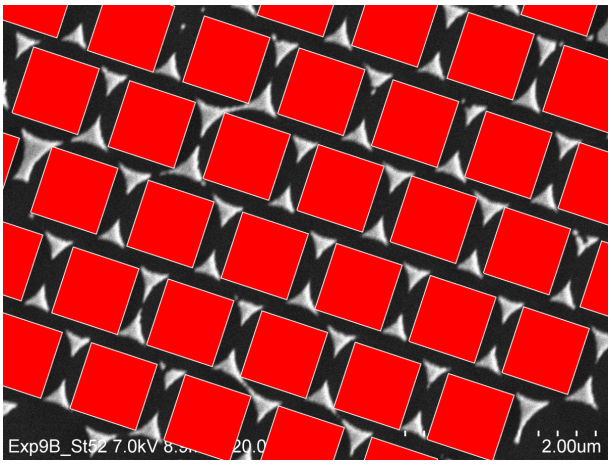

Figure 7.17: *Schematic of the idea. Red squares represent the size of the KOH etch pyramids to be formed in-between the silver islands*

of silver "snakes" with a sub-micron pitch, as shown in Figure 7.18a. The idea was to use these structures as an etch mask, hopefully forcing the KOH etch to occur only between the silver structures.

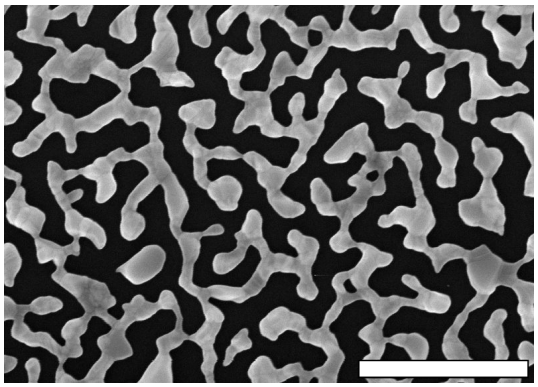

(a) *Before KOH treatment. The bright pattern is silver*

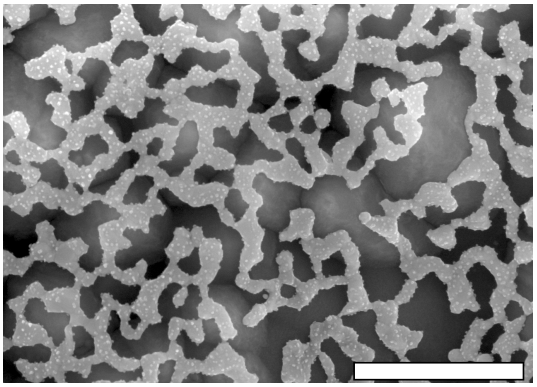

(b) *After KOH treatment. The silver pattern is suspended above several big holes dug out by the KOH etch*

Figure 7.18: *Silicon wafer covered by metallic random pattern produced by first evaporating a silver thin film onto the wafer and then heat treating. Scale bar 1 µm*

However, this proved to be unsuccessful. Rather than only etching between the silver structures, the KOH etch was able to dig under the silver, effectively tearing the silver off the surface, forming the characteristic pyramids. This is seen in Figure 7.18b. It is believed that the very low mechanical strength of silver at these thicknesses played an important role. The high contact angle between silver and silicon caused the contact patch between silver and silicon to be very small, resulting in poor adhesion. The silicon etching induces bubble formation, which likely put high mechanical stresses on

the fragile silver masks, causing them to rupture and fail quickly.

Based on these findings, this work was discontinued, and other methods were used instead.

7.3.4 Selective alkali etching through silicon nitride etch masks

It was decided to substitute the silver etch masks for a far more mechanically sturdy silicon nitride etch mask for KOH etching. The results are presented here.

Step 1. Silicon nitride etch mask deposition by PECVD In the first step, monolayers of 800 nm diameter silica beads were coated by silicon nitride in PECVD. The beads then had to be removed to expose the silicon wafer at the contact points between the beads and the substrate.

Improving nanosphere liftoff A problem in initial testing was that if using a standard industry recipe for nitride deposition (400°C, 40 W AC power), the film covered the beads more or less uniformly due to the isotropic nature of the deposition. As the mechanical strength of silicon nitride is very high, this effectively "glued" the spheres to the substrate, making them impossible to remove by sonication. This was the case for all the tested film thicknesses, the thinnest of which was 50 nm. To combat this problem it was decided to use a higher AC power (100 W) in the PECVD deposition to help make the deposition more directional (top-down). The expected influence of the higher power is shown schematically in Figure 7.19.

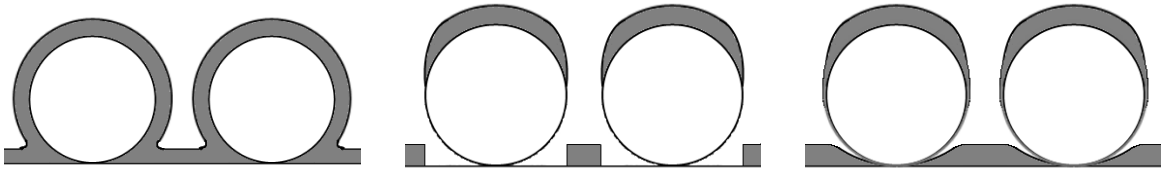

(a) *Totally isotropic deposition* **(b)** *Totally anisotropic deposition (ideal model)* **(c)** *Realistic model*

Figure 7.19: *Morphology of PECVD deposited silicon nitride on colloidal sphere monolayer*

With those measures taken, nanosphere liftoff after deposition was partially successful for all investigated thicknesses, the thickest of which was 159 nm. The growth rate at of the film was determined by ellipsometry measurements on planar wafers to be 35 nm/min. For the thickest nitride, sphere removal was unsuccessful in some areas of the samples.

To further improve nanosphere liftoff, some nitride films were deposited at a lower deposition temperature of 200°C. The idea was that a lower temperature should prevent

the species from diffusing around on the surface of the substrate, but rather sticking at the point of impact. This should improve directionality of the deposition process. The low-temperature nitrides were not used in further processing because the etch rate in hydrofluoric acid was found to be impractically high, giving very poor control of the next processing step. This observation can be explained in terms of the film morphology. At the low deposition temperature, the growth rate of the nitride was 55 nm/min compared to 35 nm/min at 400°C. Assuming that sticking probability of the reactive species landing on the substrate is independent of temperature, this means that a lower temperature yields more porous films. This theory was also corroborated by refractive index measurements in ellipsometry. The high temperature nitrides had a refractive index of 1.98 while the low temperature ones were 1.86, giving a change of $6.0 \cdot 10^{-4}\mathrm{K}^{-1}$. This tendency agrees well with results by Helland [92], who found a change in refractive index of $5.93 \cdot 10^{-4}\mathrm{K}^{-1}$.

If an effective medium approximation can be made, the refractive index of the film is calculated by volume fractions of voids and material; the more voids (lower density) the lower the refractive index. Thus, it is concluded that the reason for the poor quality of silicon nitrides deposited at low temperatures can be attributed to their high porosity, leaving them unsuitable for the further processing steps.

Thus, using a lower deposition temperature was not successful in improving the nanosphere liftoff process. Instead, it was decided to keep depositing at 400°C and 100 W and rather dip the samples in a 1% dilute HF solution to weaken the silicon nitride. It was found that dipping the substrates in the solution for just a few seconds was enough for nanosphere liftoff by sonication to be successful, and no colloidal beads could be detected on the substrates by optical microscopy and SEM.

Mask morphology Based on the observation that beads appeared to be sticking quite well to the substrates after nitride deposition, it was believed that the deposition of silicon nitride occurred in a rather non-directional fashion. The proposed model is shown in Figure 7.19c. To investigate this further, the masks were investigated in SEM and AFM.

These investigations revealed that there was indeed nitride in the "shadow regions" beneath the spheres, as illustrated in Figure 7.19c and shown in Figure 7.20. AFM scans, such as that shown in Figure 7.20b, confirm the gradual thickness decrease of the nitride in the shadow region to form a concave shape. Also, these height profiles revealed that unlike for silver deposition, such as shown in Figure 7.7, the thickness of nitride deposited in-between spheres did not even come close to the total deposited nitride thickness. In this particular example, height variations were approximately 5 nm while the deposited nitride thickness was 159 nm. This could be caused by the gas flow in-between beads being so restricted that the deposition happened very slowly here. Another explanation is that a thicker layer of nitride was indeed deposited here as well, but that most of it was removed during sphere liftoff in sonication, along with

the beads. Silicon nitride is a brittle and hard material which is likely to fracture abruptly. This is in sharp contrast to silver films, which are soft and ductile at such low thicknesses.

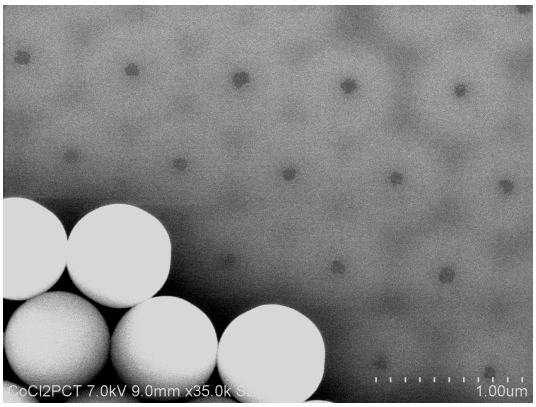

(a) *Intact spheres (lower left) and deposited nitride pattern after sphere liftoff. Note that nanosphere liftoff on this sample was performed without first weakening the nitride by a rapid HF dip, which explains the presence of intact beads*

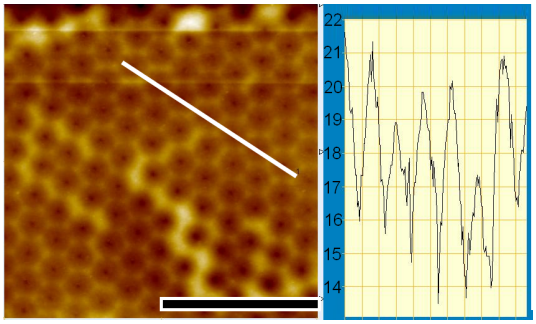

(b) *AFM profile of the same structure, along white line. Scale bar 4 µm, peak-to-bottom height variation approximately 5 nm*

Figure 7.20: *SEM and AFM scans showing sample after nitride deposition and sphere removal by sonication*

In summary, after thorough investigation of the PECVD deposition parameters, silicon nitride etch masks have been fabricated on silicon wafers using monolayers of 800 nm diameter silica beads as templates. The etch masks display 100 nm holes at the contact point between wafer and silica bead. In these holes the silicon wafer is exposed.

Step 2. HF etching to enlarge holes in nitride etch mask. While these 100 nm holes are a nice proof-of-concept demonstration for the formation of a nitride etch mask by nanosphere lithography, it would be useful to tailor the mask even further to enlarge the holes. This would allow for larger etch pits to be formed, adding another level of customisabilty of the optical properties of the final structure. Therefore it was decided to do a quick HF-dip after the nitride deposition to increase the size of the holes in the nitride before the KOH etch. As was explained in Step 1 above, this treatment also has the additional benefit of weakening the nitride slightly, so that the template beads can be more easily removed.

The etching rate in 1% HF of the nitride film deposited at 400°C was determined by ellipsometry to be 4.3 nm/min. 7 samples were prepared, with varying etch durations as listed in Table 7.5.

Sample	PE1	PE2	PE3	PE4	PE-A	PE-E	PE-C	PE-B
HF concentration [%]	1	1	1	0	1	0.67	0.67	0.67
Etch duration [s]	20	40	60	0	5	2	5	10
Nitride etched [nm] *	1.4	2.8	4.3	0	0.3	0.1	0.3	0.5

Table 7.5: *Some samples received an HF-etch after PECVD nitride deposition, to enlarge the holes in the nitride at the contact point between wafer and bead. After KOH etching, pyramidic grooves were formed into the silicon, the size of which depends on the size of the holes in the nitride etch mask. * = calculated based on the etch rate measurements of a planar nitride deposited at these conditions*

Step 3. Potassium hydroxide etching. With the nitride etch mask finished, the next step is to do a potassium hydroxide (KOH) etch to selectively etch the silicon through the holes in the nitride film. This is a highly anisotropic etch which only attacks the exposed silicon while leaving the nitride mask intact, as explained in Section 4.2.2. When etching on a planar wafer, inverse pyramids are formed with clearly defined sidewall angles. Ideally, therefore, the dimensions of the pyramids would be determined by the size of the holes in the nitride mask, and not so much by the duration of the KOH etch.

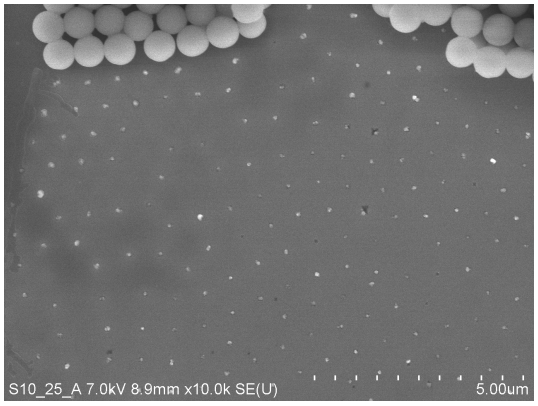

(a) *Before nitride stripping. Bright dots show holes in the nitride mask where KOH etching has occurred. Nanosphere liftoff on this sample was performed without first weakening the nitride by a rapid HF dip, which explains the presence of intact beads*

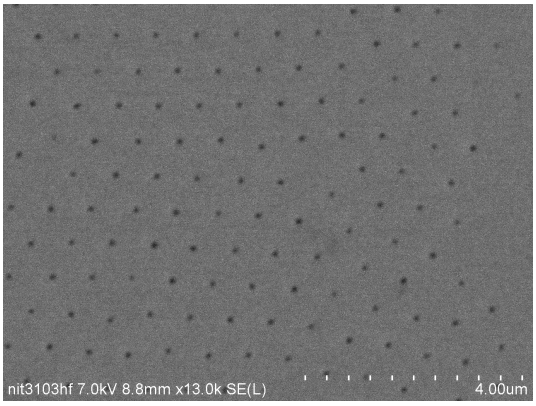

(b) *After nitride stripping. Dark spots are inverse pyramids etched out by the KOH*

Figure 7.21: *Sample PE4 before and after the final nitride etch mask removal*

First, consider the inverse pyramids formed by using as-deposited nitride masks, with 100 nm diameter holes. Figure 7.21 shows SEM images of Sample PE4 before and after nitride stripping. Figure 7.21a reveals that the nitride (dark in this image) is intact

after the KOH etching; the only etching has occurred in the holes beneath where the silica beads used to be. Figure 7.21b shows how the etching has indeed been confined to only the small exposed areas, and there is no perceivable undercut at all; the dimensions of the inverse pyramids equal the hole diameter of of the nitride mask. Note that this sample was etched rather substantially; 60 seconds in 47% KOH at 80 degrees, giving a theoretical etching depth of approximately 700 nm on a planar wafer. Due to the high selectivity of the KOH etch on different crystallographic planes, etching appeared to have stopped due to the self-limiting mechanism caused by the directionally dependent etch rate in crystalline silicon.

Now look at the samples which were exposed to a HF dip to enlarge the holes in the etch mask before KOH etching, listed in Table 7.5. Two example images are shown in Figure 7.22. Here, the inverse pyramids are seen to be far larger than the 100 nm diameter pits fabricated without such an HF dip, as was shown above. This verifies that the etch mask can indeed be tailored to produce inverse pyramidal pits of the desired size.

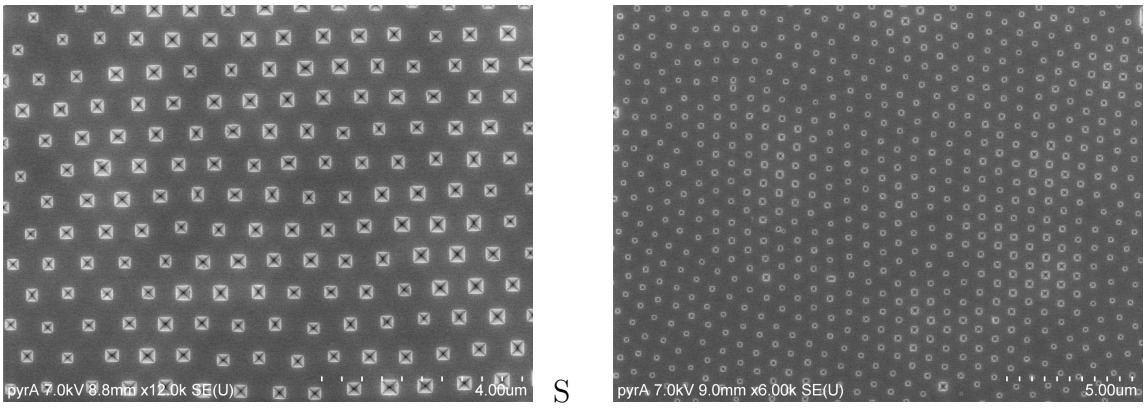

(a) *Sample PE-E* **(b)** *Sample PE-A, overview image*

Figure 7.22: *SEM images of samples after KOH etching. For these samples, the holes in the nitride film were enlarged by an HF dip prior to KOH etching. Pit sizes approximately 270x270 nm*

To conclude, silicon nitride etch masks were successfully created using nanosphere lithography and PECVD, and used for the formation of inverse pyramidal pits in the wafer by selective alkali etching through the holes in the mask. This method has, to the best of our knowledge, not been demonstrated in the literature. Excellent process control has been obtained, including tuning of the size of the pits by enlarging the holes in the etch mask using short acid baths. In the end, highly ordered arrays of pits were obtained on the silicon substrates, with one pit being formed beneath each of the beads in the template. No residual beads were observed after process optimisation.

The largest samples created in this work were on quarter 5" wafers. It is also foreseen that the method can be deployed to full wafers quite readily.

7.3.5 Evaluation of methods

Four different methods were attempted for creating periodic patterns of pits or grooves in a wafer, all based on nanosphere lithography. Only one of the methods, namely alkali etching through a silver etch mask, turned out to be completely unsuccessful. This was due to the low mechanical strength of silver, causing the mask to fall apart during the etch.

The other three methods were all successful for patterning the wafers with hexagonal dips of depths exceeding 100 nm. Metal catalysed etching was used to create straight pits whose depth could be tuned by simply changing the duration of the etch. However, while the method did work, recall that the pattern of pits is not actually hexagonal, since the pits are formed in between where the colloidal spheres used to be situated rather than directly beneath each sphere. This is seen clearly in Figure 7.11a. While the optical properties of arrays of this type of ordering have not been simulated as yet, the main problem is that the distance between the pits is very short in some directions, which puts severe restrictions on the size of the final structures which can be created when using these samples as seeds in an electrochemical etch. Another potential problem with this method is that, unlike the other techniques explored, the pores do not have a single tip but rather a wide flat bottom with sharp corners. Since it is primarily the curvature of the pores which govern the initiation of the electrochemical etch, it is believed that the control of the exact geometry of the etched structures will be rather poor using this type of seeds. This point is illustrated in Figure 7.23.

Laser ablation using colloidal crystal monolayers as microlenses proved capable of producing hexagonal arrays of sharp pits with depths exceeding 100 nm for the best laser parameters. It is believed that these pits should work very well as initiation points for an electrochemical etch. The laser used in this work is a laboratory laser designed for small-scale experiments rather than processing speed. Using this laser it is very difficult to use this technique to pattern an entire wafer. The irradiated spots are circular with a Gaussian intensity distribution, so it would be very challenging to irradiate the entire wafer evenly. The laser is also relatively slow; for the samples used here, sized 2.5x2.5 cm, the patterning took several minutes even with 40 µm between spots.

If laser ablation using colloidal crystal microlenses in this fashion is to become industrially relevant, therefore, a different approach is necessary. One alternative would be to use diffractive beam optics to split the beam into several identical spots to more effectively cover large areas simultaneously. Looking purely at the required laser energy for ablation, a 100 W industrial laser with diffractive optics would be pattern an entire 6” wafer in a matter of seconds. Another option might be to use a de-focused laser beam and let all the focusing be done by the beads themselves. In this way larger areas could be illuminated in each pulse, speeding up the process. In general, there is a strong drive in the photovoltaic community for implementing laser processing for various purposes in the fabrication of solar cells.

While laser ablation is certainly a promising technique, there is little doubt that in-

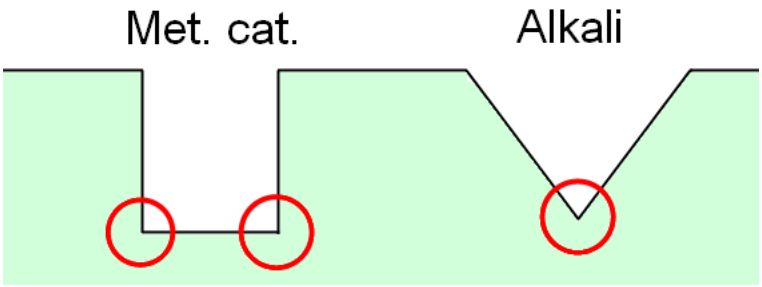

Figure 7.23: *Comparison of the seeds created by metal catalysed etch and alkali etching. The alkali etched pits have single sharp tip, which is ideal for use as seeds in an electrochemical etch*

dustrial implementation lies some distance into the future. Among the four techniques explored in this work for the patterning of wafers, there is thus one method which stands out as being particularly promising, namely alkali etching through a silicon nitride etch mask. With this method it was possible to pattern large areas with very sharp inverted pyramids in hexagonal patterns. The size of the pyramids are also tuneable. KOH etched inverted pyramids have been successfully demonstrated as seeds for electrochemical etching in the literature, using polymeric photoresists and standard photolithography to create the etch mask. A significant advantage is the sharp pits formed in this method, as shown in Figure 7.23. Our method, using nanosphere lithography, should lend itself very well to large scale implementation, as it is a quick and inexpensive method using standard equipment found in crystalline solar cell factories.

We thus conclude that the formation of seeds for electrochemical etching was successful. It is beyond the scope of this thesis to actually use these templates for an electrochemical etch process, and this concludes the discussion on this topic.

7.4 Diffraction gratings II. Dielectric cylinders

Inspired by the experiences with silver catalysed etching in the preceding chapter, it was decided to explore method further to create pillars of silicon. Here it is necessary to reduce the colloidal sphere diameter by reactive ion etching before doing the etch.

	800_1	700_1	400_1	deep1	800_5
Bead diam. [nm]	800	700	400	1000	800
Etch duration [s]	60	60	60	19 h	135
	700_P	400_2	800_4	700_Y	
Bead diam. [nm]	700	400	800	700	
Etch duration [s]	135	135	30	30	

Table 7.6: *Metal catalysed etch samples*

7.4.1 Bead diameter reduction by RIE

Colloidal crystal monolayers of 1 µm polystyrene beads were fabricated on a set of silicon wafer samples. Bead diameter reduction by reactive ion etching was performed by PhD candidate Kumar L. Vanga at Michican Technological University. Very good control of the etching rate was obtained, as shown in Figure 7.24. SEM images showing the etched beads are seen in Figure 7.25. As expected, the anisotropy of the etch causes the "flattening" of the beads, as seen in Figure 7.26. The beads, particularly the 400 nm ones, appear somewhat non-uniform after the etching. This probably is probably caused by polystyrene melting and re-solidifying.

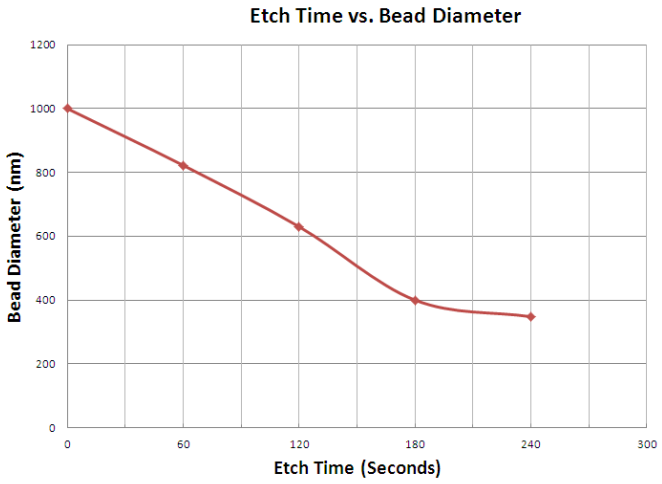

Figure 7.24: *Bead diameter vs RIE etch time*

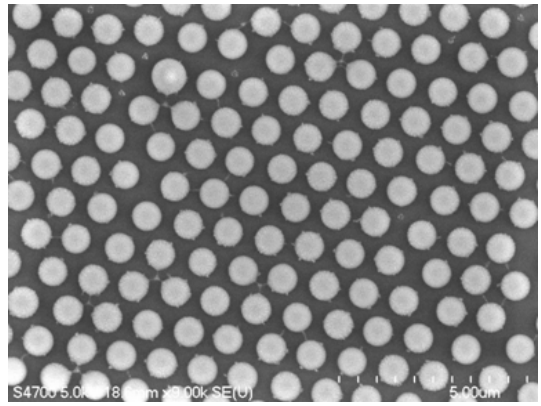

(a) *1 minute*

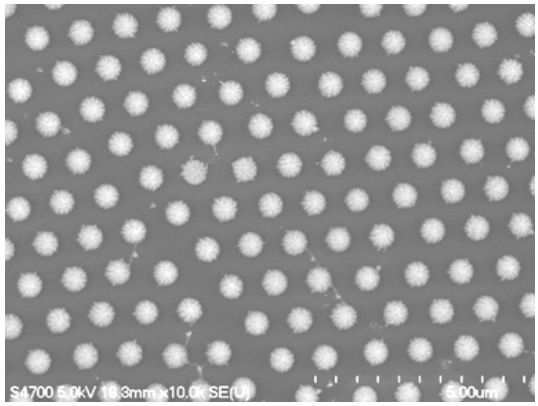

(b) *2 minutes*

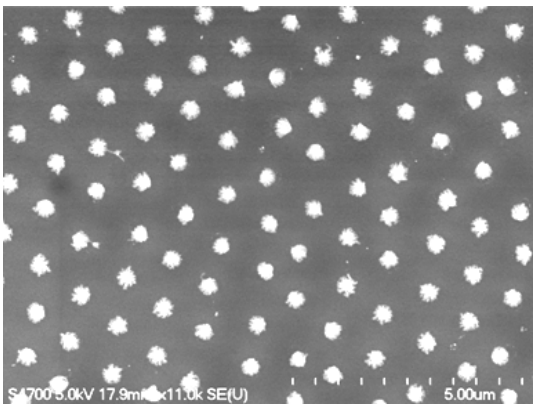

(c) *3 minutes*

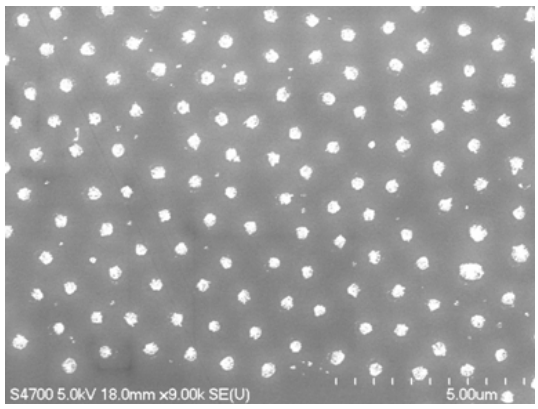

(d) *4 minutes*

Figure 7.25: *SEM images of RIE-etched beads at varying etch durations. Etch parameters 100 W/m^2, 50 sccm of O_2 and a pressure of 0.135 Torr.*

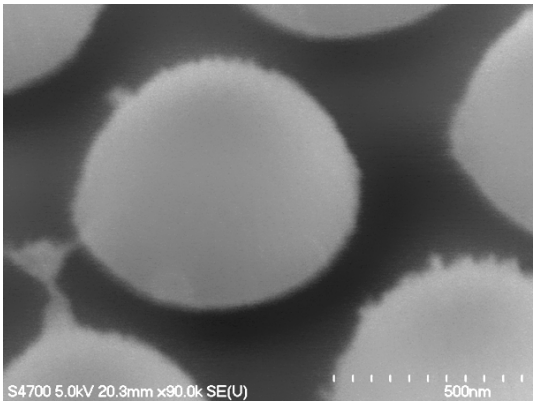

(a)

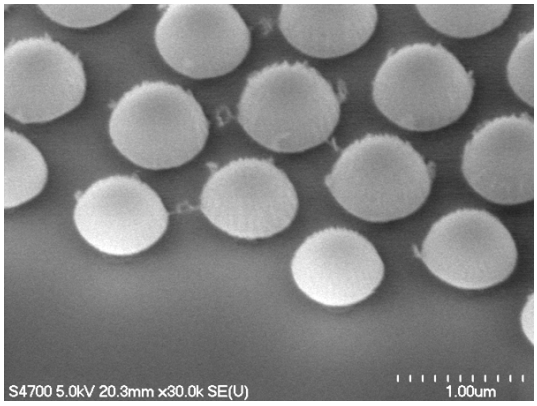

(b)

Figure 7.26: *SEM images showing how the polystyrene beads are deformed after RIE processing*

7.4.2 Silver catalysed etching

The silver catalysed etching turned out to be successful, causing the formation of separated pillars of silicon whose diameters matched very well with the bead diameters of the templates. Figure 7.27 shows how the crystalline domains of the templates are easily recognisable.

In Figure 7.8a it was shown how, when depositing silver on top of a monolayer of beads, large continuous patterns of silver were formed at the boundaries between crystalline domains of the monolayer templates. In Figure 7.27b it is seen that this silver has indeed also dug into the wafer and formed large interconnected troughs, which appear dark in the image.

The pillar sidewall profiles are found to be straight and perpendicular to the substrate. This is in agreement with the results obtained for metal catalysed etching without first reducing the bead diameters, as was reported in Section 7.3.1.

In conclusion, the formation of silicon pillars by metal catalysed etching was successful, producing hexagonal arrays of pillars whose dimensions are determined by the diameter of the beads in the template.

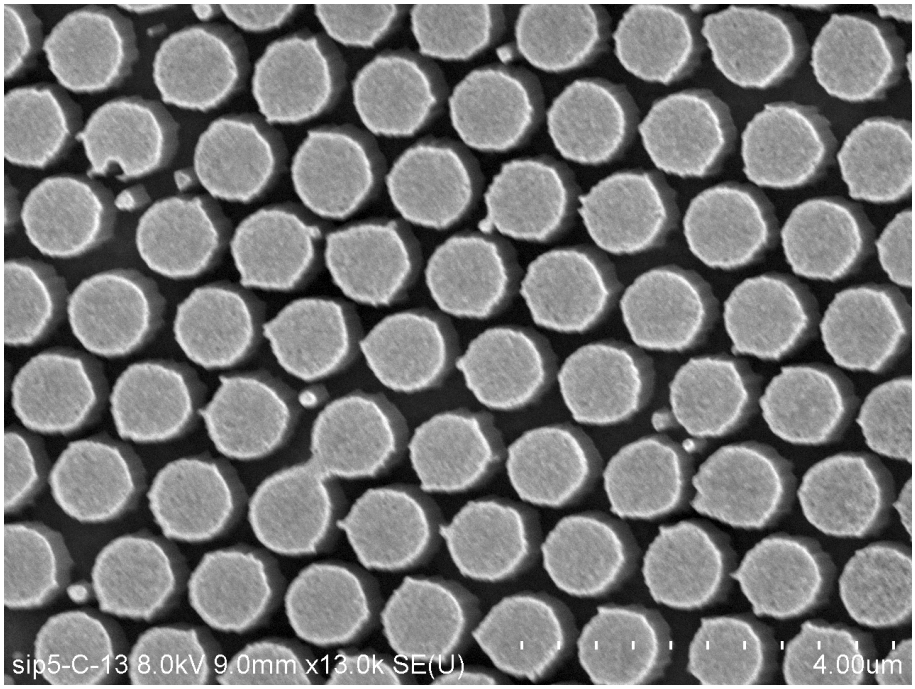

(a) *Slightly tilted view*

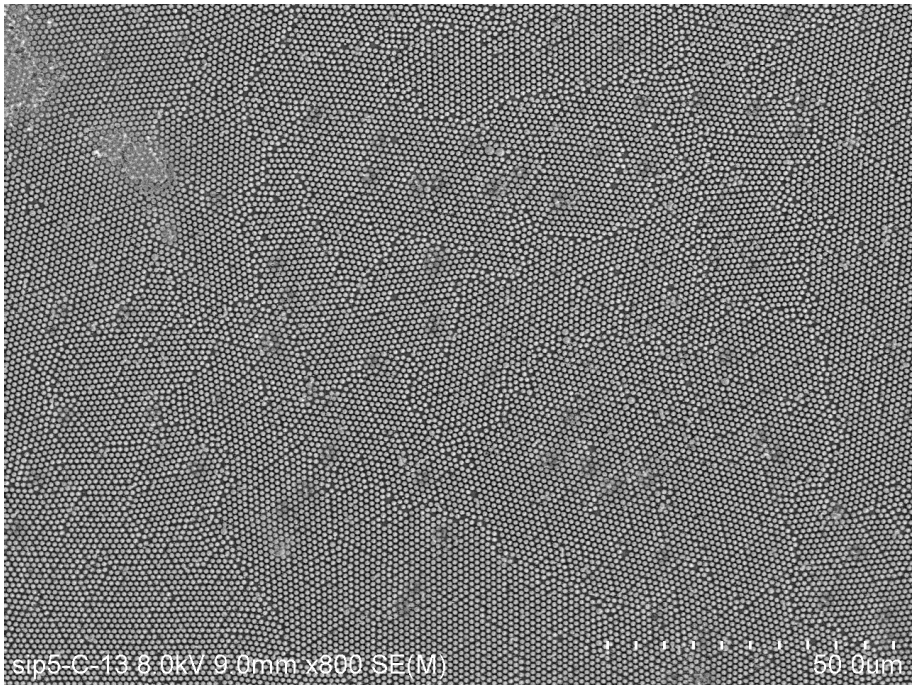

(b) *Overview image*

Figure 7.27: *SEM images of pillars, sample 800_4*

7.4.3 Process evaluation

While it must be emphasised that most of the sample areas were in fact covered with pillars such as shown above, there were also areas on all the samples which displayed certain anomalies. The etched depth was observed to vary slightly across a sample, on the microscale. This was most clearly visible on samples with small bead diameters (400 nm) or at imperfections. Examples are shown in Figure 7.28. The reason for this is unclear, but the same phenomenon was observed by Huang et al. [76], as shown in Figure 4.6. Recall that the metal catalysed dissolution of silicon involves the reduction of H_2O_2 on top of the silver islands. The holes which are generated in this half-reaction diffuse through the silver and are injected into the silicon in contact with the metal, causing the oxidation and dissolution of silicon. The rate of this reaction depends linearly on the concentration of holes. Thus, if the diffusion rate of holes through the silver islands varies across an area covered by silver, for instance due to thickness variations or defects, it is very plausible that the dissolution rate of silicon will vary as a consequence, giving rise to an uneven surface after the processing.

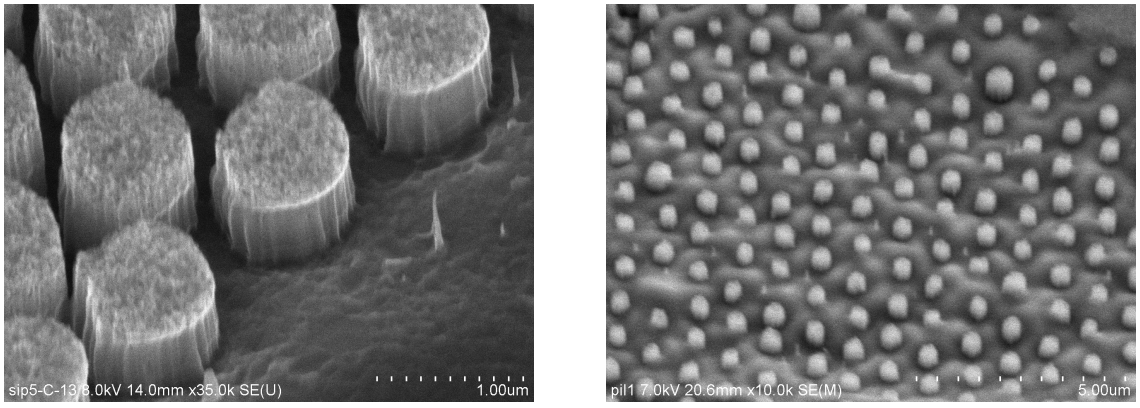

(a) *Sample 800_4* **(b)** *Sample 400_1*

Figure 7.28: *SEM images demonstrating the uneven etch depth*

Another observed imperfection was the etching of the top of the pillars themselves. Ideally the tops of the pillars would be perfectly flat plateaus, untouched by the etch. However, significant surface roughness was observed on all samples, as seen in Figure 7.29. No correlation between etch duration and surface roughness could be found. It is known that the etch rate of silicon by this etchant, even in the absence of silver, is finite and non-zero; silver merely acts as a catalyst to speed up the reaction. Therefore it is possible that the surface roughness is simply caused by the non-catalysed etching of silicon. Another possibility is slightly more involved. Recall from Equation 4.2 that the metal catalysed etch reaction actually occurs by the spontaneous formation of two local electrodes. The reaction at the silver catalyst produces holes which diffuse and cause the dissolution of silicon. It is possible that some holes diffuse to the top of the pillars rather than to the area directly in contact with silver. This would cause erosion

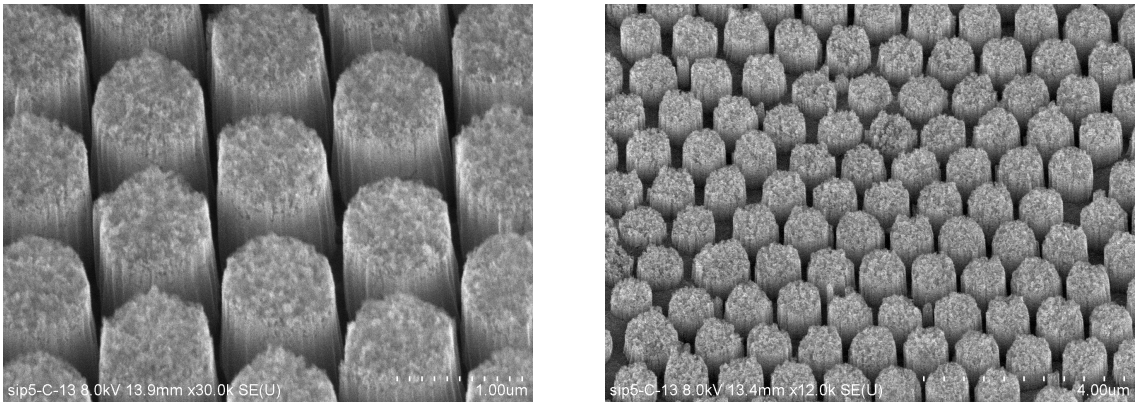

(a) *Sample 800_4* **(b)** *Sample 800_5*

Figure 7.29: *SEM images showing the rough surface of the pillars*

of the pillar tops. As the etch progresses, the distance from the metal particle to the top of the pillars obviously increase, thus reducing the likelihood of this process. This would agree well with the observation that the pillar surface roughness appeared to be independent of the etch duration.

7.4.4 Optical properties

The etched samples appeared dark and matte after removal of the silver and polystyrene, indicating a very diffuse scattering. The reflectivity was measured in the integrating sphere, and the results are shown in Figure 7.30. As can be seen, the reflectivity is indeed very low, with no appreciable systematic difference between the samples. The large increase in reflectivity beyond 1000 nm is not related to the cylinder structures, but rather it is due to the this poorly absorbed light making several passes through the silicon wafer, scattering from the back side of the wafer and exiting through the front side.

The cylinder structure was optimised based on simulations to give a high reflectivity for light of wavelengths 800-1000 nm in the case of normal incidence and light impinging on the cylinders from the silicon side. In this experiment, the reflectivity was measured for light incident from air. Therefore the two are not directly comparable. Moreover, the modeling work done on these structures assume perfectly flat surfaces. This is important for constructive and destructive interference of light reflected from the tops and bottoms of the pillars to arise. A slight deviation from this ideality might be enough to significantly perturb the situation, giving more diffuse scattering.

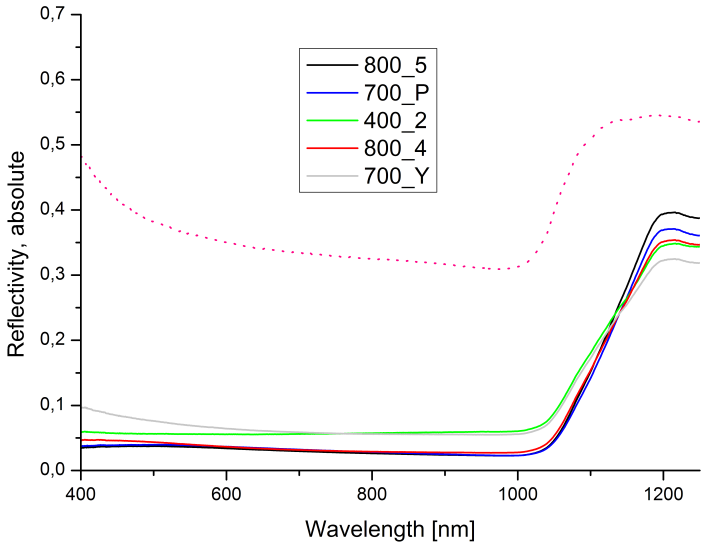

Figure 7.30: *Reflectivity of pillar samples, measured in the integrating sphere setup. The dotted line is the reflectivity of a bare silicon wafer. The increase around 1000 nm is due to the band gap of silicon, as light is reflected from the back side of the wafer*

7.4.5 Summary

It has been shown that metal catalysed etching was successful in creating hexagonal arrays of silicon cylinders on a wafer. The diameter of the cylinders can be tuned by altering the diameter of the template beads, and the pillar height is determined by the duration of the etch. Some structural imperfections are however observed, and it is believed that these are responsible for the low reflectivity from the samples. By further optimisation of the etch parameters, primarily the composition of the etching solution, it is believed that the optical response could be improved.

Chapter 8

Conclusion

In this work, monolayer colloidal crystals were fabricated and used as templates for nanosphere lithography in order to produce different structures that might be used for light harvesting in solar cells.

Monolayer colloidal crystals were successfully obtained on silicon wafer samples by spin coating an aqueous suspension of spheres. By tailoring the composition of the spinning solution and the spinning parameters, high quality monolayers displaying six-armed reflection patterns indicative of a long-range crystal ordering were routinely fabricated using suspensions of various bead diameters. The crystal domains were typically around 1000 μm^2.

Monolayers were then coated with silver before bead removal, leaving patterns of triangular silver particles on the wafer. Island size was tailored by using different sized beads in the monolayer templates, and by varying the amount of deposited silver. A peak in reflectivity was observed, agreeing well the theoretically predicted plasmon resonance frequency for this type of metal particle.

Monolayer templates were also used to fabricate arrays of dimples in a wafer. These dimples were designed to be used as initiation points for the controlled dissolution of silicon by chemical or electrochemical etching. By means of such seed-catalysed etching it will be possible to fabricate cylindrical holes, hemispherical dimples and other structures which may be used as diffraction gratings to scatter light into the solar cell. Arrays of dimples were successfully made by metal catalysed etching, laser ablation using monolayer templates as colloidal microlenses, and selective alkali etching of silicon through holey etch masks. The latter method produced exceptional geometries which should be very well suited for the purpose. No previous demonstrations of this technique have been found in the literature.

Finally, diffraction gratings consisting of hexagonal arrays of silicon cylinders were fabricated by metal catalysed etching. Good control of the structural parameters was obtained, and pillars displaying straight sidewall profiles were successfully made. By

further optimising the etch parameters it will be possible to fabricate more ideal surfaces, which should enhance the optical properties.

Chapter 9

Further work

During the work on this thesis it was decided early on to explore many different techniques and applications rather than spend a lot of time optimising a single process. This was done consciously in order to identify areas which are suitable for closer investigation in a follow-up project at the Institute for Energy Technology. While this approach was successful in that regard, it also inevitably leaves much room for further exploration and process optimisation.

In this section, some of the more important areas for future work will be highlighted. It will be split into four parts: (1) improving the monolayer quality, (2) performing the electrochemical etching using the patterned substrates developed in this work, (3) further developing the dielectric cylinder synthesis, and (4) continuing work on upconversion.

9.1 Monolayer quality

The early work on this thesis was devoted to creating monolayer colloidal crystals. The preceding project work had focused entirely on multilayer crystals, and so a process for monolayer fabrication had to be developed. While the monolayers obtained in this project were deemed sufficiently good to be used for both structural and optical characterisation of final synthesised structures. Other groups have achieved significantly larger crystalline domains, and a better crystal quality in general. Some of the best results reported in literature were obtained using highly toxic chemicals, such as in the very impressive results by Jiang et al. [42, 43]. Attempts were made at re-creating these results by using other, non-toxic viscous solvents, with poor results, and this work was therefore abandoned. This is something that would definitely be worth exploring further. In particular, using solvents with high boiling points and elevating the temperature of the spin coating process would be very interesting, as the higher kinetic energy of the particles should enhance their Brownian motion and enable them to map

larger areas of the substrate to find the most energetically favourable positions in which to settle, giving fewer crystal defects and larger domain sizes. In addition it would be very interesting to study the effects of humidity during spin coating. All this could be achieved by the acquisition of a cupboard with humidity- and temperature control.

9.2 Electrochemical etching

One of the big successes of this work was the development of a completely new method for the formation of seeds for electrochemical etching. A silicon nitride etch mask was fabricated by nanosphere lithography, and alkali etching was performed through the holes in the mask to create hexagonal arrays of sharp inverted pyramids in the wafer. Such arrays were successfully made on quarter wafers, which are large enough to be used in our electrochemical etching cell. The next natural step would be to carry this work further by actually performing the electrochemical etching step. Pores of these dimensions are most easily formed in lightly doped substrates, and p-n junction needs to be formed at the back side of the wafer before the etching can be done. Many parameters need to be optimised, such as bias voltage, illumination, etchant concentration, etch bath temperature, and etch duration. This is in other words a substantial project, but if good process control can be achieved, the potential reward is also immense.

9.3 Dielectric cylinder arrays

Some exciting work was also done on the synthesis of dielectric cylinder arrays by metal catalysed etching. The results were given in Section 7.4. Cylinders of clearly defined diameters, matching the diameters of the beads in the monolayer template, were indeed fabricated. However, the optical properties of the samples were not quite as expected, and SEM investigations revealed areas of clearly imperfect etching. It is believed that the composition of the etching solution should be altered to reduce the etching rate and minimise the formation of hydrogen gas bubbles on the substrate, as this is believed to be a major factor accounting for the uneven etch rates observed.

Once better process control has been achieved, cylinder arrays of different dimensions (diameters and heights) should be fabricated on the back side of thin ($\sim$ 50 µm) silicon wafers. The reflectance and transmittance from the front side should be measured and compared to that of a bare wafer, as well as a wafer with an aluminium back side reflector. In this way the scattering efficiency and consequent absorption enhancement caused by the cylinder arrays could be determined. This can easily be achieved by using an integrating sphere. Finally, a concept for the inclusion of these structures in a working solar cell should be developed, including back side contacting.

9.4 Upconversion

As mentioned in the introduction, significant attention was also devoted to the development of a proof-of-principle demonstration of an upconversion scheme. In essence, the idea is to embed the upconversion material inside a 3D photonic crystal exhibiting a full photonic band gap at a frequency which can block an unwanted radiative relaxation of the upconversion material. At present, lanthanides are by far the most explored materials for upconversion, but they are plagued with an intrinsically low efficiency because they rely on quantum mechanically stable intermediate states to achieve good pumping efficiencies. If successful, our idea would pave the way to using novel upconversion materials.

The work done so far on this topic is included in the following Appendix. The experiment which was attempted was a simple demonstration that a luminescent material embedded in a 3D photonic crystal can indeed be quenched by the photonic band gap. However, there were some fundamental flaws in the experimental design which left these experiments unsuccessful. The photonic crystals used did not display a full photonic band gap, but only incomplete ones, which made the detection of quenching directionally dependent. This complicated the experiment significantly.

The work on upconversion was motivated by the successes in the preceding project work at fabricating multilayer inverse opals infiltrated by atomic layer deposition (ALD). The infiltration material used in the project work was titania, whose dielectric constant is too low to allow a full photonic band gap to arise. The ALD work was conducted at the University of Oslo, supervised by Prof. Ola Nilsen. Their group are currently developing an ALD recipe for the depositon of silicon, whose dielectric constant is indeed high enough to yield full photonic band gaps in an inverse opal. Once this work is successful, multilayer colloidal crystals loaded with luminescent material can be infiltrated and inverted with silicon. The infiltration parameters and structure dimensions must be tailored such that the emission wavelength of the luminescent material overlaps the photonic band gap of the opal. Then, the luminescence should be quenched, which would provide an irrefutable proof-of-concept demonstration.

With this demonstration done, work can begin on searching for suitable candidate materials for an actual demonstration of an upconversion process which is enabled by the presence of the photonic band gap.

Further information about the work done so far and the theory behind is presented in the following Appendix.

Appendix A

Upconversion

A.1 Theory of upconversion

As described in the introduction, upconversion is a process for utilising the low-energy part of the solar spectrum which ordinarily could not be absorbed by a solar cell. In the case of crystalline silicon, this constitutes 27% of all incoming photons [93]. In essence, an upconversion material absorbs low-energy light and emits high-energy photons which can subsequently be absorbed by the solar cell [94]. This pushes the theoretical maximum efficiency of a silicon cell from 29% to 40.2% [95].

A.1.1 Upconversion processes

Atoms display several discrete electronic energy levels with a defined spacing, and electrons may be excited from the ground state to a higher energy level if irradiated by light of this particular energy $E = h\nu$. A ladder analogy is frequently used, where the steps of the ladder represent energy levels. In upconversion, an electron absorbs several photons each "kicking" it one step up the ladder. When the electron relaxes back to the ground state, the energy may be released by emission of a photon of greater energy than each absorbed photon. This is the definition of an upconversion process. For solar cell applications one generally seeks to absorb light in the near-infrared spectrum and emit light of wavelengths well below the band gap of silicon, where absorption efficiencies are high.

There are several ways in which upconversion can occur. The simplest mechanism is termed excited state absorption (ESA). The first incoming photon excites an electron in the upconversion ion to an intermediate state. A second incoming photon can then furher excite this electron to a higher state, and so on. The energies of these photons need not necessarily be the same, depending on the spacing of energy levels in the particular ion. If the excited electron relaxes via a radiative transition path, a photon

of high energy will be emitted which may be absorbed by the solar cell. For ESA to be efficient, it is crucial that the lifetime of the intermediate state(s) is long, and that any non-radiative relaxation paths for excited electrons are suppressed [95].

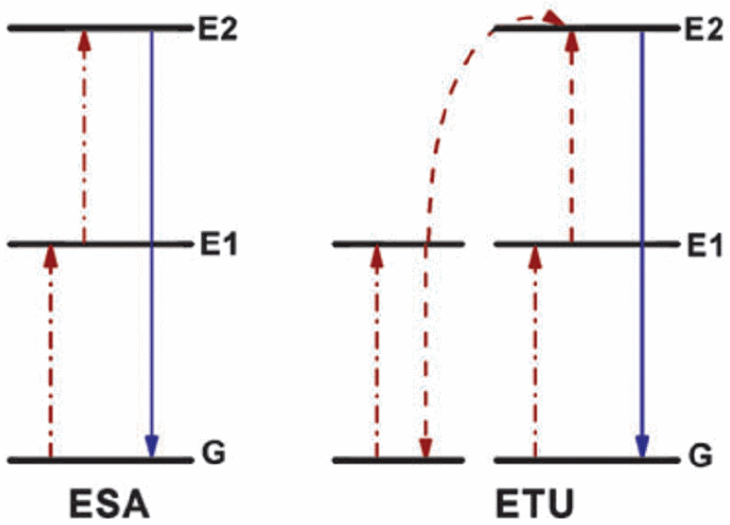

Figure A.1: *Overview of the two classes of upconversion mechanisms, ESA (excited state absorption) and ETU (energy transfer up-conversion). Dashed/dotted, dashed and full arrows represent photon excitation, energy transfer and photon emission processes respectively. G represents the ground state, while $E1$ and $E2$ are the intermediate and excited states respectively. Figure from Wang et al. [94]*

In another upconversion mechanism, called energy transfer up-conversion (ETU), the low-energy light is absorbed by ions known as sensitisers (donors) attached to the luminescent centre. The ions act as "antennas" which transfer their energy to the luminescent material, called the activator (acceptor), which finally emits the output photon. The excited level of the sensitiser should be similar to that of the activator for an efficient process. ETU has been demonstrated to be approximately two orders of magnitude more efficient than ESA [96]. ESA and ETU are both shown schematically in Figure A.1.

In ETU, the method by which energy is transferred from sensitiser to activator can be radiative or non-radiative, resonant or non-resonant. The efficiency of the energy transfer process is of paramount importance for the overall quantum yield of the upconversion process, and the degree of overlap between the emission spectrum of the sensitiser and the absorption spectrum of the activator must be as large as possible. The different mechanisms are shown in Figure A.2. The rate of non-radiative multiphonon relaxation between levels with energy gap ΔE goes like

$$k_{nr} \propto \exp\left(-\beta \frac{\Delta E}{\hbar\omega_{\max}}\right) \tag{A.1}$$

where β is a constant related to the host material, and $\omega_{\max}$ is the highest energy vibrational mode (phonon energy) of the host lattice. The larger the energy gap the larger the probability that a transition is radiative rather than non-radiative [97].

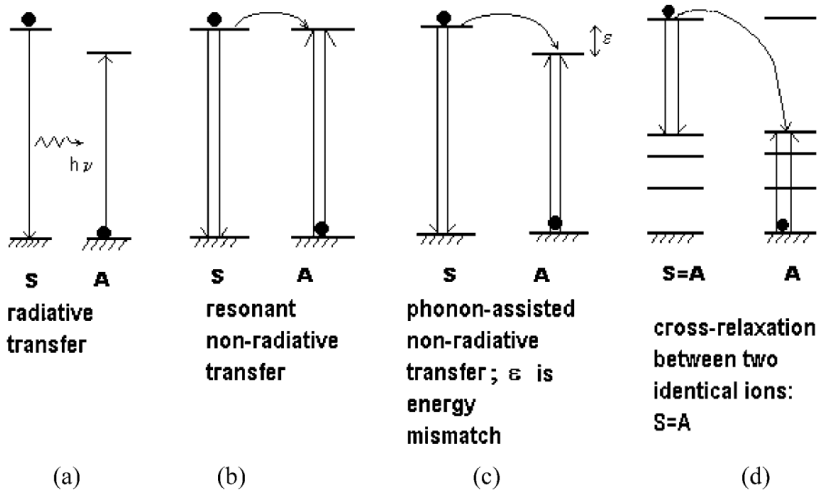

Figure A.2: *Overview of energy transfer mechanisms between sensitiser (S) and activator (A). Figure modified from Auzel [96]*

In practise, upconversion systems usually consist of a host material which is doped with activator and sensitiser ions. The distance between sensitiser and activator, R, is of crucial importance. If radiative transfer is the dominating mechanism, the transfer probability is proportional to $\tau_S R^{-2}$, while for non-radiative processes it scales as $\tau_S R^{-6}$ [96]. τ_S denotes the lifetime of sensitiser excited state. Therefore, sensitiser doping levels need to be very high in the case of non-radiative processes, usually around 20 mol%. Radiative energy transfer can thus be advantageous because lower concentrations of sensitiser ions need to be used. Activator content is normally around 2 mol% to minimise unfavourable cross-relaxation processes between activator ions (mechanism D in Figure A.2).

A.1.2 Material requirements

Finding materials suitable for use in upconversion schemes is not trivial, and a number of stringent requirements and considerations apply. The most important of these will be discussed below.

Choice of activator

The activator needs to fulfil certain requirements [94]:

1. The lifetime of electrons in the intermediate state(s) of the activator needs to be long. The probability of finding an electron in an intermediate state decays exponentially with time, and it is thus crucial that the half-life of this process is long
2. Radiative relaxation from the excited state must dominate over non-radiative relaxation. From Equation A.1 this means that energy levels should be far between
3. Relaxation to sub-levels other than to the ground level must be minimised.
4. The energy gap between the energy levels of interest must match the energies of the photons to be absorbed/emitted

The lanthanides have been shown to be suitable candidates meeting these criteria, in particular erbium (Er), holmium (Ho) and thulium (Tm). They exhibit two quite evenly spaced energy levels which may be excited by low-energy photons, which together may yield a high-energy photon via relaxation to the ground state. Lanthanides exist in their most stable form as trivalent ions, such as Er^{3+}, and are therefore typically surrounded by negative ions which may acts as sensitisers.

Choice of sensitiser

Once an activator has been chosen, appropriate sensitiser ions need to be found. There are three main criteria [94]:

1. The absorption cross-section of the ions must be high, meaning that incoming light has a high probability of being absorbed over a wide energy spectrum
2. The sensitiser should be able to absorb over a large wavelength span in the relevant energy range, typically close to the band gap of the solar cell
3. The sensitiser must match well with the activator to maximise the energy transfer efficiency

Commonly the lanthanide ytterbium (Yb) is used as a sensitiser in its trivalent form. This has a high absorption cross-section in the near infrared spectrum with the absorption band located at 980 nm. The path length of this wavelength in crystalline silicon is around 150 µm, as shown in Figure 1.2a, which means that these photons will have a high transmission probability in ultra-thin crystalline wafers. This is the type of solar cell for which upconversion is considered to be most relevant, in addition to in thin films, which means that upconverting light of 980 nm makes sense for crystalline solar cells.

Choice of host material

The host material also needs to fulfil certain requirements:

1. It must be optically transparent for light of the relevant wavelengths
2. It must be able to accommodate the sensitiser and activator ions in the lattice. For substitutional rather than interstitial doping, the radius of host and dopant ions should be similar to avoid defects
3. As can be seen from Equation A.1, the lattice phonon energies should be low to suppress non-radiative relaxation processes. In general, if it takes more than six phonons to bridge a transition, radiative relaxation dominates over nonradiative processes [97].
4. The material must be chemically stable and not degrade when exposed to radiation
5. A deposition technique must be available which is compatible with the rest of the structure synthesis (the solar cell in this case)
6. The bulk material should be fairly inexpensive

A.1.3 Light management for upconversion

Unfortunately, the maximum efficiency of upconversion demonstrated so far is only in the order of 10^{-6} [95, 97, 98], using a single-wavelength excitation source (typically a laser). In a real solar cell the incoming light is of course of a broad wavelength range. How this will affect the efficiency of the process remains an issue of some debate, because it is possible that light of different wavelengths can cooperate in the pumping process if the energy levels are spaced in a suitable way. In either situation, it is clear that the light needs to be concentrated. As the upconversion process relies on the simultaneous excitation by several photons in close proximity, the efficiency does not merely scale linearly with incoming light intensity P_{in}. Rather, the luminescence quantum efficiency (LQE) which is often regarded as a measure of the upconversion process quantum efficiency, goes like [97]

$$\text{LQE} \propto \frac{P_{in}^{(n-1)}}{(1-L)} \tag{A.2}$$

where n is an empirical constant and L represents losses due to effects such as absorption, reflection and non-radiative recombination. Observe from Equation A.2 that quantum efficiencies increase with incident light power, provided the exponential n is

greater than 1, as is the case for the systems of interest. Typically the quantum efficiency will have a maximum at a fairly high concentration, before flattening out due to heating of the material by nonradiative relaxation processes [99]. Generally, however, a high light concentration is desirable.

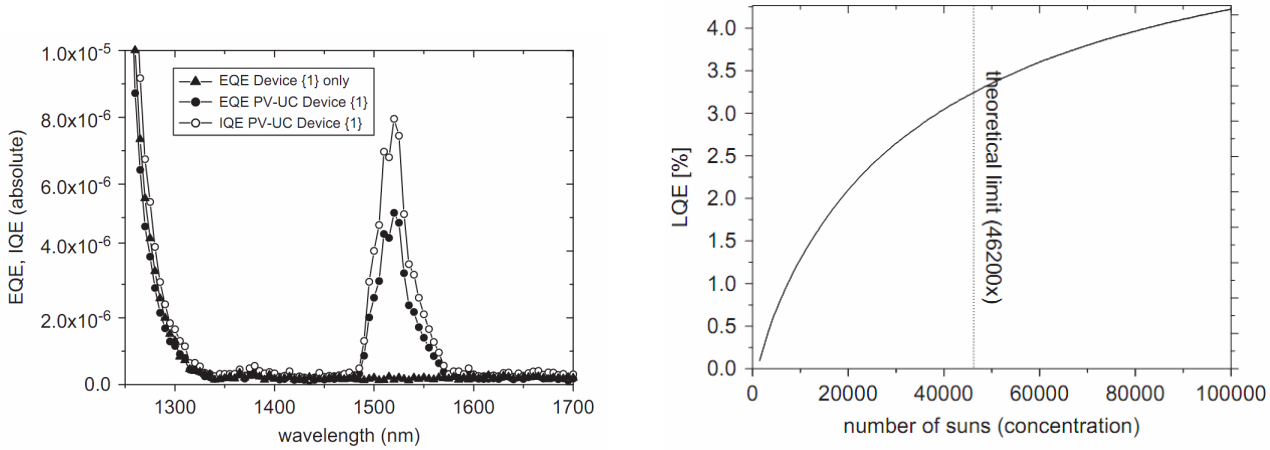

(a) *Quantum efficiency of crystalline solar cell with $NaY_{0.8}F_4{:}Er^{3+}_{0.2}$ upconverter on the back side. Buried contacts, with diffuse back reflector.*

(b) *Upconversion quantum efficiency as a function of light concentration. From Shalav et al. [97]*

Figure A.3

Therefore, it is clear that light with wavelengths in the absorption range of the sensitiser should be concentrated as much as possible to enhance the upconversion quantum efficiencies. But even with extreme concentration and an LQE of unity in the absorption range of the sensitiser, most of the sub-bandgap solar spectrum would still go unused due to the narrow absorption band. The absorption band for most sensitisers considered so far is a 100 nm range around the maximum absorption wavelength [93]. This is shown in Figure A.3a. Therefore it has been suggested to combine the upconverter system with a fluorescent material which would absorb the sub-bandgap light and emit photons within the absorption range of the sensitiser [100]. In short, fluorescent quantum dots absorb low-energy light ν_2 and emit at a particular frequency ν_3 which is upconverted to a frequency ν_1 to be absorbed by the solar cell. This is shown in Figure A.4.

A.1.4 Upconversion in 3D photonic crystals

There are two main reasons why 3D photonic crystals might be of interest for use with an upconversion system. These will now be discussed.

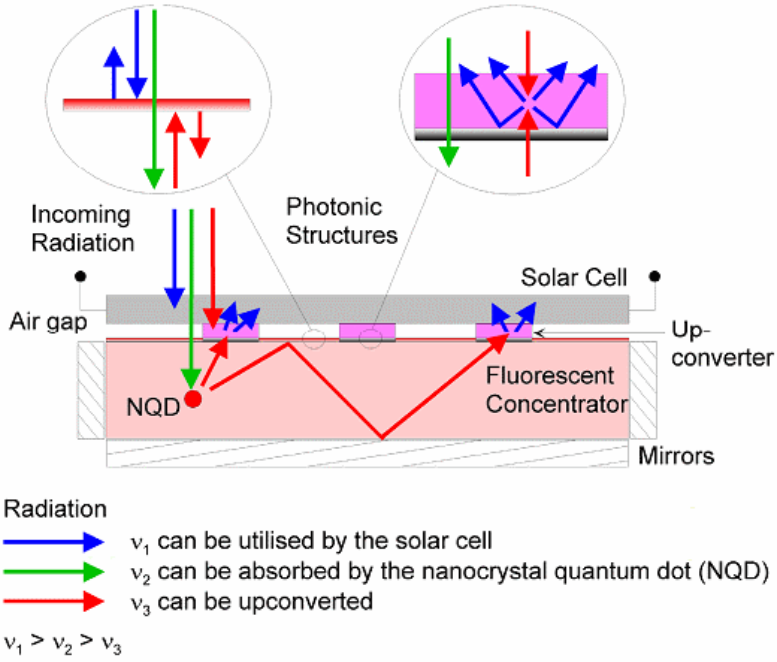

Figure A.4: *Upconversion scheme using photonic crystals. Quantum dots in the fluorescent concentrator absorb broad ranges of low-energy light around ν_2 and emit a narrow spectrum around ν_3. This light is subsequently upconverted to shorter wavelengths ν_1 which are transmitted back to the solar cell for absorption. Figure from Goldschmidt [93].*

Spectral filters and light concentration

In the type of upconversion scheme described above, spectrally selective filters are needed on several interfaces. The upconversion- and fluorescent materials must be kept separated from each other to prevent upconverted radiation to be absorbed by the fluorescent material. Additional efficiency can be expected if the upconversion material is isolated on small "islands" rather than covering the entire wafer. This is because upconversion is a non-linear process which becomes more efficient when light is concentrated.

Therefore, Goldschmidt et al. [93] proposed to make a fluorescent concentrator below the cell wherein light of frequency ν_3 is concentrated. A filter which transmits low energy light (ν_2) and reflects light emitted by the fluorescent material (ν_3) must thus be placed at the interface between the fluorescent concentrator and the upconverter. To prevent upconverted light from re-entering the fluorescent concentrator there should also be a spectrally selective mirror at the upconverter/fluorescent concentrator interface, reflecting light of frequency ν_1.

The allure of photonic crystals is that they are able to display sharply defined reflectivity peaks due to photonic band gaps, and may therefore be used as spectrally selective filters. They can also be used for light concentration if their reflectivity is high enough

and omnidirectional.

Suppression of non-radiative transitions. Novel activators

As mentioned in Section A.1.2, a very important design criterion for an activator is that the lifetime of the intermediate state(s) is long. This is necessary to facilitate pumping from the intermediate to the final excited state. This, along with the highly suitable energy level "ladder", is the main reason why lanthanides are the main materials considered for upconversion today.

However, a major drawback with the lanthanides is that a quantum mechanically stable intermediate state also infers that the pumping efficiency from the ground level to the intermediate state is very low. This is a major reason why the quantum efficiency of the best upconversion systems is so poor. Therefore, if upconversion is to ever be implemented on a significant scale in the solar cell industry, there is a great desire to design an upconversion system which uses an active material other than the lanthanides, in which the lifetime of the intermediate state(s) is extended not by the quantum mechanical transition probabilities of the active material but by some other method which does not affect the probability of excitation from the ground state.

Our idea is to use a photonic crystal to achieve this. Recall that within the band gap of a photonic crystal, light is not allowed to propagate. The concept is to embed the upconversion material inside a photonic crystal whose bandgap is tailored to block an unwanted radiative relaxation pathway from the intermediate state of the active material. Non-radiative relaxation pathways can be avoided if the phonon energy of the photonic crystal is also low, as mentioned in Section A.1.2. If both these criteria are met, the lifetime of the activator intermediate state can be prolonged significantly. In such a system, the design criteria for the activator can be relaxed, since it is no longer required that the intrinsic lifetime of the intermediate state is long. Therefore more emphasis can be placed on finding an activator whose excitation probability is high. For upconversion to ever be implemented on a significant industrial level, the activator should be both abundant and inexpensive, which is not the case for the lanthanides.

The band diagram of an activator designed to work in this scheme is shown in Figure A.5. G, E1, E2, and E3 refer to the ground state and the first- second and third excited states. (E1 and E2 can also be called intermediate states) First, an electron is excited from the ground state to the second excited state and quickly relaxes to the first excited state. Here, electrons are not allowed to relax further back to the ground state because the band gap of the photonic crystal coincides. Therefore, the lifetime of the E1 state is greatly extended, such that excitation from E1 to the excited state E3 is very much more likely to occur. Finally, electrons relax back to the ground state, emitting an up-converted high-energy photon.

Finally it should be noted that this proposed scheme would only work as intended if a full photonic band gap is used. If the bandgap is incomplete, light of all wave-

lengths will be allowed to propagate in all directions inside the structure, except for the narrow (wavelength dependent) Bragg angle. This is clearly not useful for a design implementation.

A.2 Experimental

The demonstration attempted here consisted in embedding luminescent CdTe nanocrystals inside a multilayer colloidal crystal, and investigating the quenching of luminescence due to band gap effects of the host material. The details of the experiments will now be presented.

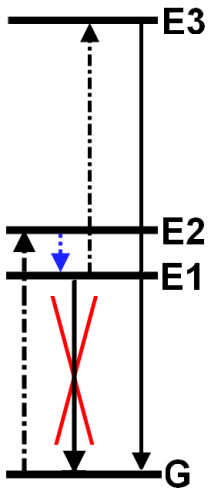

Figure A.5: *Band diagram of an ideal activator. Explanation in text*

A.2.1 Colloidal crystal multilayer synthesis

Spin coating was also explored for the synthesis of multilayer crystals with good success. However, recall that the main motivation for the formation of multilayer crystals in this work was to embed fluorescent nanoparticles inside the colloidal crystal. Spin coating was deemed to be impractical for this purpose, as this is a method which lends itself most readily to the mass production of identical samples. Therefore it was decided to build upon the results from the preceding project work [101] and fabricate the multilayer crystals by vertical EISA, as described in Section 3.2.3. A solution of PS beads was prepared in a 20 ml teflon beaker using pipettes. The solution was diluted to the desired concentration using DI water. The beaker was then placed in an ultrasonic bath for 5 minutes to break up any aggregates of colloidal spheres that may have formed. Initial experiments with shorter ultrasonic bath treatments revealed some aggregation of spheres, but 5 minutes appeared sufficient to avoid this problem.

A cleaned substrate was inserted vertically into the beaker, for a maximal submersion depth of approximately 30 mm. The beaker was placed in a pre-heated heating cupboard, model Termaks TS 8136, and left there for the solvent to evaporate and the spheres to self-assemble on the substrate surface. This would take approximately 24 hours at 63°C, which was found to be the optimal temperature by Granlund [17].

In the project work it was discovered that the fans in the heating cupboard caused violent air circulation, resulting in uneven film deposition. As the fans could not be disabled, the beaker was instead partially covered with aluminium foil to reduce air flow over the surface. This was successful in creating high-quality multilayer films [101].

A.2.2 Upconversion demonstration

In Section A.1.4, an upconversion scheme was presented where the activator would be embedded within a 3D photonic crystal whose band gap matched an unwanted relaxation pathway of radiative relaxation, thereby extending the lifetime of an intermediate electronic state in the activator.

A full blown implementation of this novel idea is well beyond the scope of this thesis. However, a proof-of-concept demonstration of the suppression of radiative relaxation pathways by a 3D photonic crystal is nevertheless attempted. The idea was to embed luminescent nanocrystals inside a photonic crystal with a bandgap overlapping the emission peak of the luminescent material. By comparing the luminescence from such samples to similar samples with no bandgap overlap, the suppression of these wavelengths can be measured. A photoluminescent material is one which, when irradiated by high-energy light, will re-emit ligth of lower energy.

This type of experiment has been conducted in the past by other groups. Noteably Lodahl et al. [102], and more recently Yang et al. [103], explored the use of inverse opals for this purpose. Inverse opals were also fabricated in the preceding project work, with highly tuneable incomplete bandgaps. The reflectivity of one such inverted opal displaying a photonic band gap at the desired wavelength is shown in Figure A.6 (blue line). However, as can be seen, this particular structure also exhibits high reflectivity over a broad wavelength range, overlapping with the excitation wavelength used (vertical purple line). Therefore this idea was abandoned. Instead, a different approach was chosen, the details of which are described here.

Photoluminescent cadmium telluride (CdTe) nanoparticles of diameter 2-7 nm were purchased from Plasmachem, product identification PL-QDN-540. These quantum dots absorb over a wide wavelength range and emit at 540 nm. The quantum dots were embedded into multilayer colloidal crystals during synthesis, the recipe for which was given in Section A.2.1. The only modification used was that some of the DI water was replaced with an aqueous suspension of quantum dots. The idea was that some quantum dots would find their way into the colloidal crystal during growth and be embedded randomly on the bead surfaces throughout the entire thickness of the colloidal crystal.

Three sets of samples were made on glass substrates, which were all identical except the diameter of the beads in the colloidal crystal were different. As explained in Section 2.1.1, the band gap of a photonic crystal can be tuned by changing its period, i.e. the dimensions of the fundamental building blocks. Thus, for the reference samples the band gap wold occur at wavelengths other than the emission wavelength of the luminescent nanocrystals. This would provide a control experiment to eliminate any absorption losses in the plastic beads.

The absorption and emission spectra of the nanocrystals are shown in Figure A.6, along with the reflectance of two candidate host materials. Note that this graph is plotted for the case of an 8° angle of incidence relative to the sample normal, due to the design of the integrating sphere.

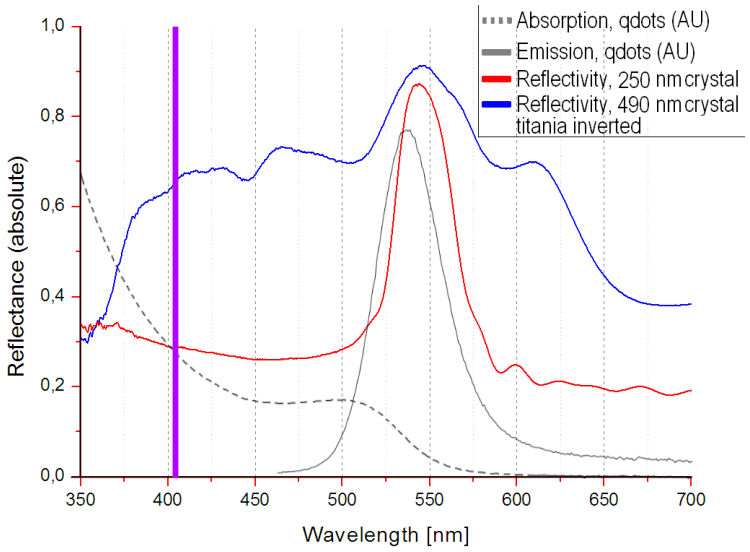

Figure A.6: *Absorption and emission spectra for the quantum dots, as well as reflectivity of the host colloidal crystal at an 8° incidence. Observe how reflectivity peak (corresponding to the band gap) of the host material coincides with the emission peak of the quantum dots.*

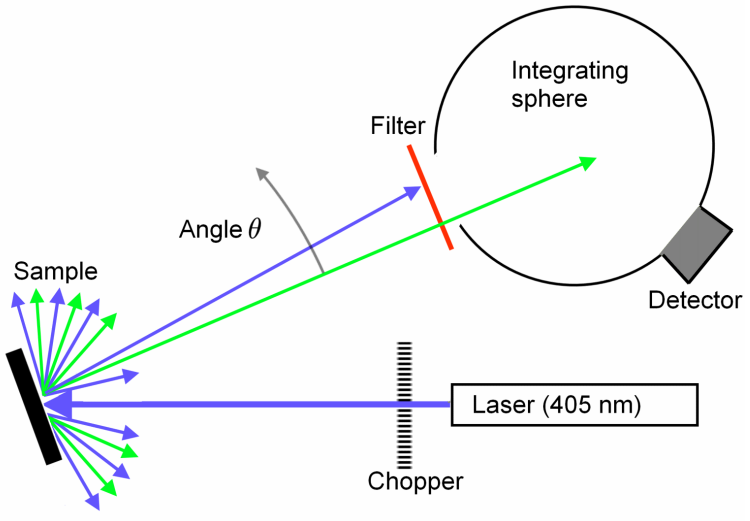

Figure A.7: *Schematic of experimental setup for detecting luminescence. Excitation wavelength shown as blue arrows, luminescent light shown as green*

Observe also from Figure A.6 how the absorption efficiency of the quantum dots increases for shorter wavelengths. In the experiment, the samples were illuminated by a 200 mW 405 nm laser. The beam was de-focused such that the spot size at this distance was approximately 1x1.5 cm. A detector was placed inside an integrating sphere to attain a stronger signal, and the sphere was scanned across a circular arc of radius 30 cm with the sample at the center, to measure the emitted light as a function of angle

relative to the sample normal. At this configuration the port opening on the integrating sphere captures approximately a 5° cone of light. The sample was mounted at a slight angle with respect to the incident beam to avoid signal loss due to the chopper and laser mount. An optical filter is used to block any of the excitation light. A schematic of the experimental setup is shown in Figure A.7.

A.3 Results and discussion

Luminescent nanocrystals were embedded into multilayer colloidal crystals consisting of polystyrene beads of diameters 190, 250 and 300 nm respectively. Clear luminescence was observed from all samples when illuminated with the 405 nm laser beam.

	UC1	UC2	UC3
Bead diameter [nm]	190	250	300
Band gap [nm]	440	555	635

Table A.1: *Samples investigated here, embedded with CdTe nanocrystals*

To better understand the expected behaviour of the samples and the presence of band gaps, their reflectivity was first measured in the integrating sphere. The results are shown in Figure A.8a. Clear reflectivity peaks are seen, corresponding to the photonic band gaps of the host lattice.

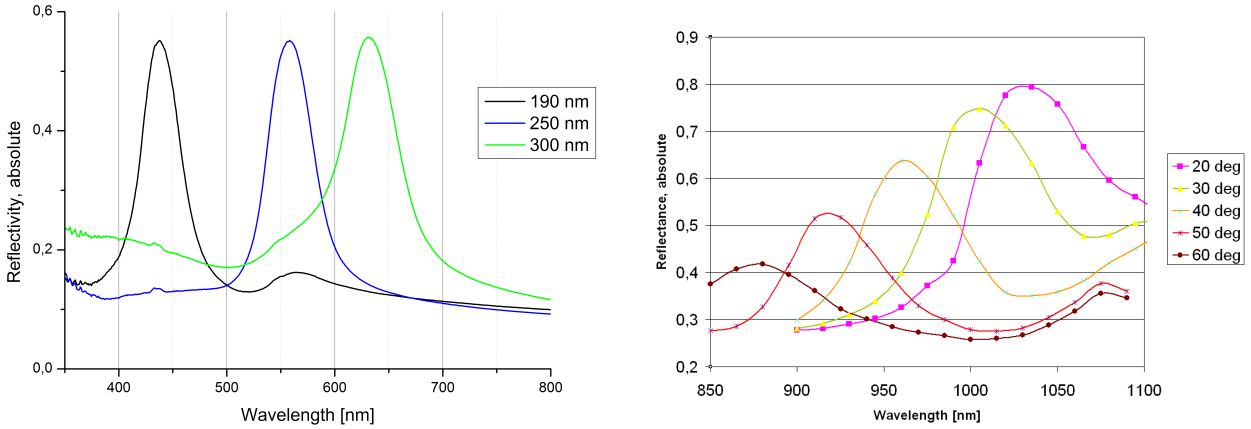

(a) *Reflectivity peaks of the samples, measured at 8° incidence in the integrating sphere*

(b) *Shift of the photonic band gap as a function of angle of the propagation angle of light with respect to the sample normal. Colloidal crystal on silicon. Results from the preceding project work [101]*

Figure A.8: *Band gap considerations of the samples*

In the preceding project work, it was investigated how the band gap of such a 3D opal shifts as a function of the angle of light. The precise position of the reflectivity peak

depends on the angle at which the light travels with respect to the sample normal. This is seen in Figure A.8b. From this graph the peak shift is found to be approximately 4 nm per degree. Based on this collected information, it is found that the band gap of Sample UC2, the 250 nm colloidal crystal, should overlap perfectly with the emission peak of the luminescent CdTe nanocrystals when the detector is oriented at 12° with respect to the sample normal. Similarly, it can be calculated that the band gap of Sample UC1 should overlap with the incident 405 nm laser beam when illuminated at approximately 18° incidence, preventing laser light from propagating into the colloidal crystal.

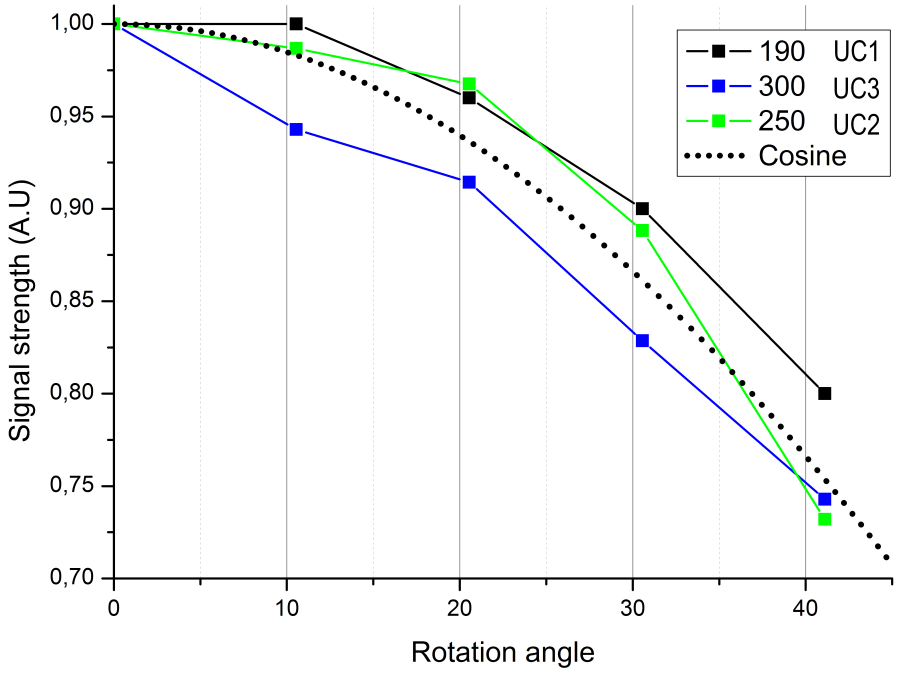

Figure A.9: *Signal strength as a function of angle with respect to the sample normal, θ, for the samples investigated*

The angular dependence of the measured intensity from all three samples was then investigated. The intensity was found to drop off following a cosine dependence, as shown in Figure A.9. If luminescence is assumed to be isotropic, a sample can be considered a planar emitter. As the detector angle θ is increased, the area of the sample projected onto the detector is decreased following a cosine relationship. The results were thus in agreement with the expected trend for regular planar luminescent samples.

However, no dip in emission was observed from Sample UC2 when the detector was oriented at 12° with respect to the sample normal, where the band gap was expected to overlap with the emission peak of the luminescent nanocrystals. Likewise, there was no clear drop in luminescence from Sample UC1 when oriented at 18° with respect to the

laser incidence, where much of the laser beam should be prevented from propagating into the colloidal crystal. In short, no evidence of band gaps prohibiting the propagation of light in the crystals could be detected in any of these experiments.

The fact that no band gap was detected for these samples could in principle be attributed to the luminescent material deposited on the very face of the colloidal crystal, which would of course not be affected by the band gap of the bulk crystal. Also, CdTe nanocrystals in the outermost layers of the colloidal crystal would be expected to luminesce quite unhindered, since the band gap only becomes significant once the crystal exceeds approximately 5 layers [17].

Also, the reflectivity from the samples within the band gap is not unity, but rather around 55% at a near-normal incidence, as shown in Figure A.8a. This means that only approximately half of the emitted luminescence is expected to be quenched, even within the band gap. This is even more true when measuring at a more oblique angle, in which case the reflectivity peaks become broader and lower, as shown in Figure A.8b. Therefore luminescence is not expected to be completely quenched even in the best case scenario.

In conclusion, the experiment at this stage was not successful in demonstrating how light may be quenched by a photonic band gap. Other groups have successfully performed such demonstrations by means of more sophisticated experiments. It must also be emphasised that for a 3D colloidal crystal to be used to quench radiative relaxation pathways in upconversion, as is the ultimate goal, a full photonic band gap is necessary. The opals used in this experiment do not exhibit such a band gap, though it is known that opals infiltrated with silicon may do so, which is promising for this application.

Appendix B

E-MRS conference material

As part of the project, the author was invited to attend the European Materials Research Society (E-MRS) Spring Meeting in France, May 9-13 2011. As part of that, an article was written based on work from this thesis as well as the preceding project work, which is currently in review, scheduled for publication in the Elservier journal *Energy Procedia*. A poster was also made for the poster session of the parent symposium *(Advanced inorganic materials and concepts for photovoltaics)*. The poster and article are reproduced here.

COLLOIDAL CRYSTALS AS TEMPLATES FOR LIGHT HARVESTING STRUCTURES IN SOLAR CELLS

E. Haugan [a], H. Granlund [b], J. Gjessing [a] and E. S. Marstein [a]

a) Section for Renewable Energy, Institute for Energy Technology, Norway

b) Department of Physics, Norwegian University of Science and Technology, Norway

INTRODUCTION

The silicon wafer solar cell industry is moving towards thinner and thinner wafers to reduce costs and energy consumption. Unfortunately, thinner wafers also allow more low-energy photons to pass through the cell without being absorbed. Therefore light trapping (harvesting) is becoming an issue of increasing significance. Periodic gratings with lattice periods close to the photon wavelength have been shown to be very interesting for such applications. We have synthesised various periodic light harvesting structures for solar cells, using templates made from suspensions of beads.

EXPERIMENTAL

Template synthesis. Multilayer colloidal crystals were fabricated by evaporation induced self assembly. Samples were placed in an aqueous 0,75% sphere suspension and the water was slowly evaporated. Monolayer colloidal crystals were made by spin coating a 30% aqueous sphere suspension at 5500 RPM for 30 s.

Inverse 3D opals. Multilayer crystals were infiltrated with 50 nm titania by atomic layer deposition (ALD) before the plastic beads were removed by heat treatment (calcination). Figure 1 shows the reflectivity of a 3D opal (SEM image in Figure 2) before and after bead removal. Multiple reflectivity peaks are seen, corresponding to photonic band gaps. The peaks are too narrow for these structures to be used as broad spectrum back reflectors, but they might be interesting as selective reflectors.

2D patterning. Monolayers were used as templates for two different techniques:

In method # 1, we fabricated a silicon nitride etch mask with 100 nm diameter holes, which was used for alkali etching. This was done by coating monolayer crystals with silicon nitride by PECVD. After sphere removal by sonication, a nm-thin nitride film covered the entire sample except at the contact points between beads and wafer, as seen in Figure 3. The dark spots in this figure show the exposed silicon substrate. An alkali (KOH) etch was then performed. The nitride layer acts as an etch barrier for the etch. The final structure is shown in Figure 4, where pyramidal pits characteristic of alkali etching are seen.

In method # 2, we used metal catalyzed etching to fabricate hexagonal arrays of triangular pits. Monolayer colloidal crystals were coated with 70 nm of silver before sphere removal by sonication, and then submerged in a 4.6 M HF / 0.44 M H_2O_2 solution. Silver acts as a catalyst for the etching of silicon by this solution. Figure 5 is a top-down image showing pits etched by this method. The dark semi-triangular spots are where the silver islands were prior to etching. As can be seen in Figure 6, pits have been dug out beneath the islands by the silver catalysed etch.

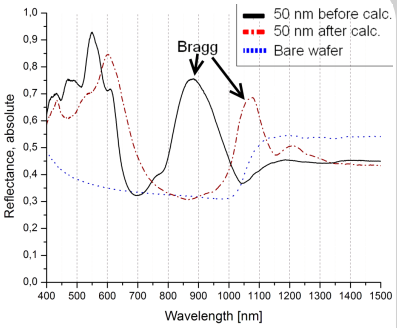

Figure 1. *Reflection from 3D opals*

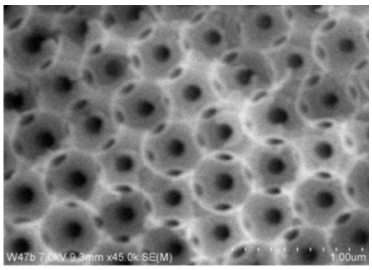

Figure 2. *Inverted titania opal*

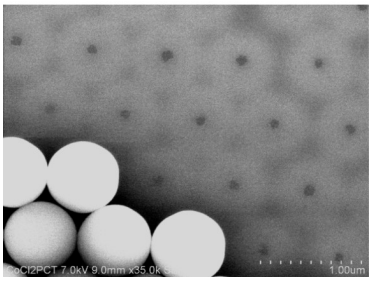

Figure 3. *Silicon nitride etch mask*

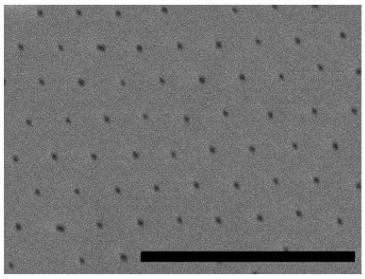

Figure 4. *Alkali etched pits Scale 4 µm*

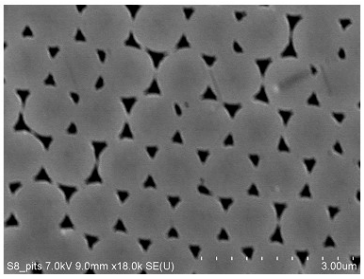

Figure 5. *Silver catalysed pits*

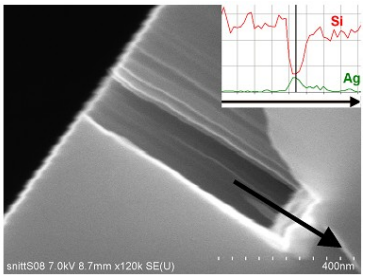

Figure 6. *Silver catalysed pit, cross section*

CONCLUSION

In conclusion, we have successfully manufactured single- and multilayer colloidal crystals on silicon wafers and used them as templates for the production of various geometries intended for light harvesting in solar cells. Specifically, we have made titania inverse opals displaying multiple reflectivity peaks whose wavelength position can be tuned by altering the degree of infiltration and template bead size.

Also, we have demonstrated two different techniques for the formation of hexagonal arrays of dents or dimples in a wafer. These methods can either be used to form 2D light harvesting structures directly, or to form initiation points ("seeds") for further processing into honeycomb structures by chemical- or electrochemical etching.

Corresponding author: einar.haugan@ife.no, telephone +47 95734413

EMRS conference 2011, Symp. R, "Advanced Inorganic Materials and Concepts for Photovoltaics"

Available online at www.sciencedirect.com
ScienceDirect
Energy Procedia 00 (2011) 1–5
Energy Procedia
www.elsevier.com/locate/procedia

European Materials Research Society Conference
Symp. Advanced Inorganic Materials and Concepts for Photovoltaics

Colloidal Crystals as Templates for Light Harvesting Structures in Solar Cells

E. Haugan[a,*], H. Granlund[b], J. Gjessing[a], E.S. Marstein[a]

[a]*Department of Solar Energy, Institute for Energy Technology, Instituttveien 18, 2007 Kjeller, Norway*
[b]*Department of Physics, Norwegian University of Science and Technology, Høgskoleringen 5, 7491 Trondheim, Norway*

Abstract

Monolayer colloidal crystals are formed using silica- and polystyrene beads and used as etch masks for the formation of regular, μm period hexagonal arrays of indentations in a silicon wafer. Such patterns can be used as diffraction gratings or as seeds for further processing, for example by pit-catalysed electrochemical etching. In another experiment, multilayer colloidal crystals are infiltrated with titania before subsequent removal of the beads, forming inverse opals displaying tuneable reflectivities which are interesting for use as selective reflectors.

Keywords: light trapping, solar cells, nanosphere lithography, colloidal crystals, inverted opals, diffraction gratings

1. Introduction

The crystalline silicon solar cell industry is continuously moving towards thinner and thinner wafers as the production of solar cell grade silicon is a costly and energy intensive process. Thinner wafers are also beneficial because the collection efficiency of photogenerated free charges increases due to a shorter path way to the contacts. However, making a solar cell thinner allows more low-energy photons to pass through the entire structure without being absorbed, thus reducing efficiency. For this reason light harvesting (trapping) of low-energy photons is becoming an issue of increasing significance also for crystalline silicon solar cells. If the path length of photons inside the wafer can be increased by such light trapping structures, then the wafer can be made proportionally thinner without sacrificing efficiency. The most common light harvesting method in industry today is surface texturing by chemical etching, which scatters light into the solar cell due to refraction at the surface. This typically yields an average path length enhancement factor no greater than 10, which is only one fifth of the theoretical Lambertian limit for random scatterers in crystalline silicon [1].

*Corresponding author. Tel.: +47-95734413; fax: +47-63816356.
E-mail address: einar.haugan@ife.no

Periodic gratings with lattice periods close to photon wavelength may scatter light into non-zero diffraction orders, effectively increasing the path length of light inside the wafer. It has even been shown that the Lambertian limit can be exceeded by such geometries [2]. We have synthesised various periodic light harvesting structures for solar cell applications using colloidal crystal templates. 3D crystals are infiltrated with a dielectric material before the template is removed, leaving inverted opals displaying photonic band gaps giving sharp reflectivity peaks which make them interesting as selective reflectors. 2D crystals are used in nanosphere lithography for creating periodic patterns of pits, which may be used as diffraction gratings directly, or as initiation points or "seeds" for further processing into honeycomb-like structures by chemical or electrochemical etching.

2. Experimental

2.1. Substrate pre-treatment

Monocrystalline silicon wafers were used as substrates. Prior to template growth, the wafers were cleaned thoroughly using DI water and placed in a bath of DI water/NH_3(27%)/H_2O_2(30%), 515:85:100 volume ratio, at 70°C for 15 minutes. This was done to make the surface hydrophilic.

2.2. Colloidal crystal templates

In our experiments, 2D and 3D templates were grown from suspensions of microspheres purchased from Bangs Laboratories, Inc. Polystyrene (PS) beads gave the highest crystal quality and were therefore used when possible, while silica beads were used when high temperature processing was required. Bead diameters were selected for the optical properties of the final structures, determined by simulations [3, 4].

3D crystal synthesis. A 0.75 wt% solution of 490 nm diameter colloidal PS beads was prepared in a 25 ml glass beaker. The solution was thinned out to the desired concentration using DI water, before the glass beaker was placed in an ultrasonic bath for 15 minutes to break up any aggregates of colloidal spheres that may have formed.

Sphere self assembly was achieved using evaporation induced self assembly (EISA) [5]. Two cleaned substrates were inserted vertically into the beaker and placed in a heating cupboard for 24 hours at 63°C for the solvent to evaporate and the spheres to self-assemble on the substrate surface. According to Nagayama et al. [6] the growth rate v and hence the thickness of a multilayer colloidal crystal formed in this way depends on the volume fraction of solids in the solution, φ , as $v \propto \frac{\varphi}{1-\varphi}$. As the concentration of beads in the solution increases during deposition, it is therefore difficult to obtain homogeneous films by this method. Our samples typically showed a thickness variation from 10 layers (top) to 40 layers (bottom) of the substrate. For the optical properties, the thickness is not critical as long as it exceeds 5-8 layers [7]. Finally, the samples were sintered at the glass transition temperature of polystyrene (95°C) for 20 minutes.

2D crystal synthesis. Suspensions of 800 nm diameter silica beads were ultracentrifuged to increase the volume fraction of solids in water to approximately 30%. Solutions were sonicated for 5 hours at 24-27°C to break up aggregates, as suggested by Kumar [8] prior to spin-coating using a Bidtec SP100 spin coater. This was done by applying approximately 100 μl of solution onto a 1.5x1.5 cm^2 substrate, rotating the substrate to achieve full wetting, and then spin coating at 300 RPM for 1 second before increasing to 5500 RPM for 30 seconds. The same method was used for 1 μm PS beads, except only 5 minutes ultrasonication was needed.

2.3. 3D photonic crystals. Infiltration and inversion

With the 3D colloidal crystals in place, the next step is to fill the voids in the opal with a dielectric to enhance the refractive index contrast and thus maximize the band gaps. Infiltration with titania (TiO_2) was done using a Beneq TFS-500 atomic layer deposition machine. The precursors used were $TiCl_4$ (Aldrich 98%) and DI water. The chamber was purged using nitrogen of purity > 99.9999% between precursor pulses. The pulse/purge routine was: 0.25/0.75/0.25/0.75 seconds $TiCl_4$/purge/H_2O/purge. The deposition temperature was set to 85°C.

After infiltration, the PS colloidal sphere template was removed by calcination, leaving an inverse opal. This was done by heating to 525°C for 2 hours in a furnace with a 2 hour ramp-up. Besides removing the polystyrene, heat treating at these temperatures is reported to initiate the phase transition from amorphous titania to anatase [3].

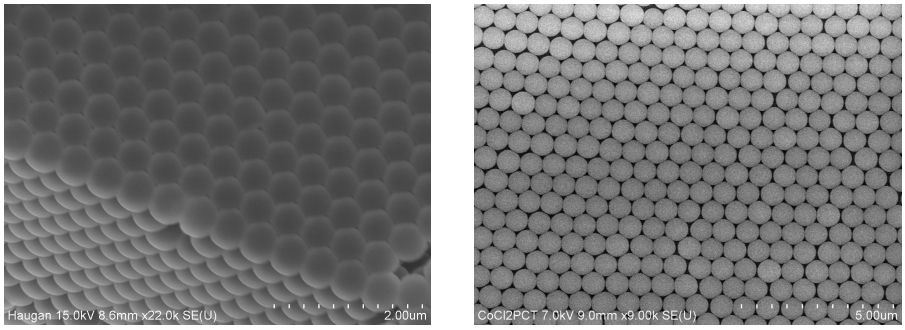

(a) Multilayer crystal (b) Single layer crystal

Figure 1: Scanning electron microscopy (SEM) images of the mono- and multilayer colloidal crystals synthesised

2.4. 2D photonic crystals by selective etching

In the first method, 50 nm of silicon nitride was deposited onto 2D colloidal crystals of silica beads to create an etch mask. The nitride was deposited using a Plasmalab System 133 PECVD at 400°C and 150 W RF power. After nitride deposition, the beads could be removed by sonication in ethanol for 2 minutes, leaving a silicon nitride etch mask. The substrates were then dipped in a 47% potassium hydroxide (KOH) solution for 30 seconds to etch pyramidic pits through the holes in the etch mask. At these conditions the etch rate along the {110} directions is approximately 700 nm/min [9, 10].

In the second method, monolayers of PS beads were covered by a 70 nm thick film of silver by thermal evaporation. The beads were removed by sonication, leaving behind triangular islands of silver. The samples were then submerged in a 4.6 M HF / 0.44 M H_2O_2 solution for 60 seconds. Silver is a catalyst for the etching of silicon by this solution.

3. Results

3.1. Colloidal crystal templates

3D crystal synthesis. The 3D crystals made were polycrystalline, with predominantly an hexagonal close packed ordering. This could be confirmed by laser diffraction experiments, looking at the reflection from the sample of a red laser beam of wavelength $\lambda = 650$ nm on a sand blasted plexiglass screen. The pattern of the reflected light showed clear hexagonal features, representing the Fourier transform of the structure. This would indicate that the real-space structure also has hexagonal symmetry [11]. Importantly, the laser spot size was so large that it would span across something in the order of 100 crystal domains, so the clear diffraction pattern indicates that adjacent domains maintained the same crystallographic orientation and packing conformation. Further corroboration of this comes from the fact that rotating the sample also caused the diffraction pattern to rotate accordingly. Thus, hexagonally close packed multilayer colloidal crystals could routinely be manufactured with thicknesses exceeding 10 layers.

2D crystal synthesis. The spin coating procedure produced a polycrystalline monolayer of spheres of predominantly hexagonal close-packed conformation, as seen in Figure 1 and confirmed by the presence of six-armed reflection patterns under white light. The monolayer quality was investigated in optical microscopy and scanning electron microscopy (SEM). Polycrystalline monolayers of PS beads covering typically 85% of the sample area were routinely manufactured, with the remaining area being mostly double layer. However for silica beads, agglomeration in solution prior to spin coating remained a problem even after several hours of ultrasonication at carefully controlled temperatures. Silica bead monolayers thus contained regions of poor quality in between crystal domains.

3.2. 3D photonic crystals. Infiltration and inversion

3D colloidal crystal templates were infiltrated with titania. Figure 2a shows the final structure after removal of the template. The refractive index of the relevant crystalline phases of titania have a refractive index in the range 2.3–3.0 in the wavelength range of interest. This contrast is too low to give rise to full photonic band gaps even after

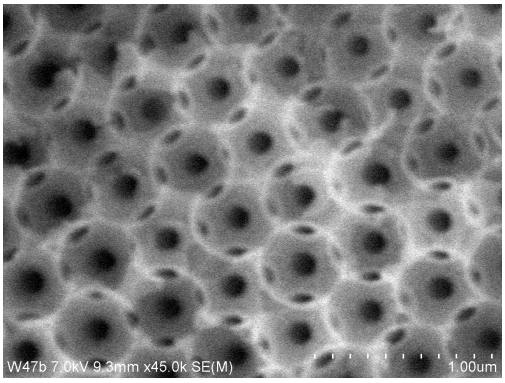

(a) SEM image of inverse titania opal

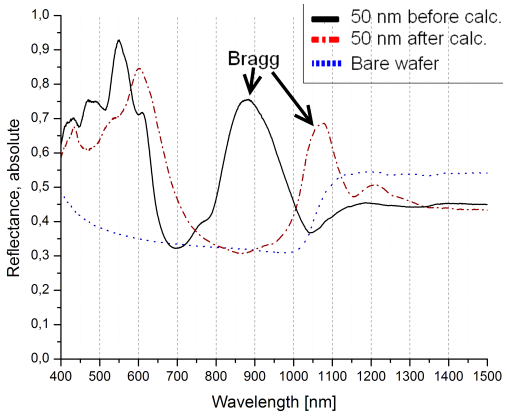

(b) Optical response of titania infiltrated opal before and after template removal by calcination. Interstices saturated with titania

Figure 2: Inverse titania opal. Template sphere diameter 490 nm

inversion of the opals. However, band structure simulations by King [12] predict several incomplete band gaps to arise following infiltration and inversion, detectable as peaks in the reflectivity spectrum.

Figure 2b shows the reflectivity of a titania infiltrated template. In addition to the Bragg peak, reflectivity peaks are also observed at high energies. After template removal (inversion) by calcination the refractive index contrast is increased, causing a blue shift of the reflectivity peaks. Also, some of the high-energy peaks get more pronounced. Templates with smaller diameter spheres gave similar reflectivity spectra, but with peaks at shorter wavelengths, demonstrating the size dependence of the band structure of these geometries.

We have achieved very good control and understanding of these structures, and we are able to tailor the reflectivity spectrum. However we also conclude that the band gaps, and thus the reflectivity peaks, are too narrow to be used as broad back reflectors in solar cells. We foresee that these structures are most relevant as spectral filters or selective reflectors in advanced solar cell applications.

3.3. 2D photonic crystals by selective etching

Method # 1. Silicon nitride etch masks, KOH etching. After nanosphere liftoff by sonication a thin layer of silicon nitride remained on the wafer, even in the "shadow regions" beneath the spheres. Atomic force microscopy (AFM) scans of these structures confirm the gradual thickness decrease of the nitride in the shadow region, forming a concave shape. Typical thickness variations from top to bottom of these concave shapes was 5 nm. At the bottom of each concave pit the bare silicon wafer was exposed in a 100 nm diameter patch, where the bead was touching the substrate.

Samples were then submerged in KOH, which etches crystalline silicon preferentially along the {110} directions. The etch does not attack silicon nitride, giving an essentially infinite etch selectivity [13]. Figure 3a shows a SEM image of a structure after KOH exposure and subsequent nitride stripping. This image reveals how the etching has indeed been confined to only the small exposed areas. Due to the high selectivity of the KOH etch on different crystallographic planes, etching is self-limiting.

Method # 2. Silver catalysed etching of silicon. AFM scans of the silver islands revealed that silver deposition was highly directional, as expected, with very little coverage in the shadow regions underneath the spheres. This is in sharp contrast to the nitride deposition in the previous section.

With the metal islands in place, samples were submerged in the HF / H_2O_2 etchant solution. As can be seen from Figures 3b and 3c, this method proved successful. From the top-down image, Figure 3b, we see that dark spots are formed where the silver islands used to be. The dark spots represent depressions in the wafer. The cross-sectional SEM image in Figure 3c demonstrates that the sidewall profile is indeed very straight, with no appreciable widening or narrowing of the groove. This is in line with the results by Huang et al [14]. Energy-dispersive X-ray spectroscopy (EDS) scans of the pits (Figure 3c, inset) show a high silver content at the bottom of the pits, as expected.

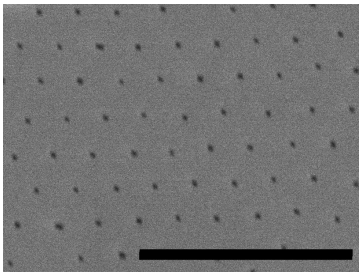

(a) Method # 1, after KOH etching and nitride stripping. Dark spots are pyramids etched out by the KOH. Scale bar 4 μm

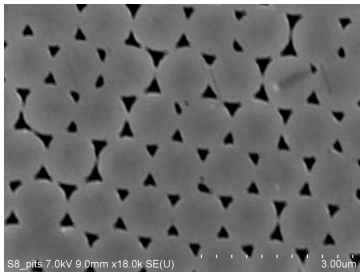

(b) Method # 2, metal catalysed pits (dark) seen from above

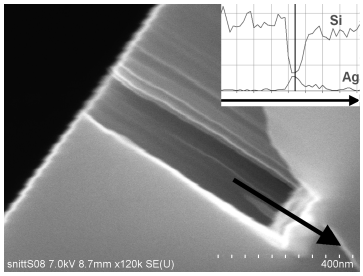

(c) Method # 2, metal catalysed pit seen from the side. The inset shows an EDS line scan (elemental analysis) along the arrow. At the bottom of the pit the silver concentration is high. 60 second etch

Figure 3: SEM images of etch pits, formed by the two methods

4. Conclusion

In conclusion, we have successfully manufactured single- and multilayer colloidal crystals on silicon wafers and used them as templates for the production of various geometries intended for light harvesting in solar cells. Specifically, we have made titania inverse opals displaying multiple reflectivity peaks whose wavelength position can be tuned by altering the degree of infiltration and template bead size. These structures are intended for use as selective reflectors in advanced multilayer solar cells. Also, we have demonstrated two different techniques for the formation of hexagonal arrays of dents or dimples in a wafer. These methods can either be used to form 2D light harvesting structures directly, or to form initiation points (“seeds”) for further processing into honeycomb structures by chemical- or electrochemical etching. Specifically, silicon nitride etch masks were made by nanosphere lithography, displaying 100 nm diameter holes with a sub-micron pitch. These masks were then used as etch masks for KOH etching, forming pyramidal dents in the exposed wafer. Silver catalysed etching was also used to form hexagonal arrays of pits.

References

[1] J. Nelson, The Physics of Solar Cells, Imperial College Press, London, 2003.
[2] Z. Yu, A. Raman, S. Fan, Fundamental limit of light trapping in grating structures, Optics Express 18 (103) (2010) A366–A380.
[3] J. King, D. Heineman, E. Graugnard, C. Summers, Atomic layer deposition in porous structures: 3D photonic crystals, Applied Surface Science 244 (1-4) (2005) 511–516.
[4] J. Gjessing, A. Sudbø, E. Marstein, Comparison of periodic light-trapping structures in thin solar cells, Journal xx (2011) xx, submitted for publication.
[5] P. Jiang, J. Bertone, K. Hwang, V. Colvin, Single-crystal colloidal multilayers of controlled thickness, Chem. Mater 11 (8) (1999) 2132–2140.
[6] A. Dimitrov, K. Nagayama, Continuous convective assembling of fine particles into two-dimensional arrays on solid surfaces, Langmuir 12 (5) (1996) 1303–1311.
[7] H. Granlund, Fabrication of a photonic crystal using self-assembly. a potentially new rear reflector in solar cells, Master’s thesis, NTNU, Trondheim, Norway (2009).
[8] K. Kumar, Preparation and characterization of spin-coated colloidal templates and patterned electrodeposited cobalt, Ph.D. thesis, Memorial University of Newfoundland (2008).
[9] H. Seidel, L. Csepregi, A. Heuberger, H. Baumgartel, Anisotropic etching of crystalline silicon in alkaline solutions, J. Electrochem. Soc 137 (11) (1990) 3612–3626.
[10] K. Mangersnes, Back-contacted back-junction silicon solar cells, Ph.D. thesis, University of Oslo (2010).
[11] A. Sinitskii, V. Abramova, T. Laptinskaya, Y. Tretyakov, Domain mapping of inverse photonic crystals by laser diffraction, Physics Letters A 366 (4-5) (2007) 516–522.
[12] J. King, Fabrication of opal-based photonic crystals using atomic layer deposition, Ph.D. thesis, Georgia Institute of Technology (2004).
[13] K. Williams, K. Gupta, M. Wasilik, Etch rates for micromachining processing-Part II, Microelectromechanical Systems, Journal of 12 (6) (2003) 761–778.
[14] Z. Huang, H. Fang, J. Zhu, Fabrication of silicon nanowire arrays with controlled diameter, length, and density, Advanced Materials 19 (5) (2007) 744–748.

Bibliography

[1] T. Markvart. *Solar electricity*. Wiley and Sons, Chichester, 2 edition, 2000.

[2] J. Nelson. *The Physics of Solar Cells*. Imperial College Press, London, 2003.

[3] Sciencedaily.com. Highest silicon solar cell efficiency ever reached. `http://www.sciencedaily.com/releases/2008/10/081023100536.htm`, Oct 2008.

[4] Photon international. April 2006.

[5] VM Fthenakis and HC Kim. Photovoltaics: Life-cycle analyses. *Solar Energy*, 2010.

[6] I.M. Peters. *Photonic concepts for solar cells*. PhD thesis, Faculty of Mathematics and Physics, Albert-Ludwigs-University, Freiburg Im Breisgau, 2009.

[7] Astm standard g159-98, "standard tables for references solar spectral irradiance at air mass 1.5". ASTM International, West Conshohocken, PA.

[8] E. Yablonovitch. Statistical ray optics. *J. Opt. Soc. Am*, 72(7):899–907, 1982.

[9] R.H. Lipson and C. Lu. Photonic crystals: a unique partnership between light and matter. *European Journal of Physics*, 30:S33, 2009.

[10] J. Joannopolulos, S. Johnson, J.N. Winn, and R. D. Meade. *Photonic Crystals: Molding the Flow of Light*. Princeton University Press, New Jersey, 2. edition, 2008.

[11] C. Kittel. *Introduction to Solid State Physics*. John Wiley and Sons, New Jersey, 8 edition, 2005.

[12] A.J. Danner. An introduction to the plane wave expansion method for calculating photonic crystal band diagrams. `http://www.ece.nus.edu.sg/stfpage/eleadj/planewave.htm`, 2005. Retrieved 05.10.2010.

[13] J.S. King, D. Heineman, E. Graugnard, and CJ Summers. Atomic layer deposition in porous structures: 3D photonic crystals. *Applied Surface Science*, 244(1-4):511–516, 2005.

[14] D. Zhou. *Light-trapping enhancement in thin film solar cells with photonic crystals*. PhD thesis, Iowa State University, 2008.

[15] Z. Yu, A. Raman, and S. Fan. Fundamental limit of light trapping in grating structures. *Optics Express*, 18(103):A366–A380, 2010.

[16] Z.Y. Li, B.Y. Gu, and G.Z. Yang. Large absolute band gap in 2D anisotropic photonic crystals. *Physical Review Letters*, 81(12):2574–2577, 1998.

[17] H. Granlund. Fabrication of a photonic crystal using self-assembly. a potentially new rear reflector in solar cells. Master's thesis, NTNU, Trondheim, Norway, 2009.

[18] H. Sai, Y. Kanamori, K. Arafune, Y. Ohshita, and M. Yamaguchi. Light trapping effect of submicron surface textures in crystalline Si solar cells. *Progress in Photovoltaics: Research and Applications*, 15(5):415–423, 2007.

[19] J. Gjessing, E.S. Marstein, and A. Sudbø. 2D back-side diffraction grating for improved light trapping in thin silicon solar cells. *Optics Express*, 18(6):5481–5495, 2010.

[20] J.M. Gee. Optically enhanced absorption in thin silicon layers using photonic crystals. In *Photovoltaic Specialists Conference, 2002. Conference Record of the Twenty-Ninth IEEE*, pages 150–153. IEEE, 2003.

[21] J. Gjessing, A. Sudbø, and E. Marstein. Comparison of periodic light-trapping structures in thin solar cells. *Journal*, xx:xx, 2011. Submitted for publication.

[22] D. Zhou and R. Biswas. Photonic crystal enhanced light-trapping in thin film solar cells. *Journal of Applied Physics*, 103:093102, 2008.

[23] K.L. Kelly, E. Coronado, L.L. Zhao, and G.C. Schatz. The optical properties of metal nanoparticles: the influence of size, shape, and dielectric environment. *The Journal of Physical Chemistry B*, 107(3):668–677, 2003.

[24] D.B. Sánchez et al. The surface plasmon resonance of supported noble metal nanoparticles: Characterization, laser tailoring, and sers application. 2007.

[25] KR Catchpole and A. Polman. Plasmonic solar cells. *Optics express*, 16(26):21793–21800, 2008.

[26] L. Novotny and B. Hecht. *Principles of nano-optics*. Cambridge University Press, 2006.

[27] A.J. Haes, C.L. Haynes, A.D. McFarland, G.C. Schatz, R.P. Van Duyne, and S. Zou. Plasmonic Materials. *MRS bulletin*, 30:369, 2005.

[28] T.R. Jensen, G.C. Schatz, and R.P. Van Duyne. Nanosphere Lithography: Surface Plasmon Resonance Spectrum of a Periodic Array of Silver Nanoparticles by Ultraviolet- Visible Extinction Spectroscopy and Electrodynamic Modeling. *J. Phys. Chem. B*, 103(13):2394–2401, 1999.

[29] C.L. Haynes and R.P. Van Duyne. Nanosphere lithography: a versatile nanofabrication tool for studies of size-dependent nanoparticle optics. *J. Phys. Chem. B*, 105(24):5599–5611, 2001.

[30] H.A. Atwater and A. Polman. Plasmonics for improved photovoltaic devices. *Nature Materials*, 9(3):205–213, 2010.

[31] J. Mertz. Radiative absorption, fluorescence, and scattering of a classical dipole near a lossless interface: a unified description. *JOSA B*, 17(11):1906–1913, 2000.

[32] P.G. O'Brien, N.P. Kherani, S. Zukotynski, G.A. Ozin, E. Vekris, N. Tetreault, A. Chutinan, S. John, A. Mihi, and H. Míguez. Enhanced Photoconductivity in Thin-Film Semiconductors Optically Coupled to Photonic Crystals. *Advanced Materials*, 19(23):4177–4182, 2007.

[33] A. Mihi, H. Miguez, I. Rodriguez, S. Rubio, and F. Meseguer. Surface resonant modes in colloidal photonic crystals. *Physical Review B*, 71(12):125131, 2005.

[34] W. Stöber, A. Fink, and E. Bohn. Controlled growth of monodisperse silica spheres in the micron size range. *Journal of Colloid and Interface Science*, 26(1):62–69, 1968.

[35] G. Ozin and A. Arsenault. *Nanochemistry. A chemical approach to nanomaterials.* The Royal Society of Chemistry, Cambridge, 2005.

[36] Y. Xia, B. Gates, Y. Yin, and Y. Lu. Monodispersed colloidal spheres: old materials with new applications. *Advanced Materials*, 12(10):693–713, 2000.

[37] Y.G. Ko and D.H. Shin. Effects of liquid bridge between colloidal spheres and evaporation temperature on fabrication of colloidal multilayers. *J. Phys. Chem. B*, 111(7):1545–1551, 2007.

[38] N. Denkov, O. Velev, P. Kralchevski, I. Ivanov, H. Yoshimura, and K. Nagayama. Mechanism of formation of two-dimensional crystals from latex particles on substrates. *Langmuir*, 8(12):3183–3190, 1992.

[39] A.S. Dimitrov and K. Nagayama. Continuous convective assembling of fine particles into two-dimensional arrays on solid surfaces. *Langmuir*, 12(5):1303–1311, 1996.

[40] H. Ko, H.W. Lee, and J. Moon. Fabrication of colloidal self-assembled monolayer (SAM) using monodisperse silica and its use as a lithographic mask. *Thin Solid Films*, 447:638–644, 2004.

[41] Y. Li, T. Sasaki, Y. Shimizu, and N. Koshizaki. Hexagonal-Close-Packed, Hierarchical Amorphous TiO2 Nanocolumn Arrays: Transferability, Enhanced Photocatalytic Activity, and Superamphiphilicity without UV Irradiation. *Journal of the American Chemical Society*, 130(44):14755–14762, 2008.

[42] P. Jiang and M.J. McFarland. Large-scale fabrication of wafer-size colloidal crystals, macroporous polymers and nanocomposites by spin-coating. *J. Am. Chem. Soc*, 126(42):13778–13786, 2004.

[43] P. Jiang, T. Prasad, M.J. McFarland, and V.L. Colvin. Two-dimensional nonclose-packed colloidal crystals formed by spincoating. *Applied Physics Letters*, 89:011908, 2006.

[44] C. Liu, J. Liu, D. Gao, M. Ding, and J.M. Lin. Fabrication of Microwell Arrays Based on Two-Dimensional Ordered Polystyrene Microspheres for High-Throughput Single-Cell Analysis. *Analytical Chemistry*, pages 544–546.

[45] R. Micheletto, H. Fukuda, and M. Ohtsu. A simple method for the production of a two-dimensional, ordered array of small latex particles. *Langmuir*, 11(9):3333–3336, 1995.

[46] A. Kosiorek, W. Kandulski, P. Chudzinski, K. Kempa, and M. Giersig. Shadow nanosphere lithography: Simulation and experiment. *Nano letters*, 4(7):1359–1363, 2004.

[47] S. Rakers, LF Chi, and H. Fuchs. Influence of the evaporation rate on the packing order of polydisperse latex monofilms. *Langmuir*, 13(26):7121–7124, 1997.

[48] GQ Liu, ZS Wang, and YH Ji. Influence of growth parameters on the fabrication of high-quality colloidal crystals via a controlled evaporation self-assembly method. *Thin Solid Films*, 518(18):5083–5090, 2010.

[49] F. Burmeister, W. Badowsky, T. Braun, S. Wieprich, J. Boneberg, and P. Leiderer. Colloid monolayer lithography-A flexible approach for nanostructuring of surfaces. *Applied Surface Science*, 144:461–466, 1999.

[50] K. Kumar. *Preparation and characterization of spin-coated colloidal templates and patterned electrodeposited cobalt.* PhD thesis, Memorial University of Newfoundland, 2008.

[51] A. Mihi, M. Ocaña, and H. Míguez. Oriented Colloidal-Crystal Thin Films by Spin-Coating Microspheres Dispersed in Volatile Media. *Advanced Materials*, 18(17):2244–2249, 2006.

[52] J.C. Hulteen and R.P. Van Duyne. Nanosphere lithography: A materials general fabrication process for periodic particle array surfaces. *Journal of Vacuum Science & Technology A: Vacuum, Surfaces, and Films*, 13(3):1553–1558, 1994.

[53] M.J.K. Klein, M. Guillaumée, B. Wenger, L.A. Dunbar, J. Brugger, H. Heinzelmann, and R. Pugin. Inexpensive and fast wafer-scale fabrication of nanohole arrays in thin gold films for plasmonics. *Nanotechnology*, 21:205301, 2010.

[54] D.J. Norris, E.G. Arlinghaus, L. Meng, R. Heiny, and L.E. Scriven. Opaline Photonic Crystals: How Does Self-Assembly Work? *Advanced Materials*, 16(16):1393–1399, 2004.

[55] P. Jiang, J.F. Bertone, K.S. Hwang, and V.L. Colvin. Single-crystal colloidal multilayers of controlled thickness. *Chem. Mater*, 11(8):2132–2140, 1999.

[56] L.V. Woodcock. Entropy difference between the face-centred cubic and hexagonal close-packed crystal structures. *Nature*, 385(6612):141–143, 1997.

[57] E. Palacios-Lidón, A. Blanco, M. Ibisate, F. Meseguer, C. López, and J. Sánchez-Dehesa. Optical study of the full photonic band gap in silicon inverse opals. *Applied Physics Letters*, 81:4925, 2002.

[58] A. Imhof. Three-dimensional photonic crystals made from colloids. *Nanoscale Materials*, pages 423–454, 2004.

[59] C. Arcos, K. Kumar, W. González-Viñas, R. Sirera, K.M. Poduska, and A. Yethiraj. Orientationally correlated colloidal polycrystals without long-range positional order. *Physical Review E*, 77(5):050402, 2008.

[60] M.D. Malinsky, K.L. Kelly, G.C. Schatz, and R.P. Van Duyne. Nanosphere lithography: Effect of substrate on the localized surface plasmon resonance spectrum of silver nanoparticles. *J. Phys. Chem. B*, 105(12):2343–2350, 2001.

[61] A. Valsesia, T. Meziani, F. Bretagnol, P. Colpo, G. Ceccone, and F. Rossi. Plasma assisted production of chemical nano-patterns by nano-sphere lithography: application to bio-interfaces. *Journal of Physics D: Applied Physics*, 40:2341, 2007.

[62] L. Li, T. Zhai, H. Zeng, X. Fang, Y. Bando, and D. Golberg. Polystyrene sphere-assisted one-dimensional nanostructure arrays: synthesis and applications. *J. Mater. Chem.*, 2010.

[63] C.L. Cheung, RJ Nikolić, CE Reinhardt, and TF Wang. Fabrication of nanopillars by nanosphere lithography. *Nanotechnology*, 17:1339, 2006.

[64] H. Seidel, L. Csepregi, A. Heuberger, and H. Baumgartel. Anisotropic etching of crystalline silicon in alkaline solutions. *J. Electrochem. Soc*, 137(11):3612–3626, 1990.

[65] M. Yun, A. Turner, R.J. Roedel, and M.N. Kozicki. Novel lateral field emission device fabricated on silicon-on-insulator material. *Journal of Vacuum Science & Technology B: Microelectronics and Nanometer Structures*, 17:1561, 1999.

[66] K.R. Williams, K. Gupta, and M. Wasilik. Etch rates for micromachining processing-Part II. *Microelectromechanical Systems, Journal of*, 12(6):761–778, 2003.

[67] J.M. Köhler. *Etching in microsystem technology*. Wiley-VCH, 1999.

[68] J. Schilling, F. Müller, S. Matthias, RB Wehrspohn, U. Gösele, and K. Busch. Three-dimensional photonic crystals based on macroporous silicon with modulated pore diameter. *Applied Physics Letters*, 78:1180, 2001.

[69] G. Pellegrini, P. Roy, R. Bates, D. Jones, K. Mathieson, J. Melone, V. O'Shea, KM Smith, I. Thayne, P. Thornton, et al. Technology development of 3D detectors for high-energy physics and imaging. *Nuclear Instruments and Methods in Physics Research Section A: Accelerators, Spectrometers, Detectors and Associated Equipment*, 487(1-2):19–26, 2002.

[70] S. Matthias, J. Schilling, K. Nielsch, F. Müller, R.B. Wehrspohn, and U. Gösele. Monodisperse diameter-modulated gold microwires. *Advanced Materials*, 14(22):1618–1621, 2002.

[71] F. Müller, A. Birner, U. Gösele, V. Lehmann, S. Ottow, and H. Föll. Structuring of macroporous silicon for applications as photonic crystals. *Journal of Porous Materials*, 7(1):201–204, 2000.

[72] H. Föll, M. Christophersen, J. Carstensen, and G. Hasse. Formation and application of porous silicon. *Materials Science and Engineering: R: Reports*, 39(4):93–141, 2002.

[73] F. Müller, A. Birner, J. Schilling, U. Gösele, C. Kettner, and P. Hänggi. Membranes for micropumps from macroporous silicon. *physica status solidi (a)*, 182(1):585–590, 2000.

[74] X. Li and PW Bohn. Metal-assisted chemical etching in HF/HO produces porous silicon. *Applied Physics Letters*, 77:2572, 2000.

[75] Z. Huang, N. Geyer, P. Werner, J. de Boor, and U. Gösele. Metal-assisted chemical etching of silicon: A review. *Advanced Materials*, 23:285–308, 2011.

[76] Z. Huang, H. Fang, and J. Zhu. Fabrication of silicon nanowire arrays with controlled diameter, length, and density. *Advanced Materials*, 19(5):744–748, 2007.

[77] A. Plech, P. Leiderer, and J. Boneberg. Femtosecond laser near field ablation. *Laser & Photonics Reviews*, 3(5):435–451, 2009.

[78] D. Brodoceanu, L. Landström, and D. Bäuerle. Laser-induced nanopatterning of silicon with colloidal monolayers. *Applied Physics A: Materials Science & Processing*, 86(3):313–314, 2007.

[79] SM Huang, Z. Sun, BS Lukyanchuk, MH Hong, and LP Shi. Nanobump arrays fabricated by laser irradiation of polystyrene particle layers on silicon. *Applied Physics Letters*, 86:161911, 2005.

[80] Arrhenius equation, 1997. IUPAC Compendium of Chemical Terminology.

[81] D.L. Smith. *Thin-film deposition: principles and practice*. McGraw-Hill Professional, New York, 1995.

[82] C.A. Bishop. *Vacuum deposition onto webs, films, and foils*. Number v. 0, no. 8155 in Materials science and process technology series. William Andrew Pub., 2007.

[83] J. Perrière, E. Millon, and E. Fogarassy. *Recent advances in laser processing of materials*. European Materials Research Society Series. Elsevier, 2006.

[84] S.M. Rossnagel, J.J. Cuomo, and W.D. Westwood. *Handbook of plasma processing technology: fundamentals, etching, deposition, and surface interactions*. Materials science and process technology series. Noyes Publications, 1990.

[85] Labsphere Inc. A guide to integrating sphere theory and applications. `http://www.labsphere.com/data/userFiles/A%20Guide%20to%20Integrating%20Sphere%20Theory&Apps.pdf`. Retrieved 12.12.2010.

[86] E. Haugan. Reflektans av silisiumwafere med bakreflektor av aluminium. *Institutt for Energiteknikk*, 2010.

[87] D.G. Brandon and W.D. Kaplan. *Microstructural characterization of materials*. Quantitative software engineering series. John Wiley, 2008.

[88] P.J. Eaton, P. Eaton, and P. West. *Atomic force microscopy*. Oxford University Press, 2010.

[89] P. Dixit, X. Chen, J. Miao, S. Divakaran, and R. Preisser. Study of surface treatment processes for improvement in the wettability of silicon-based materials used in high aspect ratio through-via copper electroplating. *Applied Surface Science*, 253(21):8637–8646, 2007.

[90] Bangs Laboratories Inc. Technote 203. washing microspheres. `http://www.bangslabs.com/files/bangs/docs/pdf/203.pdf`, 2008.

[91] K. Mangersnes. *Back-contacted back-junction silicon solar cells*. PhD thesis, University of Oslo, 2010.

[92] S. Helland. Surface passivation using silicon nitride (a-sinx:h) for silicon based solar cells, 2010. Norwegian University of Science and Technology.

[93] J.C. Goldschmidt, P. Loper, S. Fischer, S. Janz, M. Peters, S.W. Glunz, G. Willeke, E. Lifshitz, K. Kramer, and D. Biner. Advanced upconverter systems with spectral and geometric concentration for high upconversion efficiencies. In *Optoelectronic and Microelectronic Materials and Devices, 2008. COMMAD 2008. Conference on*, pages 307–311. IEEE, 2009.

[94] F. Wang and X. Liu. Recent advances in the chemistry of lanthanide-doped upconversion nanocrystals. *Chemical Society Reviews*, 38(4):976–989, 2009.

[95] T. Trupke, A. Shalav, BS Richards, P. Würfel, and MA Green. Efficiency enhancement of solar cells by luminescent up-conversion of sunlight. *Solar Energy Materials and Solar Cells*, 90(18-19):3327–3338, 2006.

[96] F. Auzel. Upconversion and anti-Stokes processes with f and d ions in solids. *Chem. Rev*, 104(1):139–174, 2004.

[97] A. Shalav, BS Richards, and MA Green. Luminescent layers for enhanced silicon solar cell performance: Up-conversion. *Solar Energy Materials and Solar Cells*, 91(9):829–842, 2007.

[98] RenewableEnergyWorld.com Montgomery, J. Researchers: "up-conversion" creates "super-efficient" solar cells. `http://www.renewableenergyworld.com/rea/news/article/2009/11/researchers-upconversion-creates-super-efficient-solar-cells`, 11 2009. Retrieved 24.01.2011.

[99] K.W. Kraemer, D. Biner, G. Frei, H.U. Guedel, M.P. Hehlen, and S.R. Luethi. Hexagonal sodium yttrium fluoride based green and blue emitting upconversion phosphors. *Chem. Mater*, 16(7):1244–1251, 2004.

[100] C. Strümpel, M. McCann, G. Beaucarne, V. Arkhipov, A. Slaoui, V. Svrcek, C. del Caņizo, and I. Tobias. Modifying the solar spectrum to enhance silicon solar cell efficiency–An overview of available materials. *Solar Energy Materials and Solar Cells*, 91(4):238–249, 2007.

[101] E. Haugan. Inverted opal photonic crystals as back reflectors in silicon wafer solar cells, 2010. Norwegian University of Science and Technology.

[102] P. Lodahl, A.F. Van Driel, I.S. Nikolaev, A. Irman, K. Overgaag, D. Vanmaekelbergh, and W.L. Vos. Controlling the dynamics of spontaneous emission from quantum dots by photonic crystals. *Nature*, 430(7000):654–657, 2004.

[103] Z. Yang, K. Zhu, Z. Song, D. Zhou, Z. Yin, and J. Qiu. Effect of photonic bandgap on upconversion emission in ybpo4:er inverse opal photonic crystals. *Applied Optics*, 50(3):287–290, 2011.